MULTI-DIMENSIONAL ERROR ANALYSIS OF NEARSHORE WAVE MODELING TOOLS, WITH APPLICATION TOWARD DATA-DRIVEN BOUNDARY CORRECTION

A Thesis

by

BOYANG JIANG

Submitted to the Office of Graduate Studies of
Texas A&M University
in partial fulfillment of the requirements for the degree of

MASTER OF SCIENCE

December 2010

Major Subject: Ocean Engineering

Multi-Dimensional Error Analysis of Nearshore Wave Modeling Tools,

with Application Toward Data-Driven Boundary Correction

MULTI-DIMENSIONAL ERROR ANALYSIS OF NEARSHORE WAVE MODELING TOOLS, WITH APPLICATION TOWARD DATA-DRIVEN BOUNDARY CORRECTION

A Thesis

by

BOYANG JIANG

Submitted to the Office of Graduate Studies of
Texas A&M University
in partial fulfillment of the requirements for the degree of

MASTER OF SCIENCE

Approved by:

Chair of Committee,	James M. Kaihatu
Committee Members,	Jun Zhang
	Robert D. Hetland
Head of Department,	John M. Niedzwecki

December 2010

Major Subject: Ocean Engineering

ABSTRACT

Multi-Dimensional Error Analysis of Nearshore Wave Modeling Tools, with Application Toward Data-Driven Boundary Correction. (August 2010)

Boyang Jiang, B.T., Hohai University,

Nanjing, China

Chair of Advisory Committee: Dr. James M. Kaihatu

As the forecasting models become more sophisticated in their physics and possible depictions of the nearshore hydrodynamics, they also become increasingly sensitive to errors in the inputs. These input errors include: mis-specification of the input parameters (bottom friction, eddy viscosity, etc.); errors in input fields and errors in the specification of boundary information (lateral boundary conditions, etc.). Errors in input parameters can be addressed with fairly straightforward parameter estimation techniques, while errors in input fields can be somewhat ameliorated by physical linkage between the scales of the bathymetric information and the associated model response. Evaluation of the errors on the boundary is less straightforward, and is the subject of this thesis.

The model under investigation herein is the Delft3D modeling suite, developed at Deltares (formerly Delft Hydraulics) in Delft, the Netherlands. Coupling of the wave (SWAN) and hydrodynamic (FLOW) model requires care at the lateral boundaries in order to balance run time and

error growth. To this extent, we use perturbation method and spatio-temporal analysis method such as Empirical Orthogonal Function (EOF) analysis to determine the various scales of motion in the flow field and the extent of their response to imposed boundary errors. From the Swirl Strength examinations, we find that the higher EOF modes are affected more by the lateral boundary errors than the lower ones.

DEDICATION

This thesis is dedicated to my parents, Maoguo and Maoling, who have taught me the importance of knowledge to achieve success, and how to establish objectives in my life that are both ambitious and attainable.

I also dedicate this research to my brother, who is going to graduate from high school next year. I hope one of his next steps will be reading – and bettering – his brother's previous work.

ACKNOWLEDGEMENTS

First and foremost, I cannot thank my committee chair Dr. James Kaihatu enough for providing me constant support throughout my research and being always welcoming and encouraging of new ideas for discussion. His patience and guidance were greatly instrumental to the achievement of this project. Many thanks are also due to my committee members, Dr. Jun Zhang and Dr. Robert D. Hetland, for consenting to be on my committee, and providing guidance throughout the course of this research. I must also thank Dr. Steven Dimarco and Dr. Ping Chang for their guidance on the subject of Empirical Orthogonal Function analysis.

This work would not have been possible without funding from Award number N00014-09-1-0503, granted by the Coastal Geosciences Program (Code 322 CG), Office of Naval Research, which provided financial support for my studies at Texas A&M University. I would also like to thank Drs. Steve Elgar (WHOI), Robert Guza (SIO), William O'Reilly (SIO), and the staff of the U.S. Army Corps Field Research Facility for the data used for this study.

Last, but not least, I thank my friends and colleagues and the Ocean Engineering faculty and staff for making my time at Texas A&M University a great experience.

TABLE OF CONTENTS

Page

LIST OF FIGURES

FIGURE Page

FIGURE Page

FIGURE Page

LIST OF TABLES

1. INTRODUCTION

Accurate descriptions of the nearshore wave, hydrodynamic and sediment transport and morphologic processes are necessary for many civilian and military activities in the nearshore. In particular, forecasting environmental conditions at a given area is of great importance for naval exercises and operations. This capability has progressed beyond simple reduced-dimension models (e.g., Navy Standard Surf Model; Earle 1989) to more sophisticated comprehensive three-dimensional hydrodynamic models (e.g., SHORECIRC; van Dongeren and Svendsen 2000; Delft3D; Lesser *et al*. 2004), with the realization that strong spatial and temporal non-homogeneities will greatly affect the nearshore hydrodynamic environment.

However, sites for operations in coastal and nearshore areas are usually poorly sampled, and input data are often obsolete (bathymetry) or of low resolution (input wave and current conditions, bathymetry). The effect of these characteristics of input data on increasingly sophisticated forecast models is unclear, but is necessary to know so that reasonable confidence limits can be placed on the results. This is especially true of boundary conditions. Additionally, the forecasts must be performed expediently; however many modeling practices developed to mitigate the potential effects of unknown boundary errors are not well suited to speedy forecasts. We propose to develop methods to evaluate the effect of boundary errors and help optimize the typical run configuration to reduce wasteful calculation required to handle open lateral boundaries.

This thesis follows the style of Coastal Engineering.

In this study we investigate the effect of lateral grid extensions on the model predictions, and will use two test areas (Duck, NC, and La Jolla, CA, both in the USA) for this evaluation.

1.1 Model and Input Descriptions

1.1.1 Delft3D FLOW

FLOW is a hydrodynamic model capable of simulating 2-D depth averaged or 3-D unsteady flow (e.g., coastal-scale tidal flows and wave-induced nearshore flows) by solving the unsteady non-linear shallow water equations for an incompressible fluid. It makes use of the hydrostatic pressure assumption, as the time and horizontal length scales of the modeled flow phenomena are significantly larger than the vertical scales. The governing system of equations also consists of the equation of continuity to compute vertical velocity in 3-D models, and the transport equations for the conserved constituents. The equations are formulated in orthogonal curvilinear coordinates. The flow is forced by water-level or tides at the open boundaries, wind stress at free surface, density gradients or water-level induced pressure gradients.

Roelvink and Walstra (2004) developed a Neumann lateral boundary condition for the FLOW model in order to allow flow to leave the lateral boundaries with no artificial circulation This condition assumes that the longshore gradient of the mean sea surface is zero at the lateral boundaries of the grid; the remaining dynamic variables would reach their “natural” values at the boundaries, and the resulting flow would be free of boundary-induced effects.

1.1.2 Delft3D WAVE (or SWAN in Its Standalone Configuration)

SWAN or Simulating Waves Near-shore (Booij *et al*., 1999), the wave module of the Delft-3D hydrodynamic package used herein, is a spectral wave model which simulates the generation of surface waves due to wind and the propagation of wave energy over arbitrarily-varying bathymetry. Wind-wave generation, whitecapping, wave-current interaction, deep and (parameterized) shallow water nonlinearity, bottom friction and wave breaking dissipation are all represented in the model.

Since the SWAN model accounts for wave-current interactions, it is based on the action balance equation (Hasselmann *et al.* 1973) rather than the energy balance equation. For small-scale computations, the equation in Cartesian coordinates is:

$$\begin{aligned}&\frac{\partial}{\partial t}N(\sigma,\theta;x,y,t)+\frac{\partial}{\partial x}c_x N(\sigma,\theta;x,y,t)+\frac{\partial}{\partial y}c_y N(\sigma,\theta;x,y,t)\\&+\frac{\partial}{\partial \sigma}c_\sigma N(\sigma,\theta;x,y,t)+\frac{\partial}{\partial \theta}c_\theta N(\sigma,\theta;x,y,t)=\frac{S(\sigma,\theta;x,y,t)}{\sigma}\end{aligned} \tag{1}$$

where $N(\sigma,\theta)$is the action density spectrum. The first three terms of this equation represent the local rate of change of action density and the propagation of action over geographical space respectively. The fourth term represents the shifts in relative frequency due to currents. The fifth term represents the depth and current induced refraction. The source term S on the right-hand side accounts for wave generation, dissipation of wave energy and non-linear wave-wave interactions. The model is driven by wave boundary conditions and local winds. The wave generation by wind is based on the feedback mechanism of Miles (Miles, 1957; Janssen 1991a); the wind speed used in SWAN is the wind speed at 10-*m* elevation, U_{10}.

The wave induced set-up in the model is computed using the vertically integrated momentum balance equation which, in the 2D case, incorporates the observation of Dingemans *et al*. (1987) that the rotation-free part of the wave force drives the set-up, while the divergence-free part drives the wave-induced currents. This then leads to the following approximation:

$$\nabla.(\vec{F} + gd\nabla\eta) = 0 \tag{2}$$

where η is the water surface elevation including the wave induced set-up; F is the wave force vector and d represents the total depth.

1.1.3 The Sediment Model

The sediment model is capable to simulating sediment transport and bottom level changes of both cohesionless and cohesive sediment. It uses various formulations for the sediment transport and mobility developed by researchers at-Deltares, as well as other institutions, and then uses continuity of sediment to determine bed level changes. While important, the sediment model is not a component of this work.

1.2 General Model Approach

1.2.1 Boundary Conditions

As mentioned above, in order to allow flow to leave the lateral boundaries with no artificial circulation, Roelvink and Walstra (2004) developed a Neumann lateral boundary condition for the FLOW model. This condition assumes that the longshore gradient of the mean sea surface is zero at the lateral boundaries of the grid; the

remaining dynamic variables would reach their "natural" values at the boundaries, and the resulting flow would be free of boundary-induced effects.

Since the Neumann boundary conditions require longshore uniform conditions at the lateral boundaries, coupling of the wave and hydrodynamic models requires care at these boundaries. The optimum method of doing this is by laterally extending the grid for the forcing wave model beyond the boundaries of the hydrodynamic model (Figure 1.1 left), thus keeping longshore irregularities in the forcing far away from the domain of interest. A major disadvantage of this approach is the increased computational time required for the wave model, which has typically been the bottleneck in the overall calculation time, particularly for stationary (equilibrium) conditions. We wish to investigate the effect of truncating this extraneous lateral extension has on the run time and the errors in the model.

Here we define the extension ratio A/B, where A is the length of the extension of the SWAN model grid on either side of the FLOW grid, and B is the overall longshore extent of the FLOW grid (Figure 1.1 right). The higher the ratio A/B, therefore, the longer the overall extent of the wave model grid is.

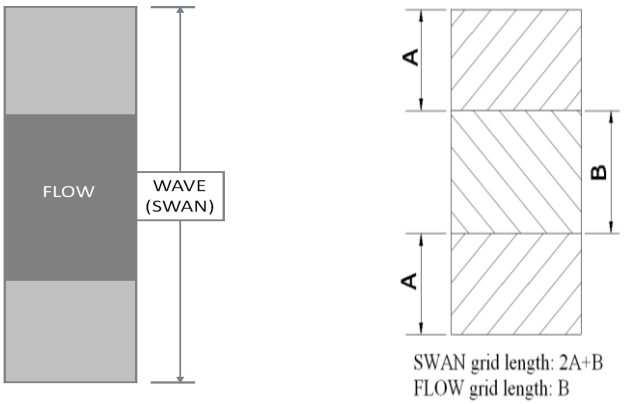

Figure 1.1 Sketch of grid extension (left) and definition of the extension ratio A/B.

1.2.2 Research Objective

In this thesis there are two intertwined objectives. The first objective relates to the model validation of the Delft-3D modeling system in nearshore applications. The second objective focuses on determining the effect of boundary errors on model response, and the development of methods to ameliorate these issues. Specific tasks of this research are:

1) to apply the perturbation method in order to develop a set of equations governing the spreading of the errors introduced at the cross-shore boundaries in the computational domain;
2) to implement spatio-temporal analysis methods such as Empirical Orthogonal Function (EOF) analysis to determine the overall scales of motion in the flow field and the extent of the variation of their response to the errors;
3) to use a critical-point analysis called swirling strength (Zhou *et al*., 1996) for quantifying and interpreting velocity-field data, especially the eddy features.

1.3 Data Sources

1.3.1 Duck94 Field Experiment

Duck94 field experiment was conducted in August, September and October 1994 near the Army Corps of Engineers' Field Research Facility pier located in Duck, North Carolina (shown in Fig. 1.2). The wave gauge arrangements and general map of the bathymetry at Duck is shown in Fig. 1.3. A bathymetry survey for the so-called "mini-grid", which is marked by the box, was conducted daily during the intensive study

period. The mini-grid surveys were merged with the larger, domain-sized bathymetry to yield wave model bathymetry for each day of the experiment.

The SWAN model grid consisted of 85 columns and 160 rows with grid spacing of 10 *m* in the cross-shore direction (*x*), and 15 *m* along the shore (*y*). The smaller FLOW grid lay inside the SWAN domain with 85 by 80 grid points with grid spacing of 10 *m* in *x* and 15 *m* in *y*. In order to satisfy the Neumann boundary condition, longshore uniform areas are extended by a few grid points into the FLOW domain on both side boundaries. Directional spectrum from the 8-*m* array (pressure gauges located on the 8-*m* contour about 900 *m* offshore) was used as offshore boundary to the wave model. The dates selected for model computation were based on the availability of mini-grid bathymetry surveys. Model simulation was conducted for every 3 hours and 132 cases were run. All SWAN runs were stationary for Duck94 in this study; waves do not change during the one hour flow computation. In addition, all model runs were made without wave-current interaction.

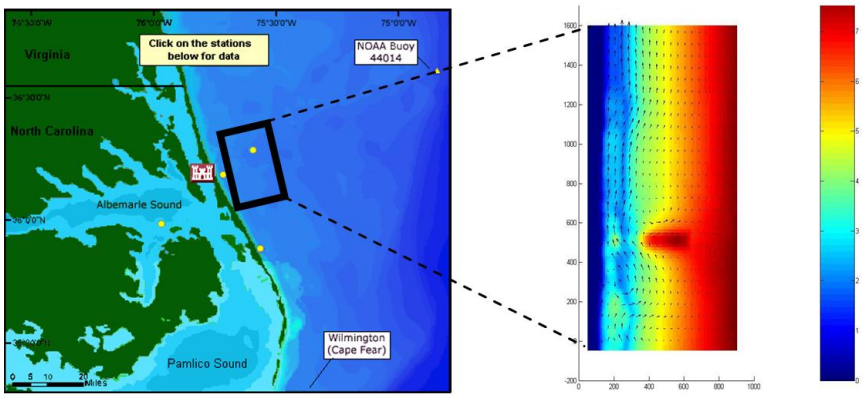

Figure 1.2 Duck, North Carolina (from http://frf.usace.army.mil/frf.shtml) and bathymetry of Delft3D area.

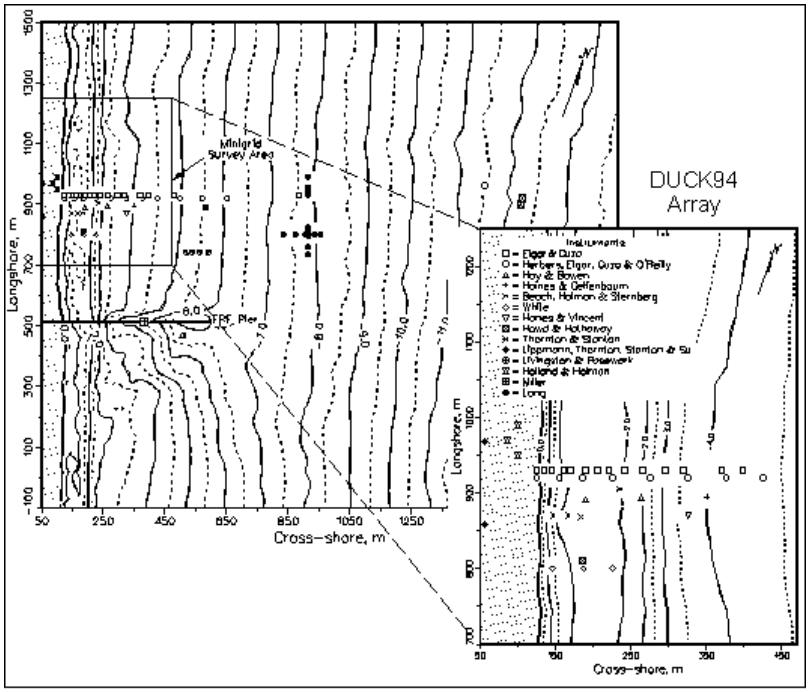

Figure 1.3 Instrumentation layout at Duck94 (from http://frf.usace.army.mil/duck94/DUCK94_overview.stm)

1.3.2 Nearshore Canyon Experiment (NCEX)

The data from the site of the Nearshore Canyon Experiment (NCEX), conducted near Scripps Institution of Oceanography (La Jolla, CA) in 2003, was used in this study. In addition, there are active relevant websites run by the Coastal Data Information Program (CDIP), which serve as the source of input data for our study. The bathymetric data was taken from surveys conducted during the experiment, while the offshore wave spectrum forcing for the model was made available through the CDIP web site for January 2010. The steep topography at the canyons could be expected to cause significant variation in nearshore wave energy; in particular, complex refraction effects are likely to focus/defocus wave energy at various locations alongshore, leading to strong longshore variation of energy. This expected spatial variation in sensitivity of the

overall model results to boundary errors was one of the reasons for selecting this as the study area.

Because forcing from the CDIP buoy is located about 8 *km* offshore, the SWAN model was first run over a larger domain (shown in Fig. 1.4 left), and the wave spectrum results along the offshore boundary of an approximately 1 *km* by 2 *km* grid (shown in Fig. 1.4 right) was written out to be used as the boundary condition for the SWAN runs over this smaller area of interest.

A computational grid resolution of 5 *m* in the cross-shore direction (*x*), and 15 *m* along the shore (*y*) was used in SWAN. We adopted higher resolution for FLOW, which is 2 *m* in *x* and 5 *m* in *y*. This was chosen to be sufficiently high to reduce the effect of numerical artifacts on the model results, and thereby maximize the impact of the input conditions. Model runs were conducted for every hour and 216 cases were run. All SWAN runs were stationary for NCEX cases in this study.

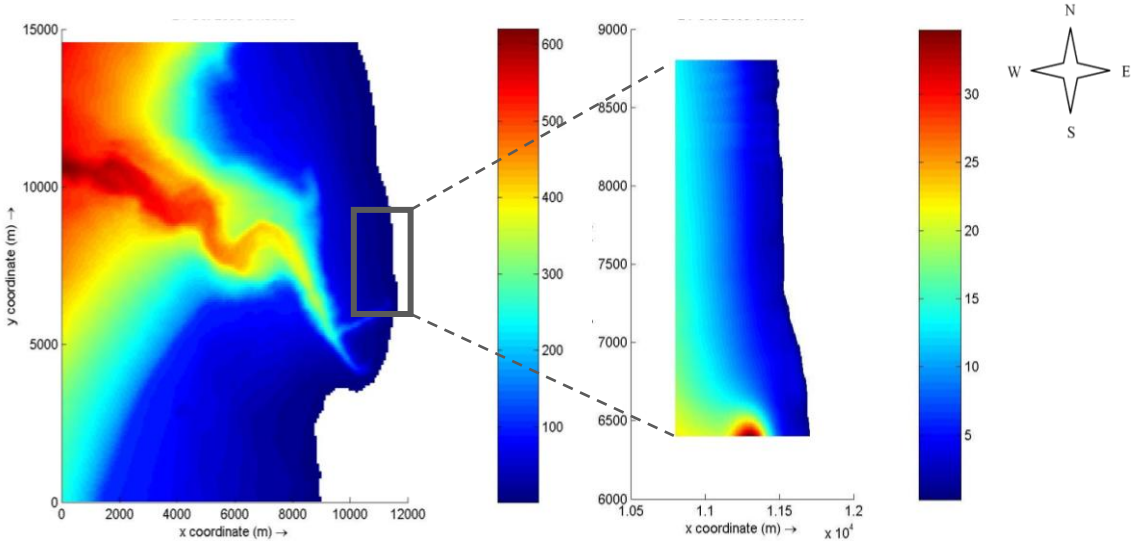

Figure 1.4 Bathymetry of over the extent of the larger WAVE domain and selected area of interest.

2. COMPARISON OF FIELD OBSERVATIONS AND MODEL EXPERIMENTS

The two-dimensional Delft3D model has been shown to be capable of simulating nearshore hydrodynamic processes such as wave, winds, flow, tides and so forth, over complex bathymetries where the use of a one-dimensional nearshore model (e.g. the Navy Standard Surf Model) would be inappropriate (Morris 2001). In this study we will use data from the Duck94 experiment to establish the accuracy of the basic model.

2.1 Model Parameters and Setup

For 2-D simulations, three roughness formulations (Manning, White-Colebrook and Chezy) can be selected at the roughness menu under the data group "physical parameters" of Delft3D. It has been shown that all the three formulations can produce good results if a proper empirical constant is chosen (Hsu *et al*., 2006). The bottom friction coefficient C_f is related to Chezy roughness coefficient C by definition:

$$C_f = g / C^2 \tag{3}$$

where g is the acceleration due to gravity. The default Chezy value is set at 65 in the Delft3D FLOW manual. For Manning formulation, the Chezy coefficient is related to the Manning roughness coefficient n by:

$$C = h^{1/6} / n \tag{4}$$

where h is the water depth. For W-C formulation, the Chezy coefficient is calculated from both water depth and geometrical roughness of Nikuradse k_s:

$$C = 18 * \log(12 * h / ks) \tag{5}$$

The optimal value of k_s based on Duck runs was found to be 0.003 m for the barred beach in Morris's investigation (Morris, 2001). As for the Manning formulation, the suggested default value for n is 0.02 in the Delft3D FLOW manual.

2.2 Comparisons of Delft3D Output to Data

To evaluate the model performance, comparison plots are presented in Figure 2.1-2.4. For each gauge, the maximum, mean, and minimum longshore current for the time period is shown. (The nearshore data are provided every 5 min, while the offshore data used for initialization represents a span of two hours, 16 min.) The figures show that Delft3D model based on default parameters works reasonably well for Duck94.

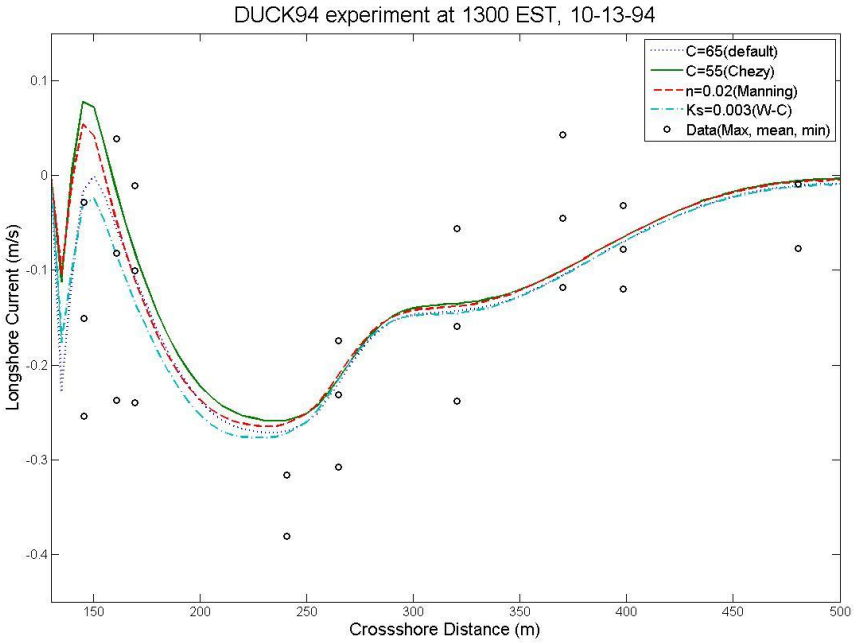

Figure 2.1 Comparison of longshore current from Delft3D to the Duck94 experiment data for the time period beginning at 1300 EST, 10-13-94

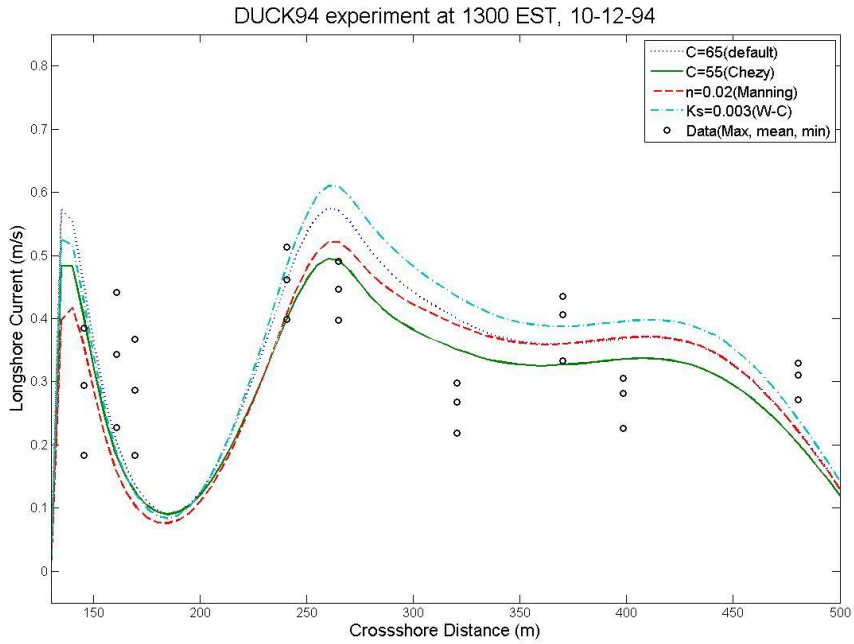

Figure 2.2 Comparison of longshore current from Delft3D to the Duck94 experiment data for the time period beginning at 1300 EST, 10-12-94

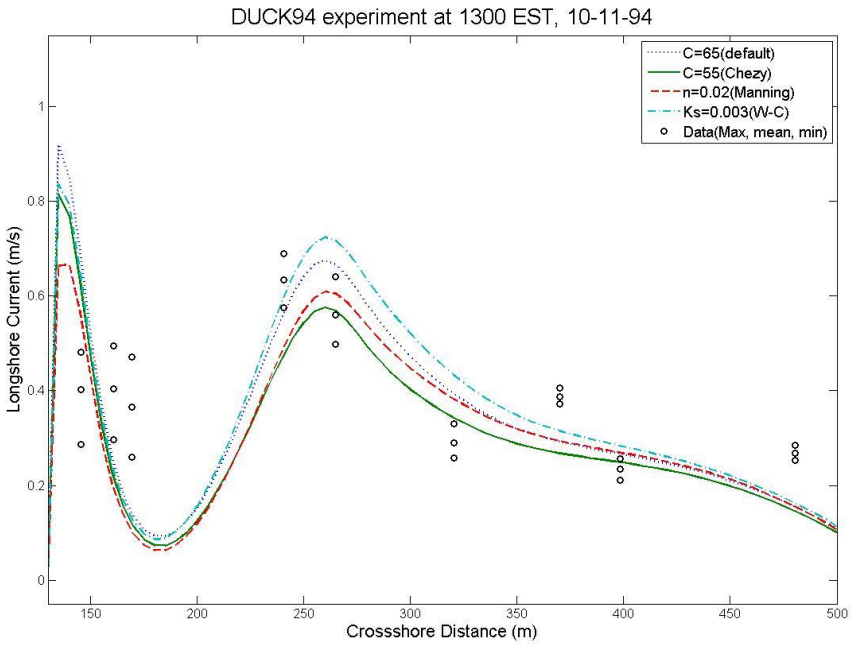

Figure 2.3 Comparison of longshore current from Delft3D to the Duck94 experiment data for the time period beginning at 1300 EST, 10-11-94

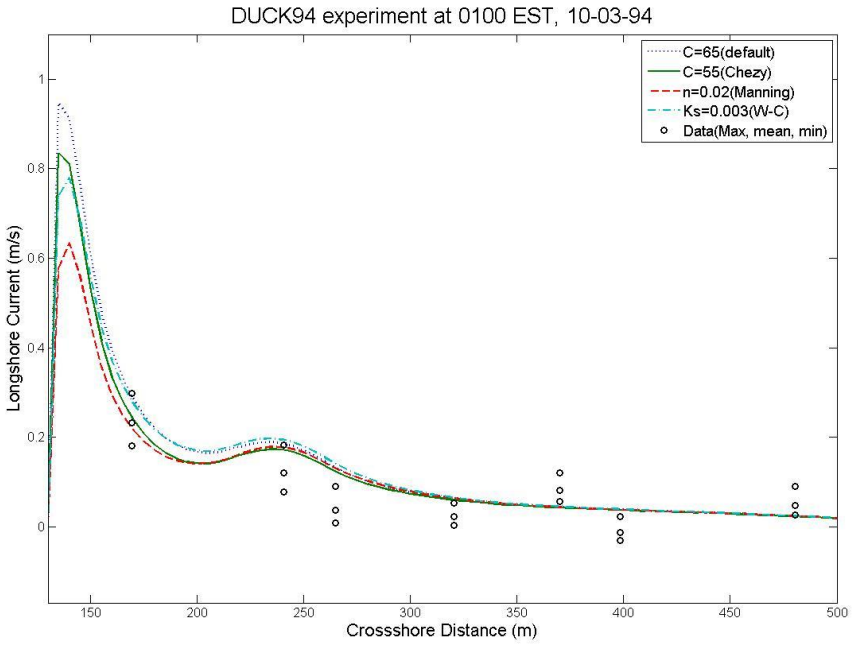

Figure 2.4 Comparison of longshore current from Delft3D to the Duck94 experiment data for the time period beginning at 0100 EST, 10-03-94

Figure 2.5-2.8 show representative comparisons of model output to data from the nearshore, cross-shore array. Again, the maximum, mean, and minimum wave height for the time period is shown for each gauge. Wave reformation shoreward of the bar is evident in some cases in both model results and data.

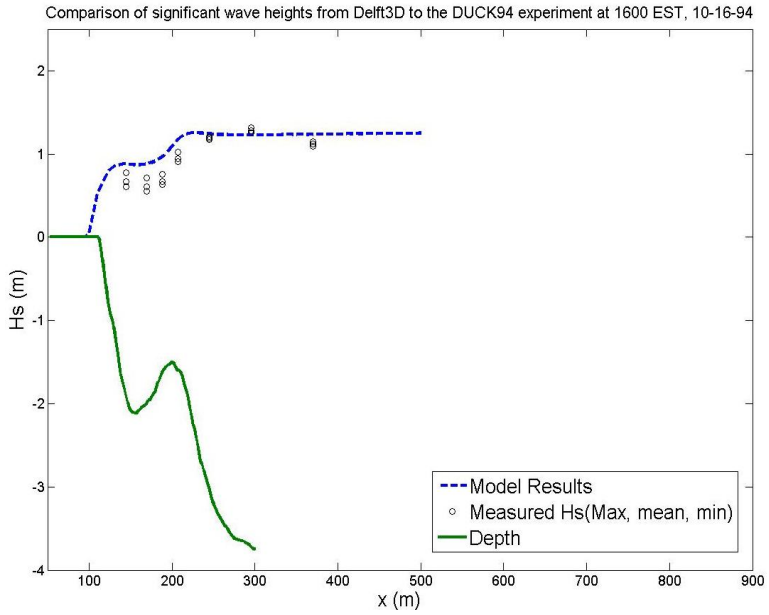

Figure 2.5 Comparison of significant wave heights from Delft3D to the Duck94 experiment data for the time period beginning at 1600 EST, 10-16-94

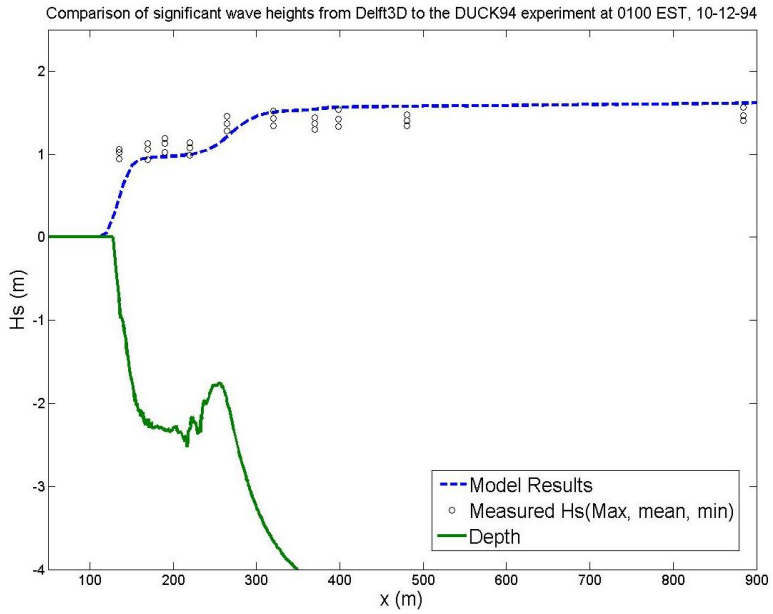

Figure 2.6 Comparison of significant wave heights from Delft3D to the Duck94 experiment data for the time period beginning at 0100 EST, 10-12-94

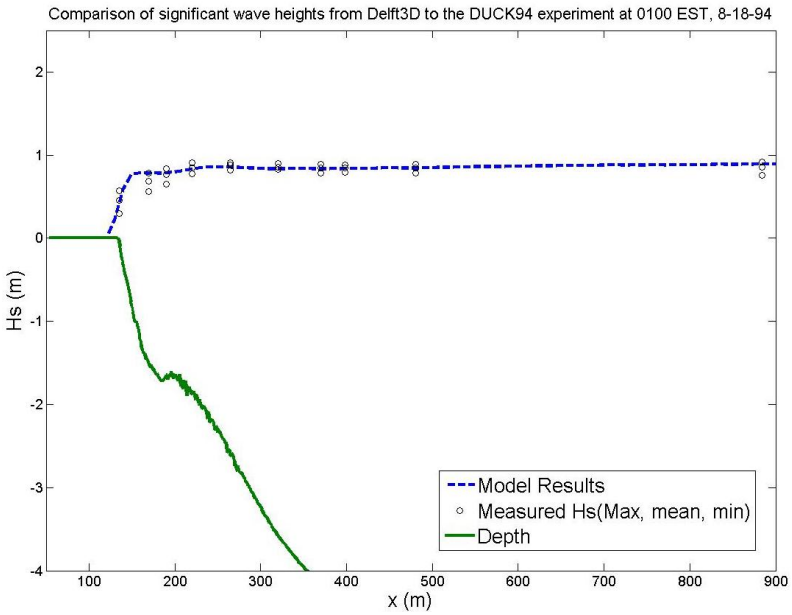

Figure 2.7 Comparison of significant wave heights from Delft3D to the Duck94 experiment data for the time period beginning at 0100 EST, 08-18-94

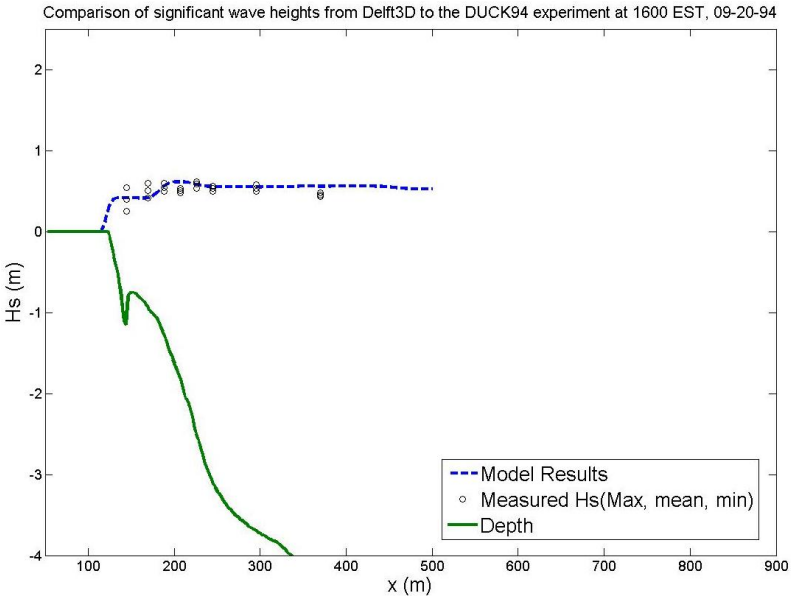

Figure 2.8 Comparison of significant wave heights from Delft3D to the Duck94 experiment data for the time period beginning at 1600 EST, 09-20-94

As mentioned above, the Delft3D model was run for 132 cases of Duck94 data. The scatter plots for both significant wave height and longshore current for ratio A/B equal to 50% are presented in Fig. 2.9-2.10. This analysis on the 'best' modeled field (A/B = 50%) yields our "Golden Standard" by which we can evaluate further possible degenerative effects of imposed errors defined relative to the standard on the boundaries. In addition, Figure 2.11-2.16 present comparisons for 40%, 30% and 25% cases, respectively.

The skill statistics for wave height and longshore current results are summarized in Table 1 and Table 2 respectively, where *R* represents the linear correlation coefficient, *slope* is the slope of the linear regression line (solid line), and *N* is the number of observations. Additionally, the root mean square error (RMSE) and mean absolute gross error (MAGE) are listed. It is clear that the model results agree reasonably well with

measurement. Obviously, both the RMSE and MAGE grow as the grid extension is decreased. It should be noted that the higher the ratio A/B, the more computational time is required of the model simulation.

With a reasonable degree of confidence in the model skill, we now can investigate the effect of errors on the possible deterioration of model performance. However, we have only confirmed the model performance in pointwise comparisons to data. Is it possible to systematically examine and evaluate the model performance in terms of spatial variation? Are there any certain spatial patterns we can track as the boundary errors increase? To address these questions, we will further introduce and interpret Empirical Orthogonal Function analysis in the next section.

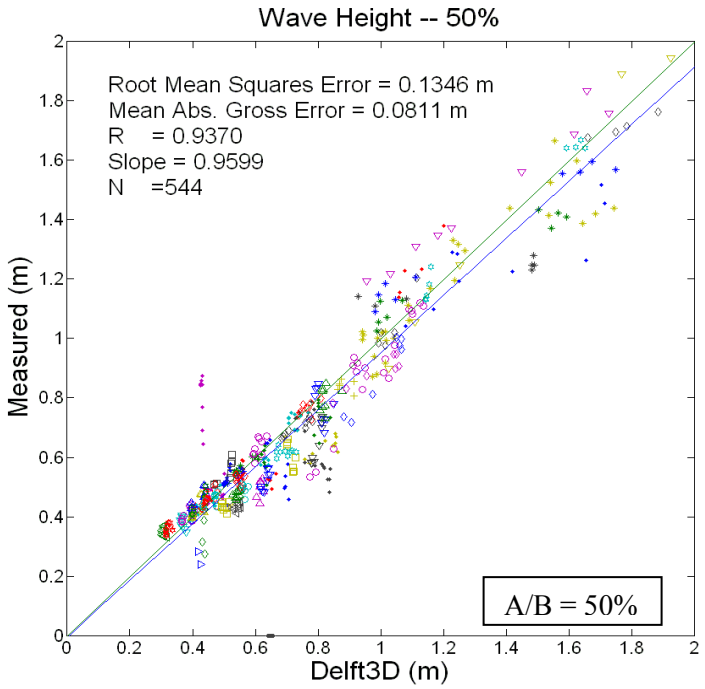

Figure 2.9 Scatter plots for wave height comparison with 50% grid extension.

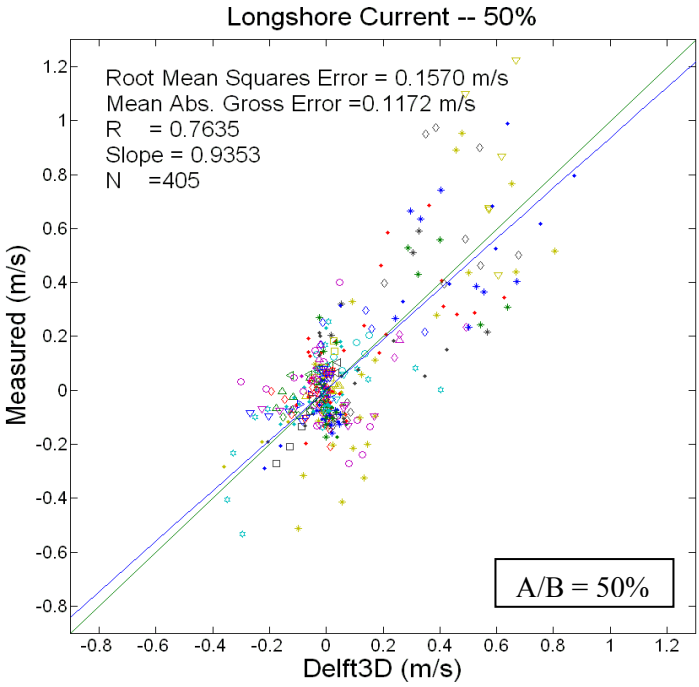

Figure 2.10 Scatter plots for longshore current comparison with 50% grid extension.

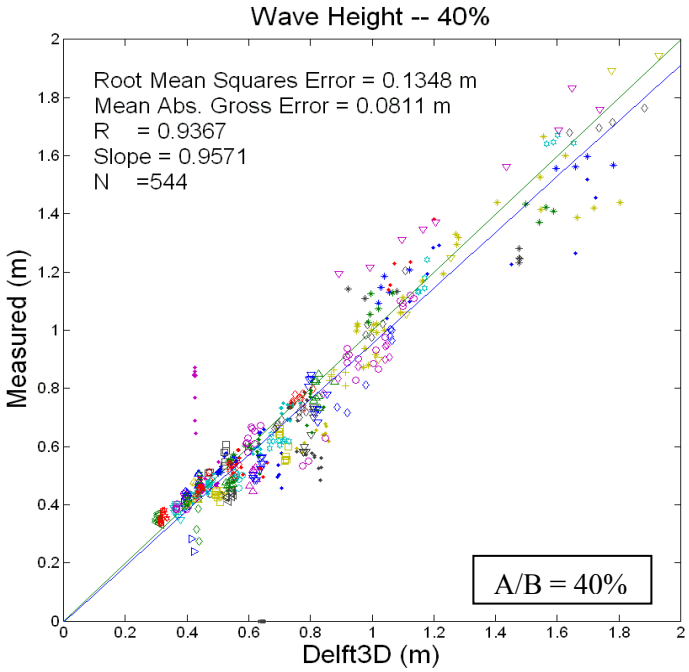

Figure 2.11 Scatter plots for wave height comparison with 40% grid extension.

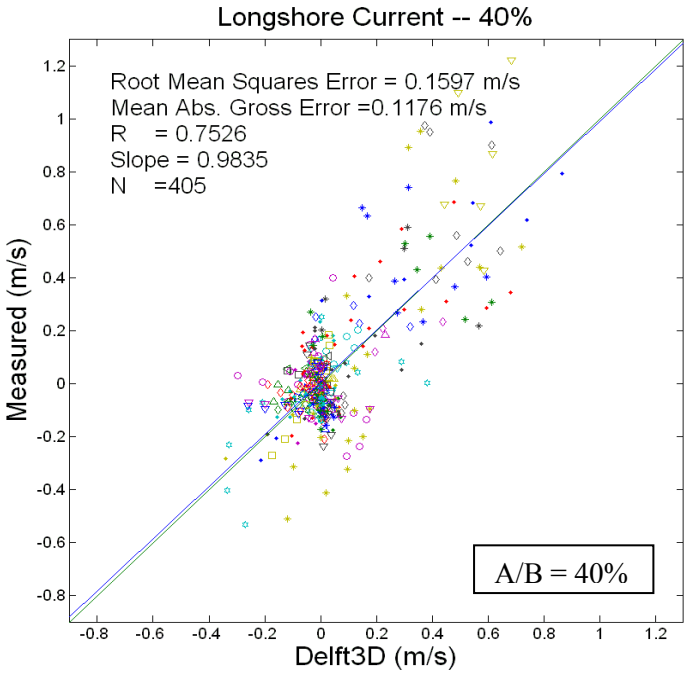

Figure 2.12 Scatter plots for longshore current comparison with 40% grid extension.

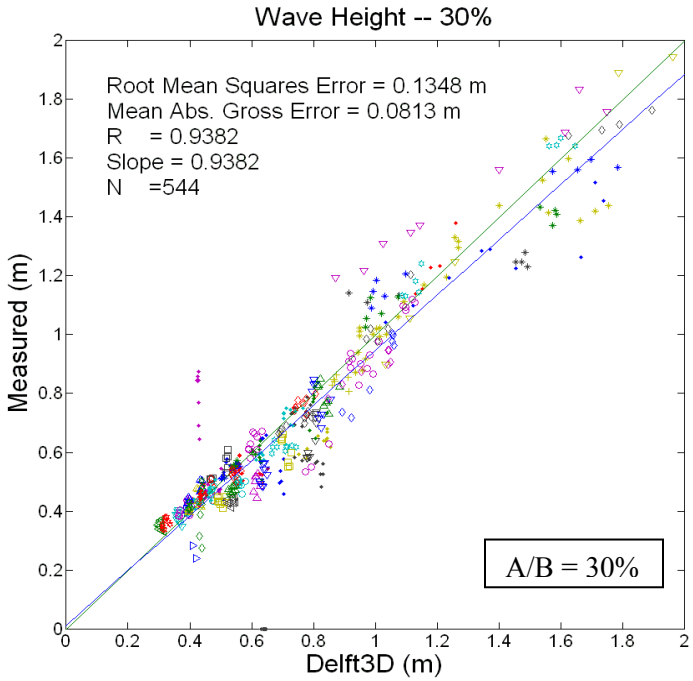

Figure 2.13 Scatter plots for wave height comparison with 30% grid extension.

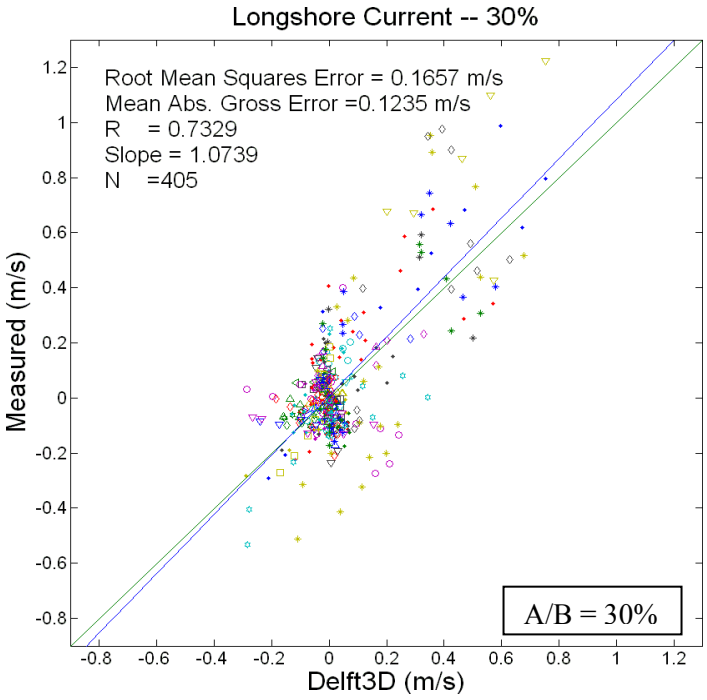

Figure 2.14 Scatter plots for longshore current comparison with 30% grid extension.

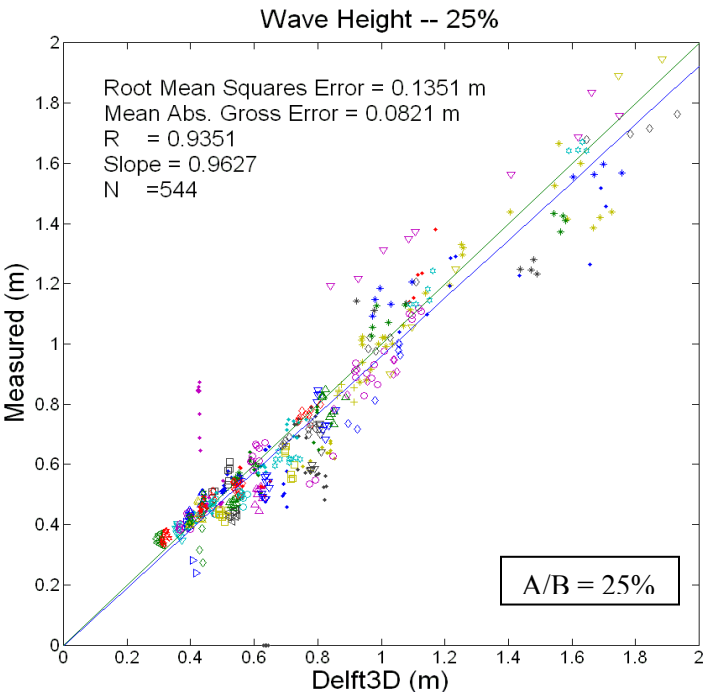

Figure 2.15 Scatter plots for wave height comparison with 25% grid extension.

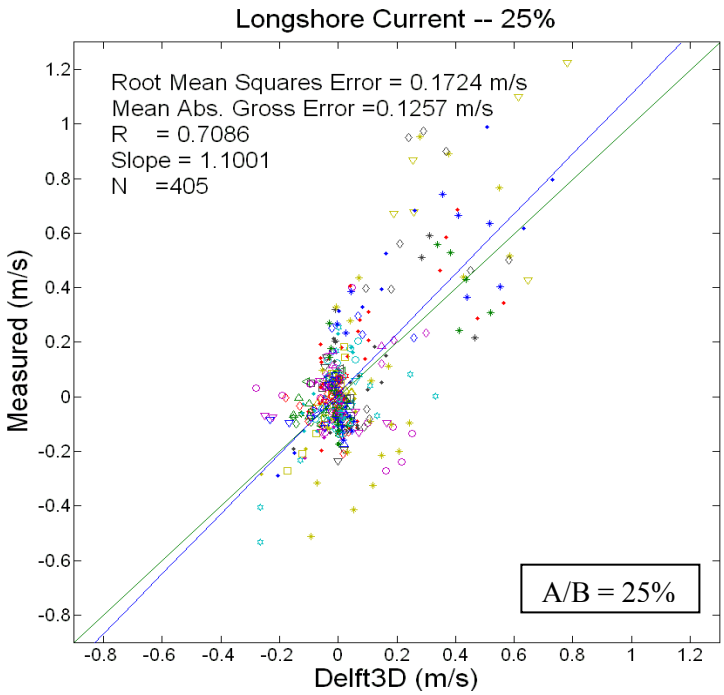

Figure 2.16 Scatter plots for longshore current comparison with 25% grid extension.

Table 1 Skill statistics for different grid extension selections of wave height at Duck94. See Figure 1.1 for grid extension ratio definition.

WAVE HEIGHT	RMSE (m)	MAGE (m)	R	Slope	N	Relative Running Time
A/B = 25%	0.1351	0.0821	0.9351	0.9627	544	0.835
A/B = 30%	0.1348	0.0813	0.9382	0.9382	544	0.871
A/B = 40%	0.1348	0.0811	0.9367	0.9571	544	0.941
A/B = 50%	0.1346	0.0811	0.937	0.9599	544	1.000

Table 2 Skill statistics for different grid extension selections of longshore current at Duck94.

LONGSHORE CURRENT	RMSE (m/s)	MAGE (m/s)	R	Slope	N
A/B = 25%	0.1724	0.1257	0.7086	1.1001	405
A/B = 30%	0.1657	0.1235	0.7329	1.0739	405
A/B = 40%	0.1597	0.1176	0.7526	0.9835	405
A/B = 50%	0.1570	0.1172	0.7635	0.9353	405

3. ERROR ANALYSIS

While it is always possible to compare model results to data to determine the optimum grid configuration, the point-to-point comparison does not offer any information on the spatial response of the model to the forcing, whether correct or erroneous. Is a poor data-model comparison due to a slight spatial shift of a highly-variable field by the model, or is it due to a complete inadequacy of the model physics or numerics?

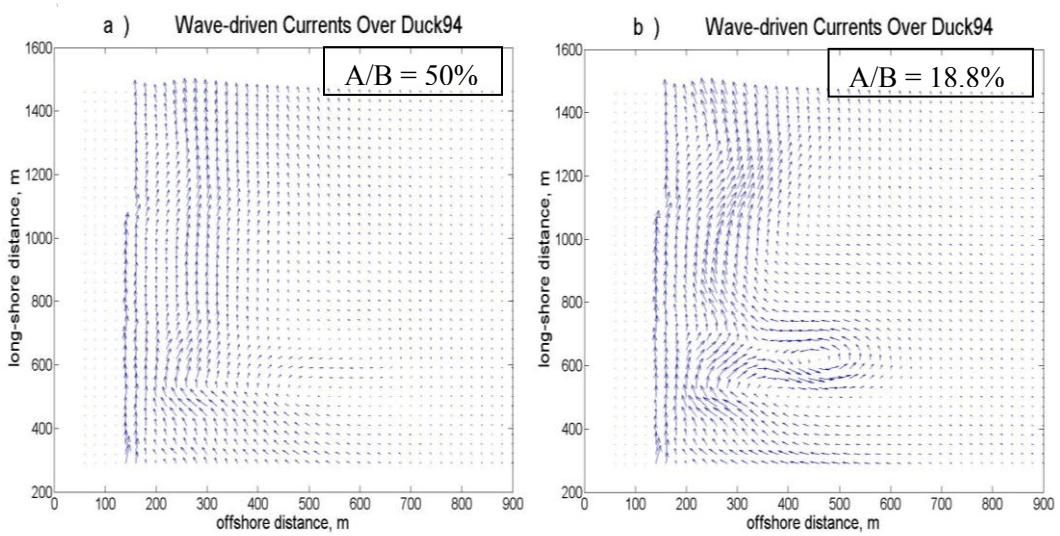

Figure 3.1. The effect of reduction of the lateral extent of SWAN grid on the simulation of wave-driven currents over Duck94 bathymetry. Shoreline is on the left of each plot of velocity vectors. a) A/B=50%; b) A/B=18.8%. See Figure 1.1 for grid extension ratio definition.

Figure 3.1 shows the flow field near the boundary for several values of ratio A/B. As the ratio becomes smaller, irregularities in the forcing field from the waves begins to effectively pollute the interior of the hydrodynamic model domain. This is demonstrated by the development of an eddy in the domain, which strengthens as A/B reduces.

Despite this, the patterns elsewhere seem reasonably similar, indicating that reliance on a data-model comparison alone may not raise issues of concern elsewhere in the domain.

3.1 Perturbation Analysis

A perturbation method is initially used to develop a set of equations governing the spreading of the errors introduced at the cross-shore boundaries in the computational domain of FLOW model. We start from Longuet-Higgins (1970b) one-dimensional longshore momentum balance, with the wave forcing represented by an energy decay based on a monochromatic wave breaking on a planar beach:

$$-\tau_{by} = \sin\theta \frac{E}{2d}\left(\frac{5-6\sin^2\theta}{\cos\theta}\right)\frac{\partial d}{\partial x} - \frac{\partial}{\partial x}\left(\mu_E d \frac{\partial V}{\partial x}\right) \tag{6}$$

where $-\tau_{by}$ is the bottom stress; θ is the incident wave direction with respect to shore normal; d is the total water depth; μ_E is the eddy viscosity coefficient; and V is the longshore current.

$$\mu_E = \rho N x \sqrt{gd} \tag{7}$$

where $0 < N \leq 0.016$. We note here that the FLOW model would effectively reduce to this equation under the relevant assumptions.

We assume that the waveheight decays linearly with depth, endemic of a spilling breaker:

$$H = Kd \tag{8}$$

where the parameter *K* is typically 0.78, and the wave celerity $C = \sqrt{gd}$ because of the shallow water assumption. We can express the energy *E* in terms of the spilling breaker assumption:

$$E = \frac{1}{8}\rho g H^2 = \frac{1}{8}\rho g K^2 d^2 \tag{9}$$

We use the weak-current assumption (the mean current is much smaller than the orbital velocity) for the bottom stress:

$$\tau_{by} = \frac{\rho f u_{\max} V}{4\pi} = \frac{\rho f K C V}{8\pi} \tag{10}$$

where ρ is the fluid density, *f* is the bottom friction coefficient and u_{max} is the maximum orbital velocity at the bottom, and $u_{max} = KC/2$ if we use the shallow water and spilling breaker assumptions.

We further assume that the slope is expressible as:

$$\frac{\partial d}{\partial x} = -s \tag{11}$$

where *x* axis is now positive offshore.

Finally we obtain:

$$\frac{\rho f C K}{8\pi} V = \frac{\sin\theta}{2d}\left(\frac{1}{8}\rho g K^2 d^2 \left[\frac{5 - 6\sin^2\theta}{\cos\theta}\right]\right) s + \frac{\partial}{\partial x}\left(\mu_E d \frac{\partial V}{\partial x}\right) \tag{12}$$

which is the longshore momentum balance between bottom friction (represented by the left hand side term), radiation stress gradients (first term on the right hand side) and lateral mixing (second term on the right hand side).

In order to investigate the sensitivity of this result to errors in boundary conditions in an analytic manner, we express the longshore velocity V and wave energy coefficient K as:

$$V = V_0 + \varepsilon V_1 \tag{13}$$

$$K = K_0 + \varepsilon K_1 \tag{14}$$

where the subscript 0 refers to the "correct" value and the subscript 1 refers to a residual (in the case of velocity) or error (in the case of wave energy coefficient). The parameter ε is the expansion parameter that is much smaller than unity. Substitution of (13) and (14) into governing equation (12), and separating the orders yields the $O(1)$ equation:

$$\frac{\rho f C K_0}{8\pi} V_0 = \frac{\sin\theta}{2d}\left(\frac{1}{8}\rho g {K_0}^2 d^2 \left[\frac{5-6\sin^2\theta}{\cos\theta}\right]\right) s + \frac{\partial}{\partial x}\left(\mu_E d \frac{\partial V_0}{\partial x}\right) \tag{15}$$

and the $O(\varepsilon)$ equation:

$$\frac{\rho f C K_1}{8\pi} V_0 = \frac{1}{8}\sin\theta \rho g d s \left(\frac{5-6\sin^2\theta}{\cos\theta}\right) K_0 K_1 + \frac{\partial}{\partial x}\left(\mu_E d \frac{\partial V_1}{\partial x}\right) - \frac{\rho f C K_0}{8\pi} V_1 \tag{16}$$

Herein the $O(1)$ problem is identical to the situation expressed in Longuet-Higgins (1970a,b); the solution is:

$$\overline{V}_0 = B_1 \overline{X}^{P_1} + A_1 \overline{X}; \qquad 0 \le X \le 1 \tag{17}$$

$$\overline{V}_0 = B_2 \overline{X}^{P_2}; \qquad X > 1 \tag{18}$$

where

$$\overline{V}_0 = \frac{V_0}{V_{nm}} \tag{19}$$

and V_{nm} is the longshore current with no lateral mixing:

$$V_{nm} = \frac{gsK_0}{f}\frac{\pi}{2}\left(\frac{\sin\theta}{c}\right)\left(\frac{5-6\sin^2\theta}{\cos\theta}\right)d \tag{20}$$

Further:

$$B_1 = \left(\frac{P_2 - 1}{P_1 - P_2}\right)A_1; \qquad B_2 = \left(\frac{P_1 - 1}{P_1 - P_2}\right)A_1 \tag{21}$$

$$A_1 = \frac{1}{1-\frac{5p}{2}}; P \ne \frac{2}{5} \tag{22}$$

and the parameter P_1 and P_2 are the roots of:

$$P_{1,2} = -\frac{3}{4} \pm \sqrt{\frac{9}{16} + \frac{1}{P}}; P_1 > 0, P_2 < 0 \tag{23}$$

where:

$$P = \frac{8\pi Ns}{fK_0} \tag{24}$$

The $O(\varepsilon)$ problem (16) is solved in a similar manner. Substituting equation (7) into equation (16) and rearranging yields:

$$\frac{fCK_1}{8\pi}V_0 = \frac{1}{8}\sin\theta gds\left(\frac{5-6\sin^2\theta}{\cos\theta}\right)K_0K_1 + N\sqrt{g}\,\frac{\partial}{\partial x}\left(xd^{3/2}\frac{\partial V_1}{\partial x}\right) - \frac{fCK_0}{8\pi}V_1 \qquad (25)$$

For a plane beach, $-d = sx$, $-C = \sqrt{gd} = \sqrt{gsx}$, and using the following nondimensionalization:

$$X' = \frac{X}{X_b} \qquad (26)$$

where x_b is the location of breaking. Thus we are re-expressing the problem such that the solution is the fraction of residual current due to errors in the estimation of wave energy coefficient. Substituting this nondimensionalization into (25) gives:

$$V_0 = GX'^{1/2} + QX'^{-1/2}\frac{\partial}{\partial x'}\left(X'^{5/2}\frac{\partial V_1}{\partial x'}\right) - \frac{K_0}{K_1}V_1 \qquad (27)$$

where

$$G = \frac{\pi}{\rho}\sin\theta g^{1/2}s^{3/2}X_b^{1/2}\left(\frac{5-6\sin^2\theta}{\cos\theta}\right)K_0 \qquad Q = \frac{8\pi Ns}{fK_1} \qquad (28)$$

We then assume that the residual current is only appreciable inside the surf zone ($X' \le 1$) and dropping primes:

$$QX^2\frac{\partial^2 V_1}{\partial X^2} + Q\frac{5}{2}X\frac{\partial V_1}{\partial X} - \frac{K_0}{K_1}V_1 = V_0 - GX^{1/2}; 0 \le X \le 1$$

$$0; \quad X > 1 \qquad (29)$$

The homogeneous solution to (29) is similar to that for the *O*(1) solution:

$$V_H = BX^Q \tag{30}$$

where

$$Q^2 + \frac{3}{2}Q - \frac{K_0}{K_1}\frac{1}{Q} = 0 \tag{31}$$

$$Q_{1,2} = -\frac{3}{4} \pm \sqrt{\frac{9}{16} + \frac{K_0}{K_1}\frac{1}{Q}}; Q_1 > 0, Q_2 < 0 \tag{32}$$

We now determine the particular solution V_{1P} by assuming:

$$V_{1P} = A_1 X^{1/2} + A_2 \tag{33}$$

Thus:

$$V_1 = B_{11}X^{Q_1} + A_1 X^{1/2} + A_2; 0 \le X \le 1$$

$$V_1 = B_{12}X^{Q_2}; \qquad X > 1 \tag{34}$$

where coefficients A_1, A_2, B_{11} and B_{12} are determined by (35) and (36):

$$A_1 = \frac{G}{\frac{K_0}{K_1} - Q_1}\left(Q_1 \neq \frac{K_0}{K_1}\right); A_2 = -\frac{K_1}{K_0}V_0; \tag{35}$$

$$B_{11} = \frac{A_1 Q_2 + A_2 Q_2 - \frac{A_1}{2}}{Q_1 - Q_2}; B_{12} = \frac{A_1 Q_1 + A_2 Q_1 - \frac{A_1}{2}}{Q_1 - Q_2}; \tag{36}$$

A plot of the solution for various values of $F = K_1/K_0$ and mixing parameter Q appears in Figure 3.2. Since parameter G is a constant, we make $G = 0.01$. It is apparent that the mixing serves to ameliorate the effects of wave energy error for most of the range of the surf zone; little mixing (small Q) causes a larger value of V_1/V_0 through more of the surf zone than greater mixing (large Q). More importantly, the normalized residual velocity has a maximum value of F. Thus, the percentage error in the velocity is the percentage uncertainty in the wave energy coefficient.

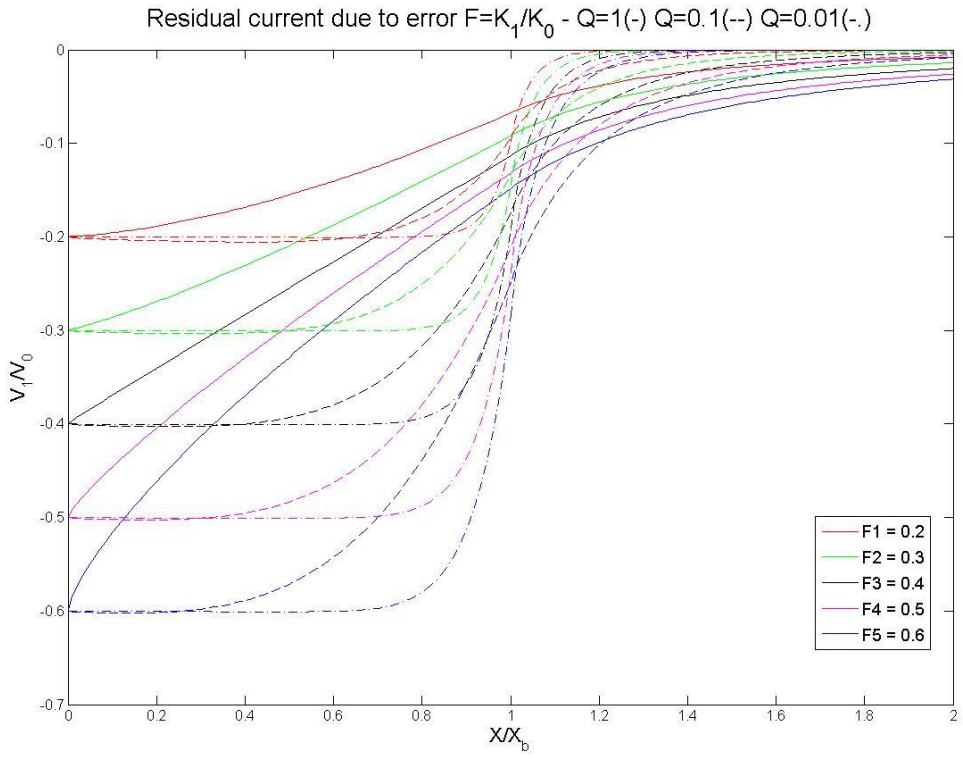

Figure 3.2 Normalized residual velocity for several values of mixing parameter P and percentage error in wave energy coefficient K.

3.2 Empirical Orthogonal Functions

The perturbation method would become very complicated for general cases and a way to investigate this numerically is therefore very necessary. Empirical Orthogonal Function (EOF) analysis offers a compact description of the spatial and variability of data series in terms of orthogonal functions or statistical modes (Kaihatu *et al.,* 1998). The first reference we could find to the application of EOF analysis to geophysical fluid dynamics is a report by Edward Lorenz (1956) in which he developed the statistical weather forecasting and coined the term "EOF". (Derivation of EOFs is shown in Appendix A).

As outlined by Davis (1976), two advantages of a statistical EOF description of the data are: 1. EOFs provide the most efficient method of compressing the data (a very few empirical modes can be used to describe the fundamental variability in a large data set); and 2. EOFs may be regarded as uncorrelated modes of variability of the data field.

As a start, we used EOF analysis to decompose time series of spatially-distributed current fields into separate, linearly independent modes which cascade in variance with increasing mode number. In general, the analysis herein addresses the two-dimensional behavior of the model response in the face of lateral boundary condition errors.

We will perform this analysis on a "best" modeled field, yielding a standard by which we can evaluate the effects of imposed errors on the lateral boundaries, such as seen in Figure 3.1. The separation into modes will allow a comparison to determine which modes are most affected by these errors, which in turn helps determine the

relevant scales of motion most vulnerable to errors. The result will allow value judgments concerning the important modes to be made and allow for the establishment of a balance between the desired level of accuracy and expediency.

3.3 Model Output

We used the model results as data for EOF analysis. Eleven stations, marked with stars in Figure 3.3, were defined in the FLOW domain of NCEX simulations. Water depth increases from right to left on this bathymetry map.

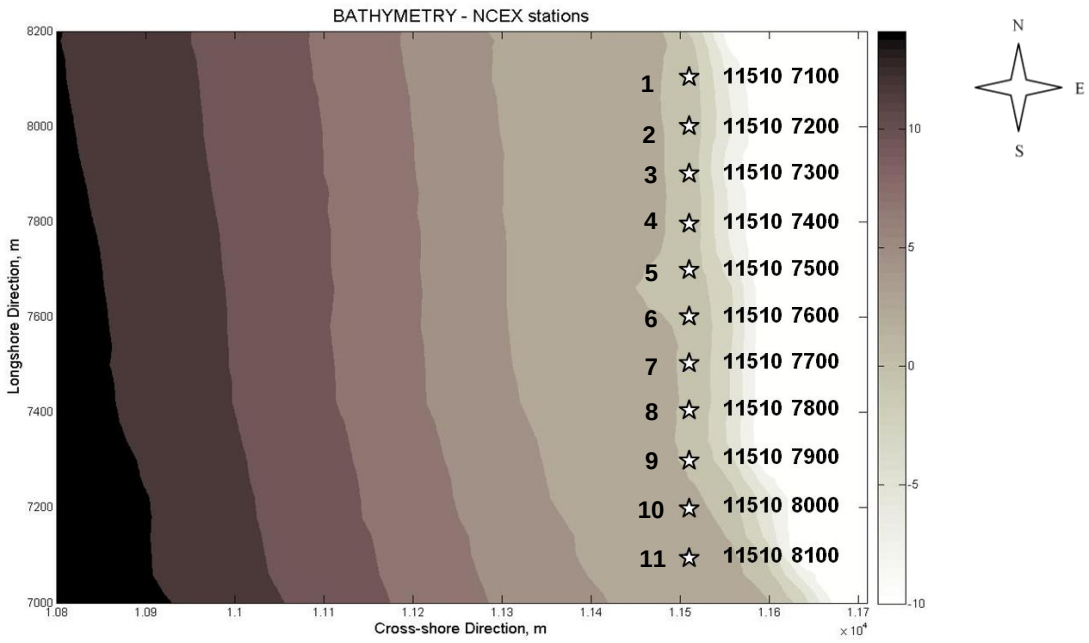

Figure 3.3 Layout of NCEX stations (coordinates display on the right) for Delft3D output.

Figure 3.4-3.6 show the time series of cross-shore current, longshore current and wave height respectively with 50% grid extension ratio for eleven stations. And the time series for 25% grid extension ratio are shown in Figure 3.7-3.9. Top panels (of Figure

3.4-3.9) present daily time series from January 1st, 2010 to January 31st, 2010. In order to obtain more data with high variance for EOF analysis, model runs with hourly initial wave spectrum (instead of a single representative daily spectrum) were also conducted, shown in the middle panels, from 0100 EST of January 1st, 2010 to 2300 EST of January 31st, 2010. We zoomed into the boxes to see the hourly time series features more clearly, as seen in the bottom panels. The selected hourly time series, marked by the box in the middle panels, spanned January 9th - January 17th.

Straightforward comparison between the time series for 50% ratio and 25% ratio cases is not possible; we thus calculate and display a histogram for each variable. These are shown in Figure 3.10-3.12. Since we obtained great variance near the coastline from south to north in the FLOW domain, we divided the stations into three parts: north (Station 1-3), middle (Station 4-7) and south (Station 8-11). It is apparent that the introduction of boundary errors affects the model's ability to simulate southward (negative) longshore currents, especially in Station 4-7 (shown in the middle panels of Figure 3.11).

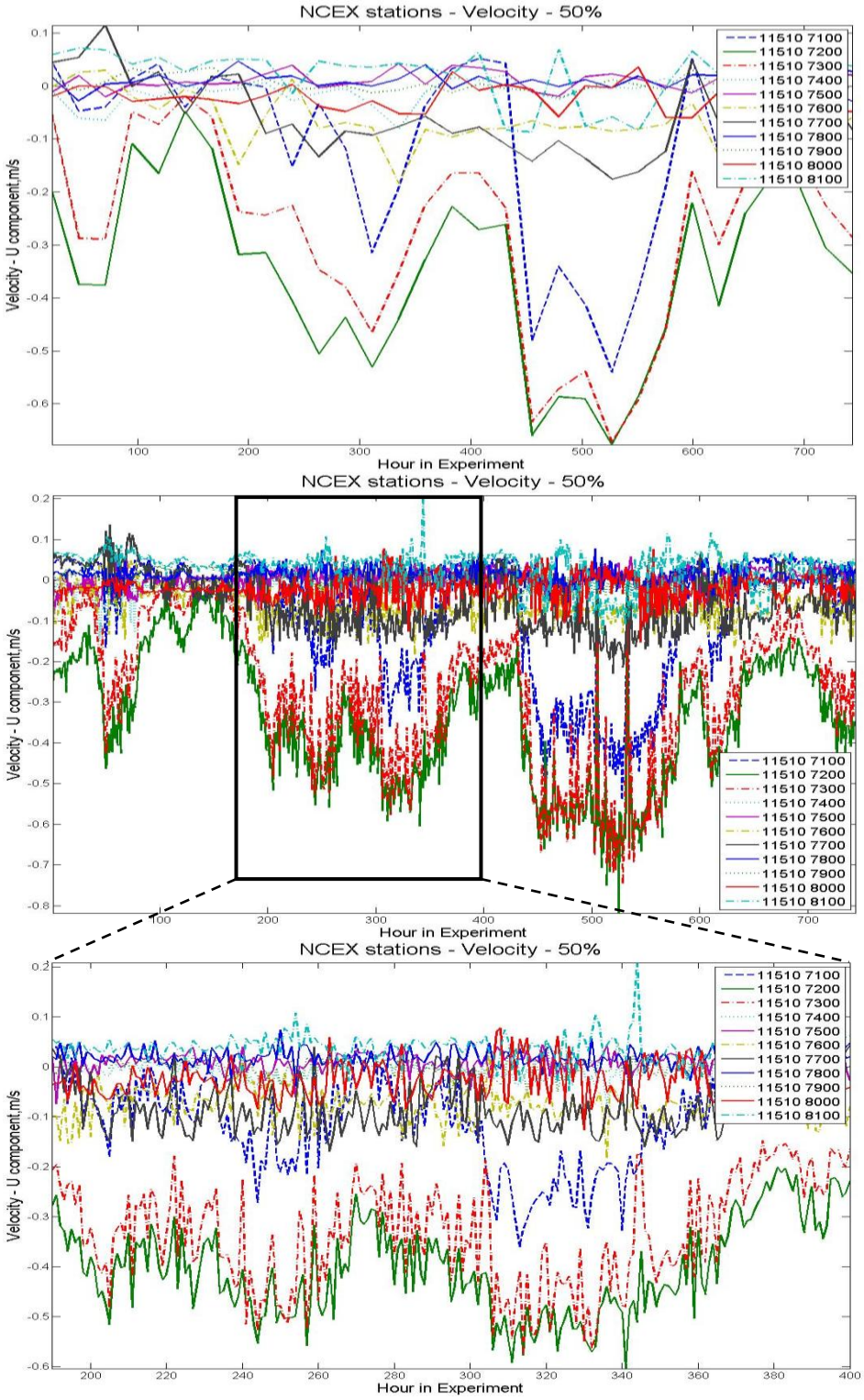

Figure 3.4 Time series of cross-shore current of NCEX stations with 50% grid extension ratio.

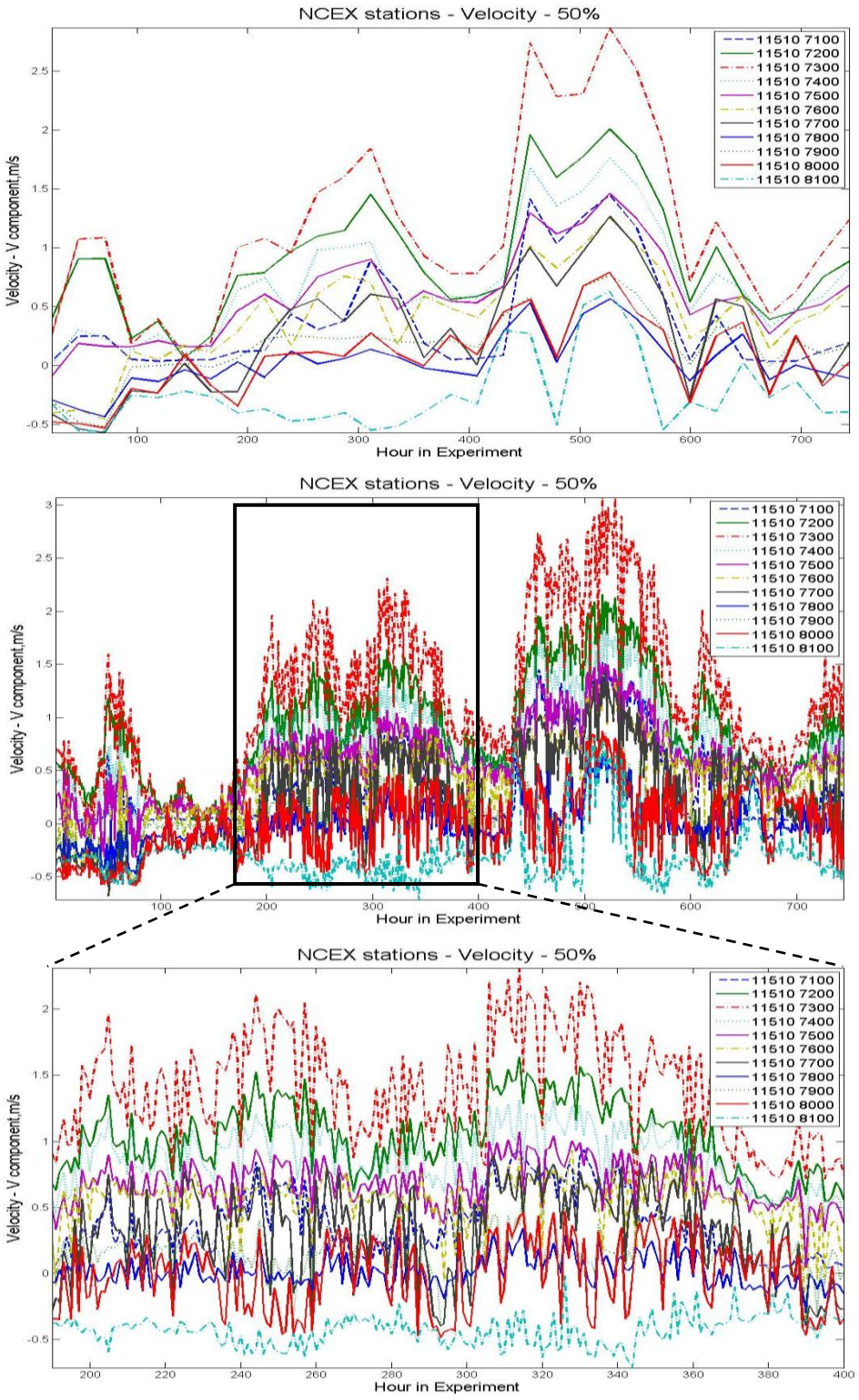

Figure 3.5 Time series of longshore current of NCEX stations with 50% grid extension ratio.

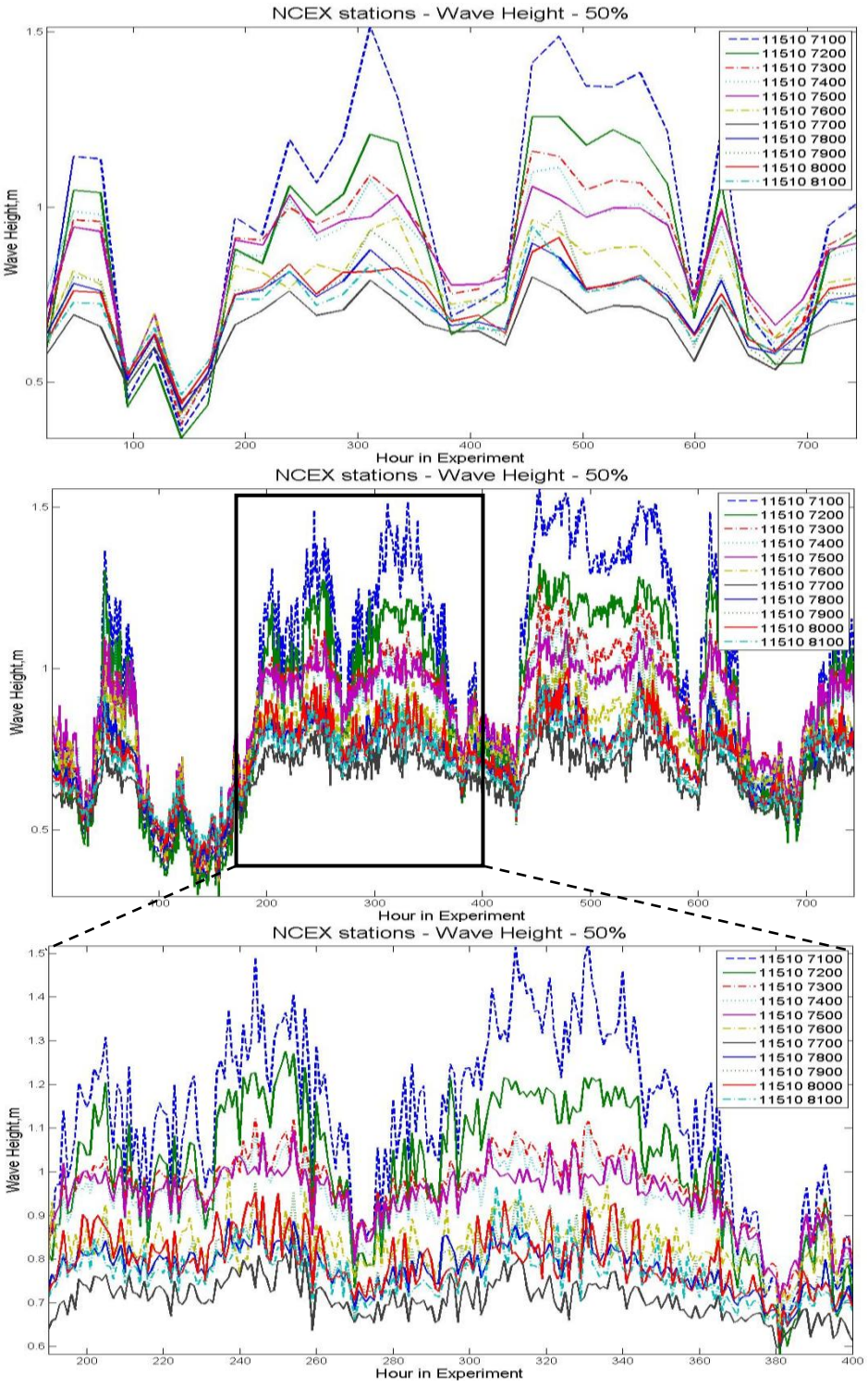

Figure 3.6 Time series of wave height of NCEX stations with 50% grid extension ratio.

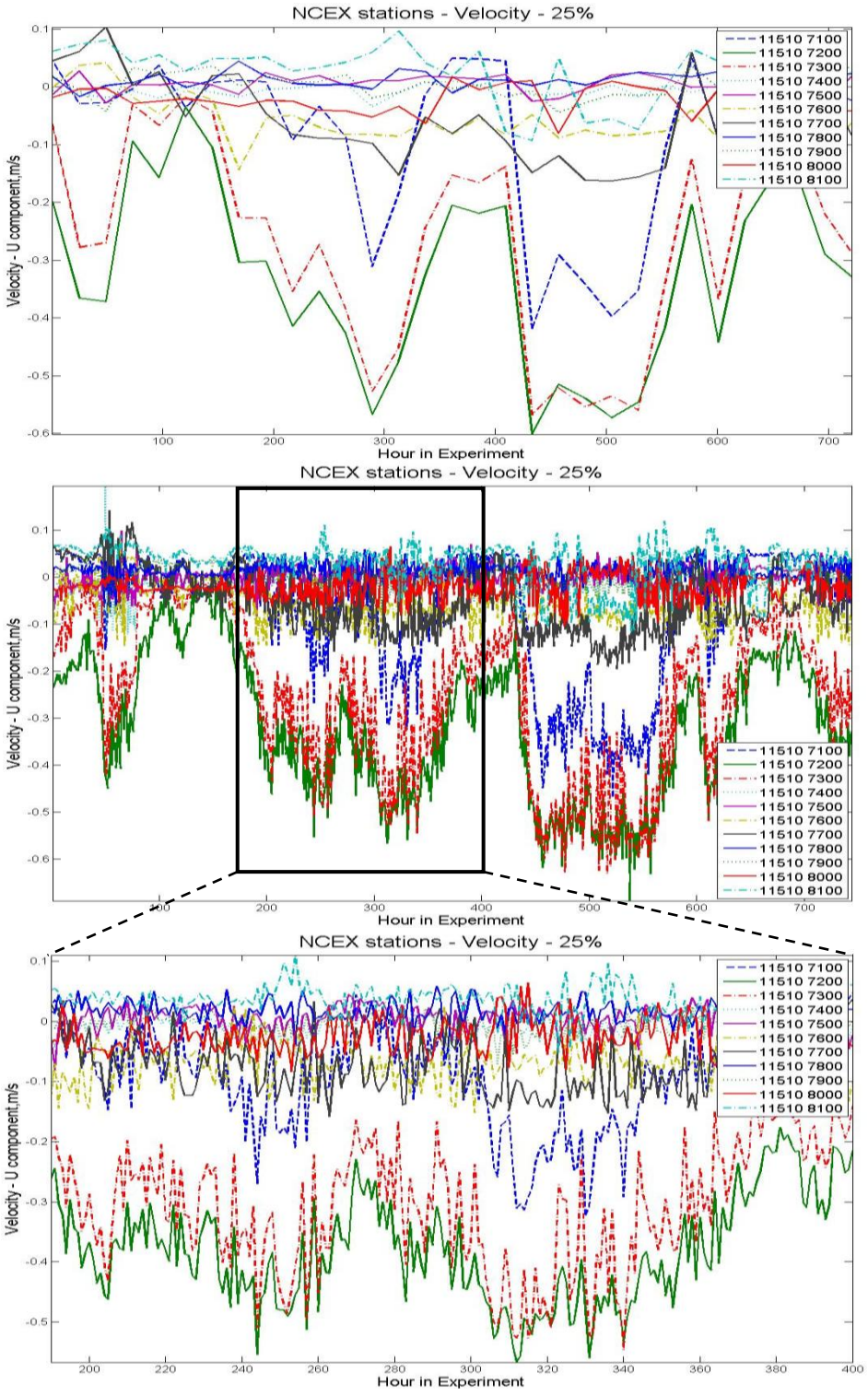

Figure 3.7 Time series of cross-shore current of NCEX stations with 25% grid extension ratio.

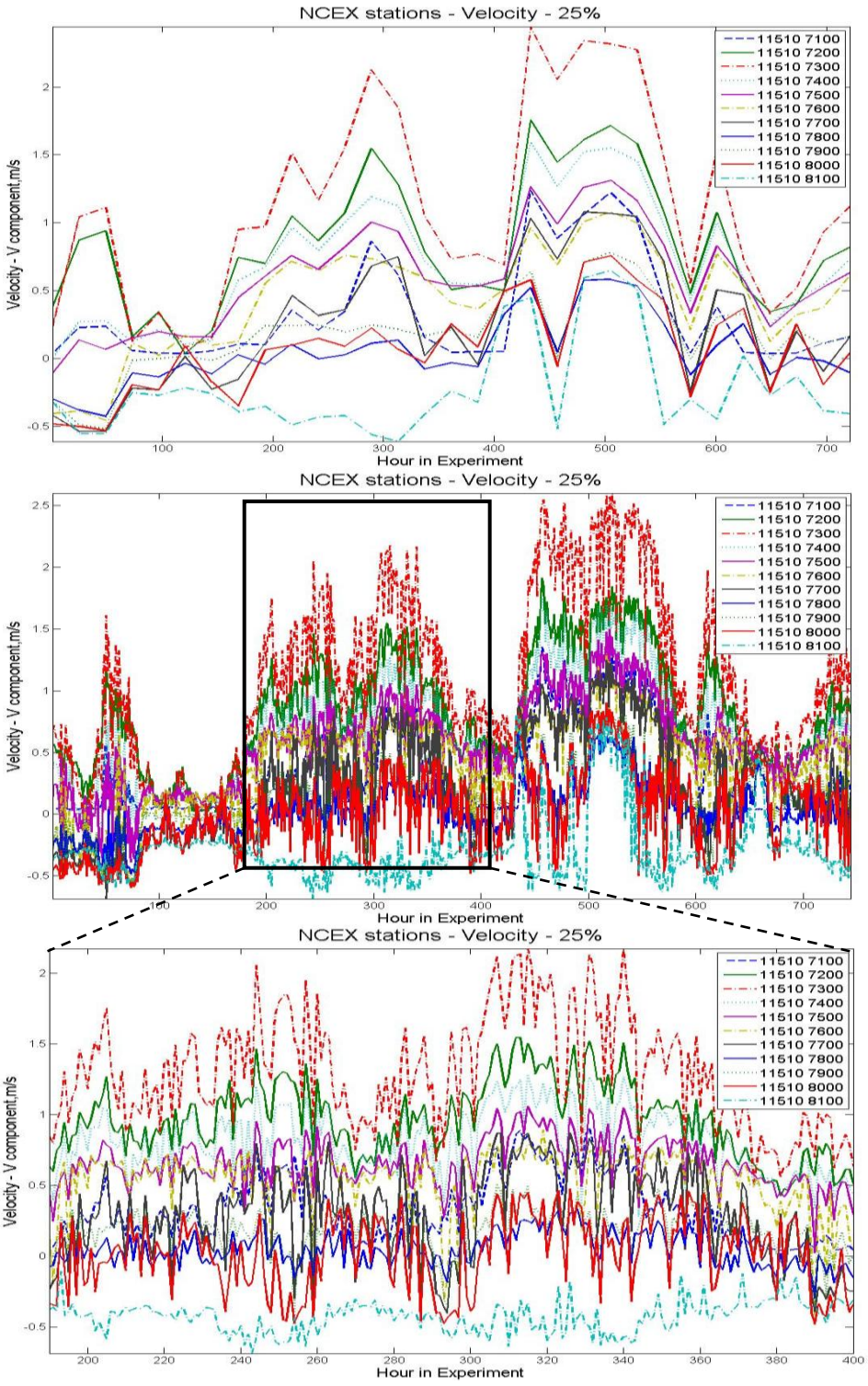

Figure 3.8 Time series of longshore current of NCEX stations with 25% grid extension ratio.

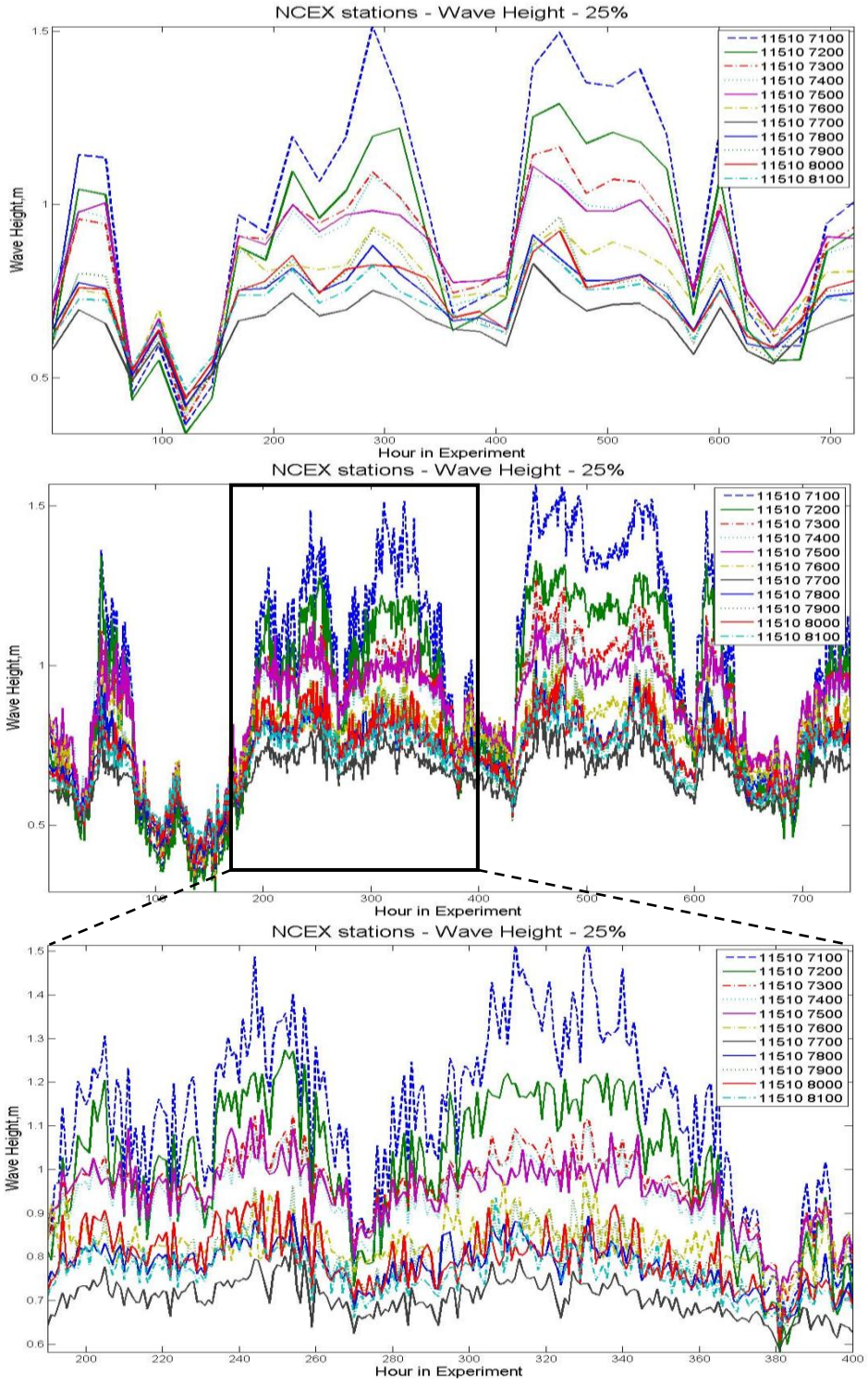

Figure 3.9 Time series of wave height of NCEX stations with 25% grid extension ratio.

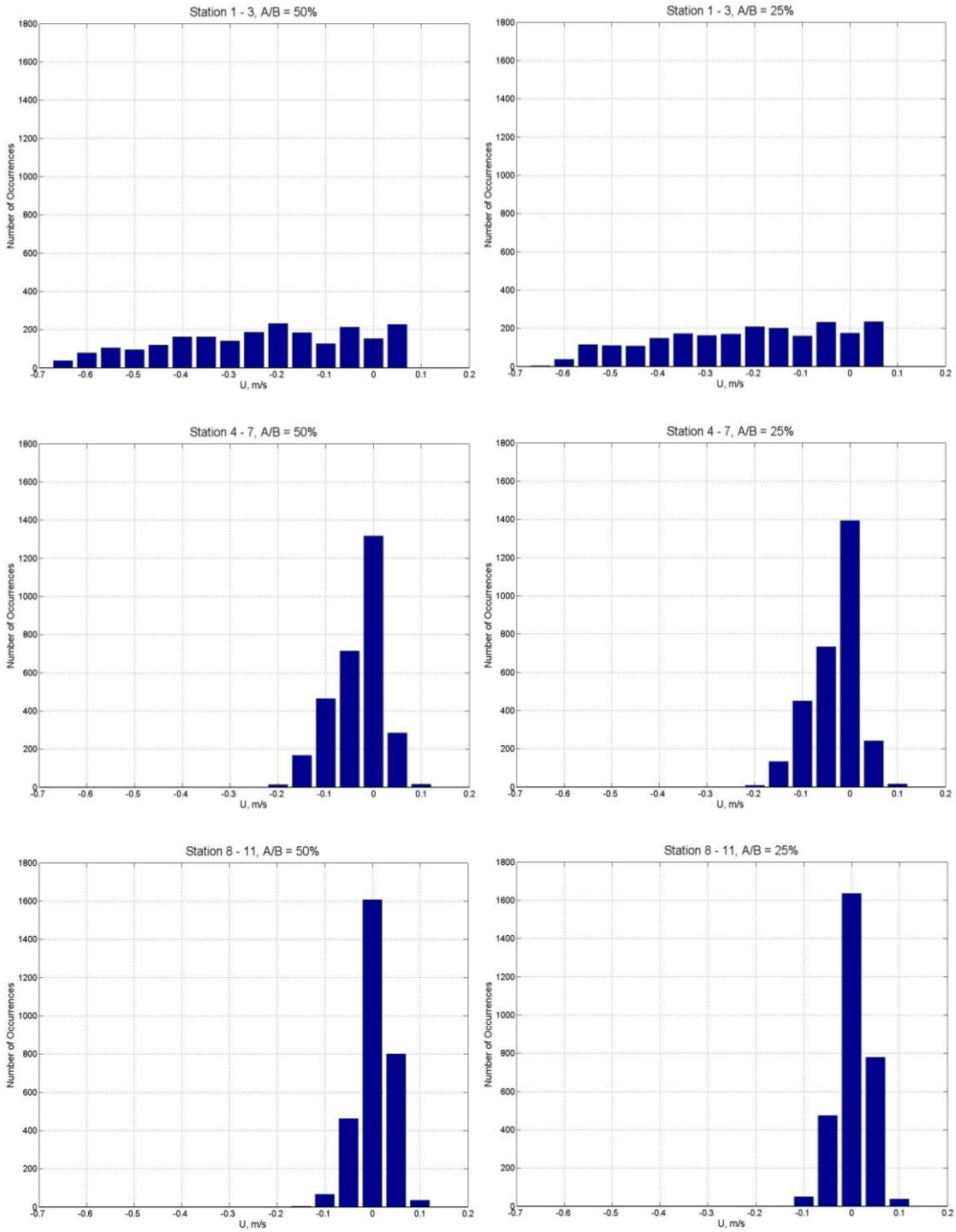

Figure 3.10 Number of occurrences compared with cross-shore current for Station 1-3, Station 4-7 and Station 8-11 respectively. Left: A/B=50%; Right: A/B=25%.

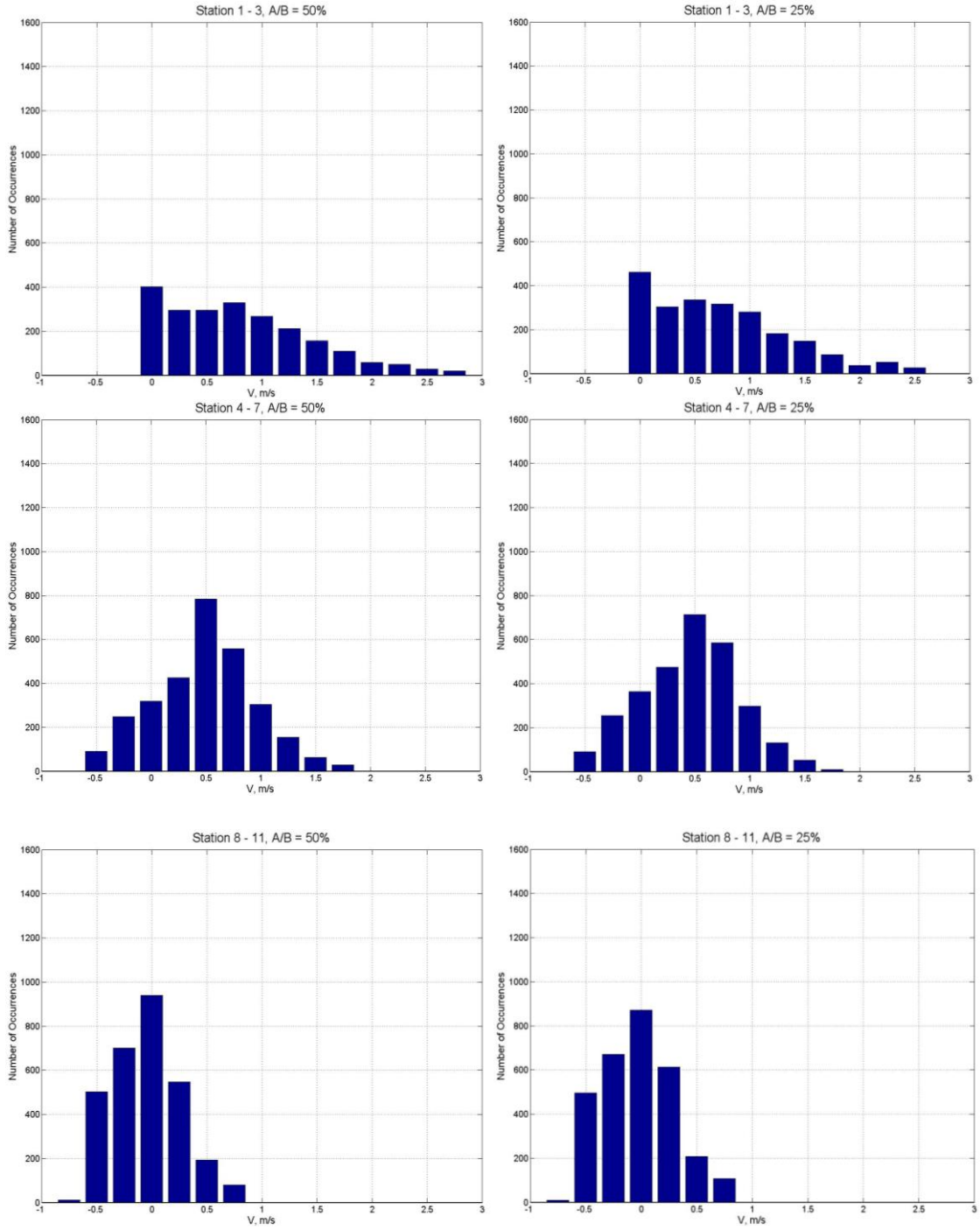

Figure 3.11 Number of occurrences compared with longshore current for Station 1-3, Station 4-7 and Station 8-11 respectively. Left: A/B=50%; Right: A/B=25%.

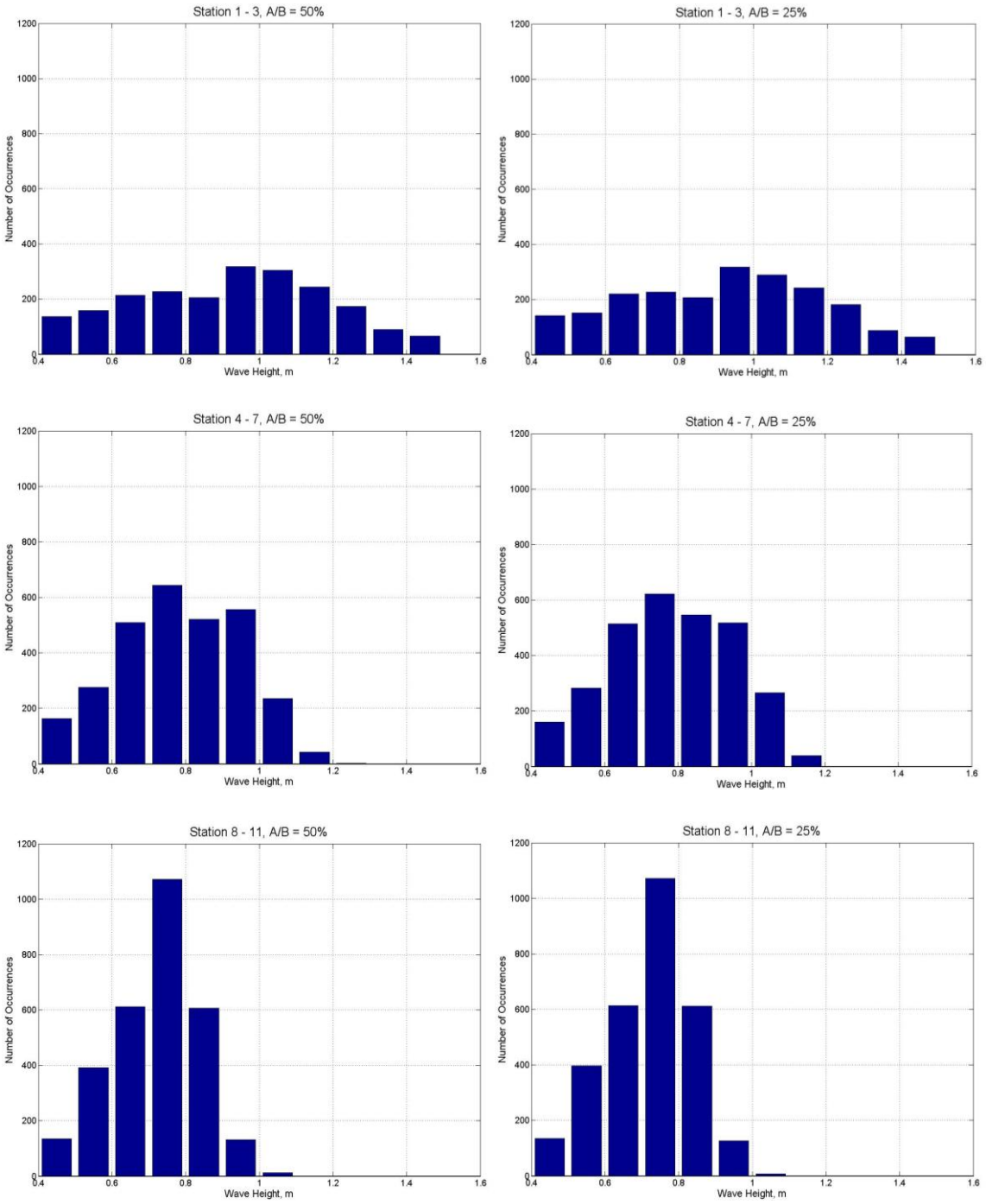

Figure 3.12 Number of occurrences compared with wave height for Station 1-3, Station 4-7 and Station 8-11 respectively. Left: A/B=50%; Right: A/B=25%.

3.4 EOF Results

As mentioned above, we conduct model runs with hourly initial wave spectrum for EOF analysis. Figure 3.13 and Figure 3.14 depict the spatial and temporal behavior for EOF modes 1-2 based on the NCEX case with the extension ratio A/B equal to 50% (standard) and 25% respectively. Figure 3.15-3.16 show the EOF modes 7-8 with ratio A/B equal to 50% and 25%. Appendix B describe the comparisons of EOF modes 3-6.

First of all, we can see much more variation between our standard and 25% cases in higher EOF modes (modes 7-8) than lower ones (modes 1-2); the higher modes of motion are affected more by error. Secondly, both eddylike structures and slablike structures are shown in EOF modes 1-8 of both 50% and 25% cases, but higher modes have more eddylike structures than lower ones. For instance, we obtain a large-dominant eddylike structure in the center of each lower mode, especially in mode 1 and mode 2. This is not evident in higher modes such as mode 7 and mode 8. In general, all modes of the standard case are altered by grid extension reduction; the degree of alteration, however, is far greater for the higher modes (modes 7 and 8) than for the lower modes (modes 1 and 2).

Figure 3.17 shows the percentage variance in EOF modes and the normalized amplitude of the first 8 modes. Addtionally, the first 8 modes represent 85.75% of the total variance in standard case (A/B=50%) and 85.82% of the total variance in 25% cases.

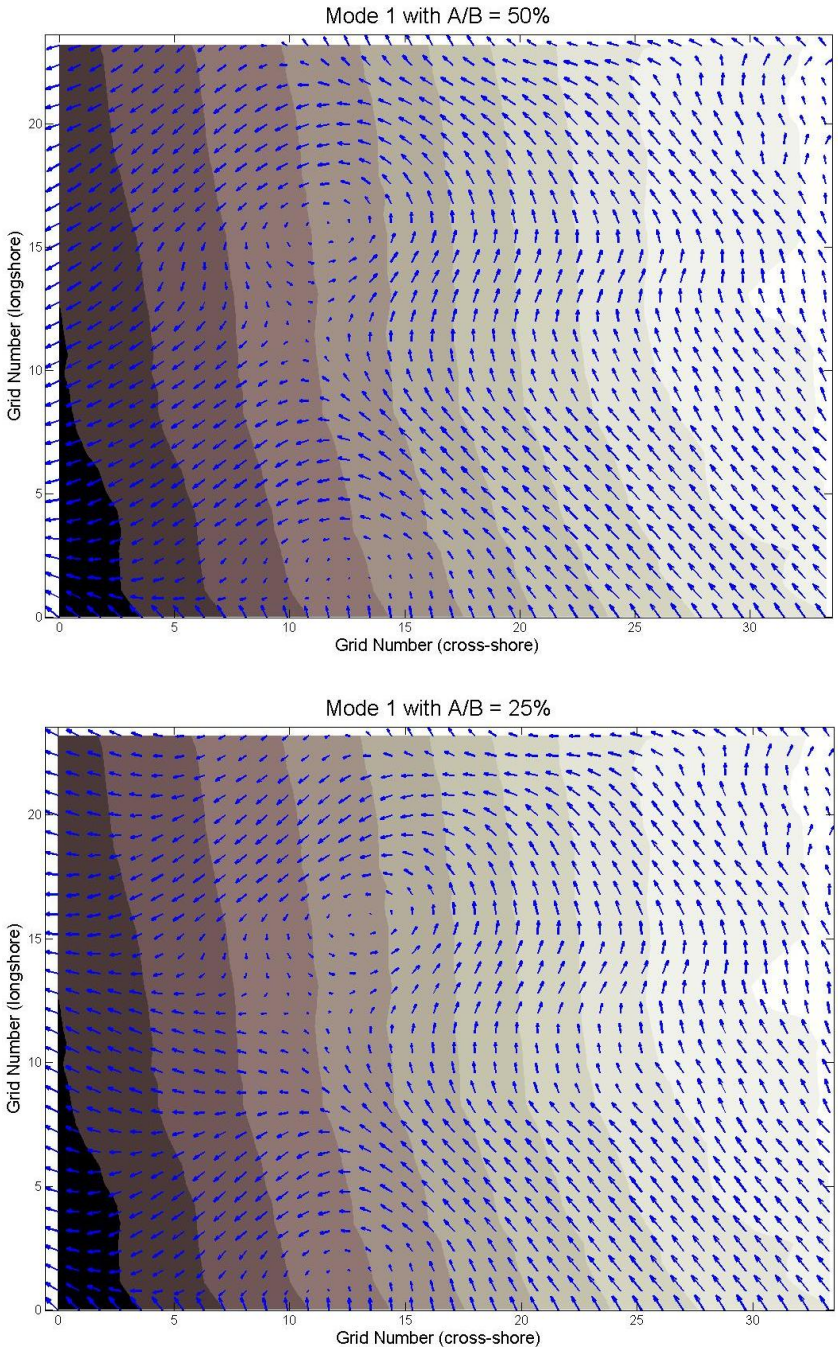

Figure 3.13 EOF mode 1 based on the NCEX case with A/B=50% (top) and A/B=25% (bottom).

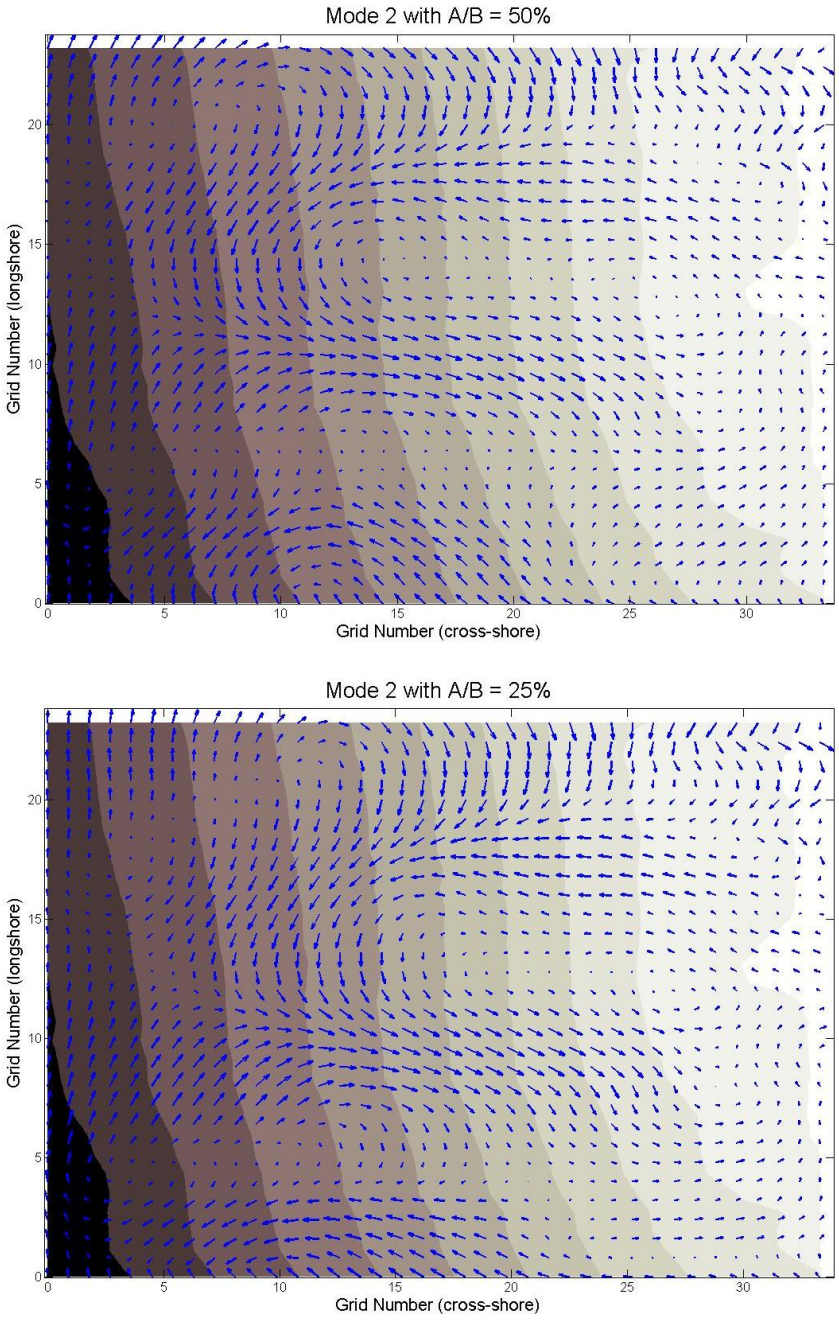

Figure 3.14 EOF mode 2 based on the NCEX case with A/B=50% (top) and A/B=25% (bottom).

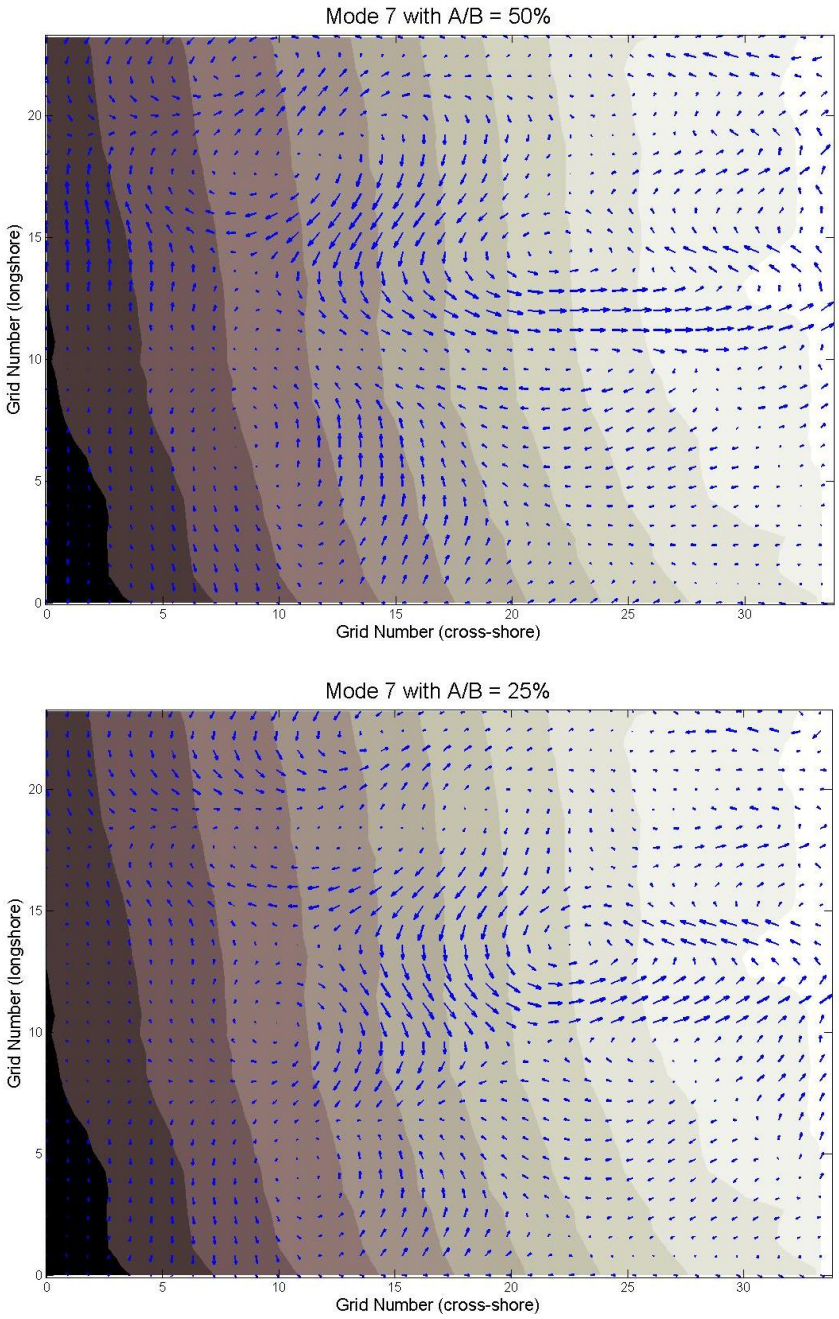

Figure 3.15 EOF mode 7 based on the NCEX case with A/B=50% (top) and A/B=25% (bottom).

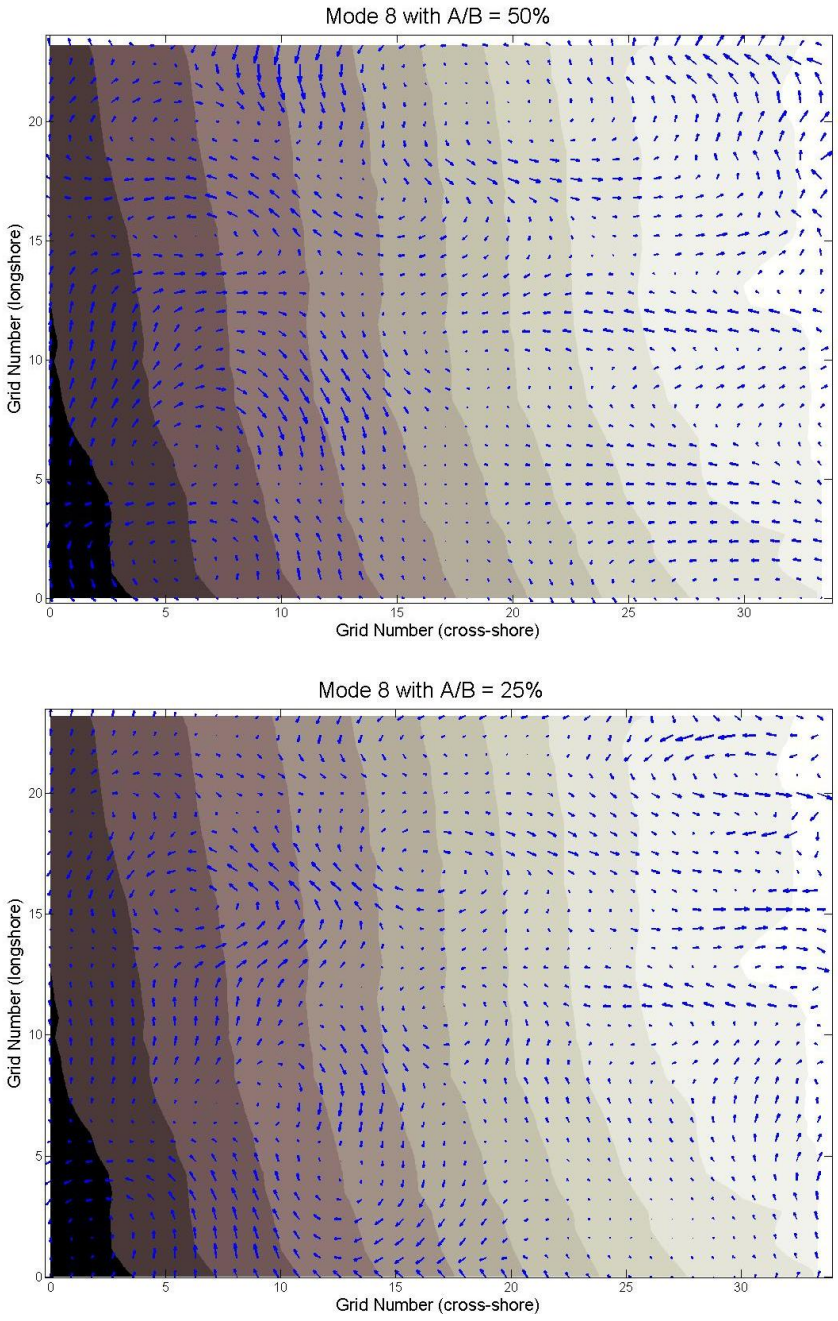

Figure 3.16 EOF mode 8 based on the NCEX case with A/B=50% (top) and A/B=25% (bottom).

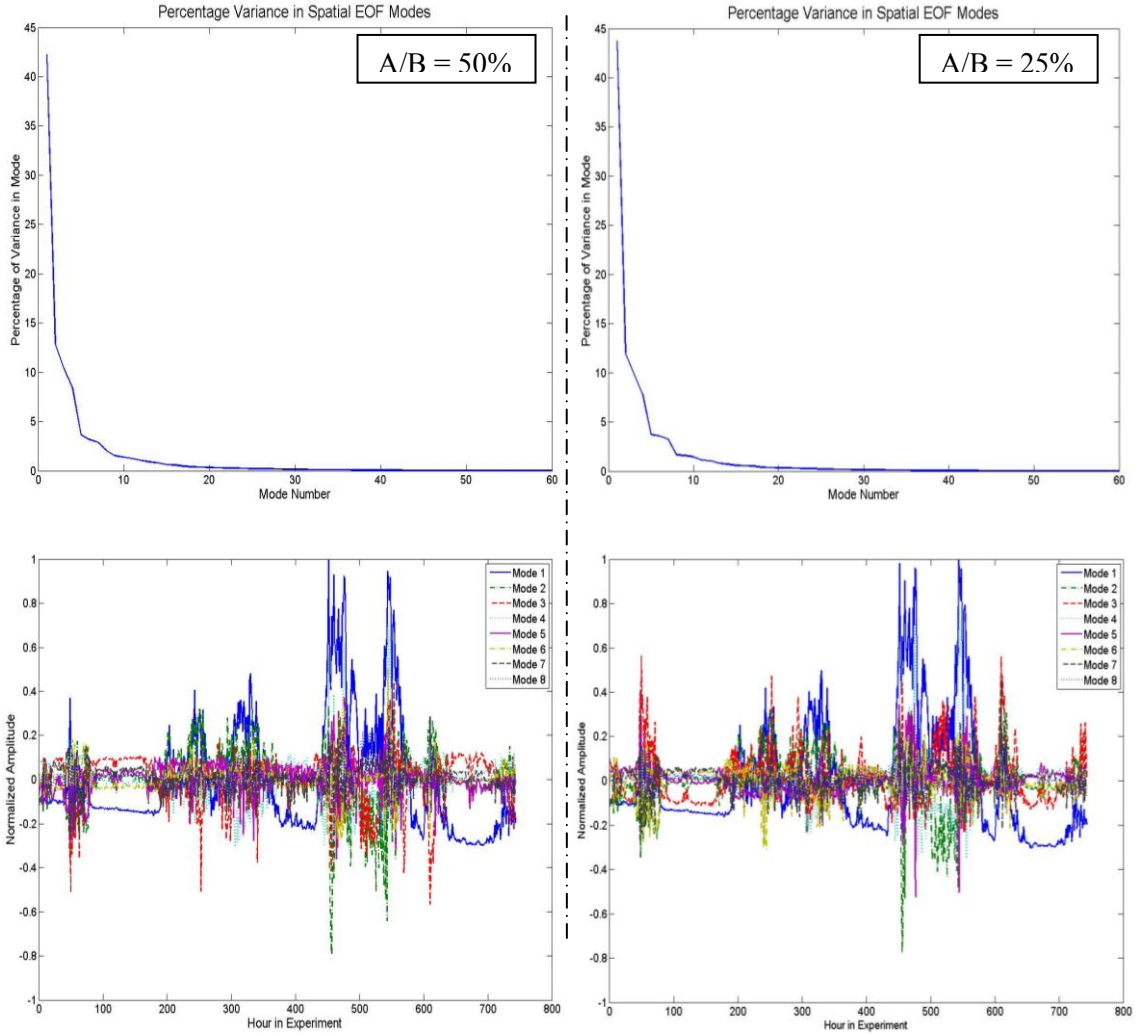

Figure 3.17 EOF Percentage variance in EOF modes and the normalized amplitude of the first 8 modes. Left: A/B=50%. Right: A/B=25%.

3.5 Swirl Strength Method

We note that it is important to know the characteristics of eddy structures and their distribution in the model output. Many methods can be applied to identify vortical structures in two-dimensional data. Herein we choose the local swirl strength criterion, which was shown (Adrian *et al*. 2000) to be most effective at identifying the full range

of vortices. The local swirl strength can be calculated by building an equivalent two-dimensional velocity gradient tensor *D* given by:

$$D = \begin{bmatrix} \frac{\partial u}{\partial x} & \frac{\partial u}{\partial y} \\ \frac{\partial v}{\partial x} & \frac{\partial v}{\partial y} \end{bmatrix} \tag{32}$$

where *u* and *v* are respectively the instantaneous velocity vectors in the cross-shore *x* and longshore *y* coordinate directions. The velocity gradients are calculated from EOF data using a two-point central difference method (Raffel *et al.*, 1998). The local swirl strength, represents the local frequency of rotation, is the imaginary part of the complex conjugate eigenvalues of the tensor *D*. It is clear in the Figure 3.18 that the swirl strength identifies the vortexes which are clearly visible in the data.

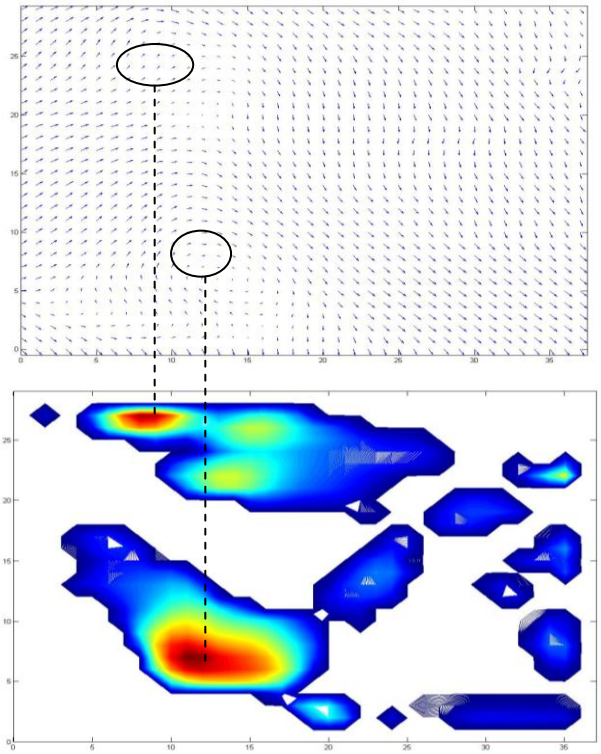

Figure 3.18 Velocity field from EOF data (top) and Swirl Strength estimate (bottom).

Figure 3.19-3.26 show the identified vortex map with contours of swirl strength for the velocity vector map depicted in Figure 3.13-3.16 and Appendix B.

To quantify the properties of individual “vortices”, a clipping procedure is required. The function bwlabel in MATLAB® toolbox is used to assign a number to each vortex in the flow field. Each identified vortex is then easily indexed, its position identified, and used to clip the velocity and vorticity maps, resulting in fields for the identified vortex only (Bryant *et al.* 2009). Additionally, the position of maximum swirl strength of each individual vortex is recorded and marked with dot in the bottom panels in Figure 3.19-3.26 in order to present the position of each structure. The effect of the errors on the location and shape of the swirl strength contours increase from lower modes to higher modes. For example, the differece between 50% and 25% case of mode 8 is much bigger than that of mode 1.

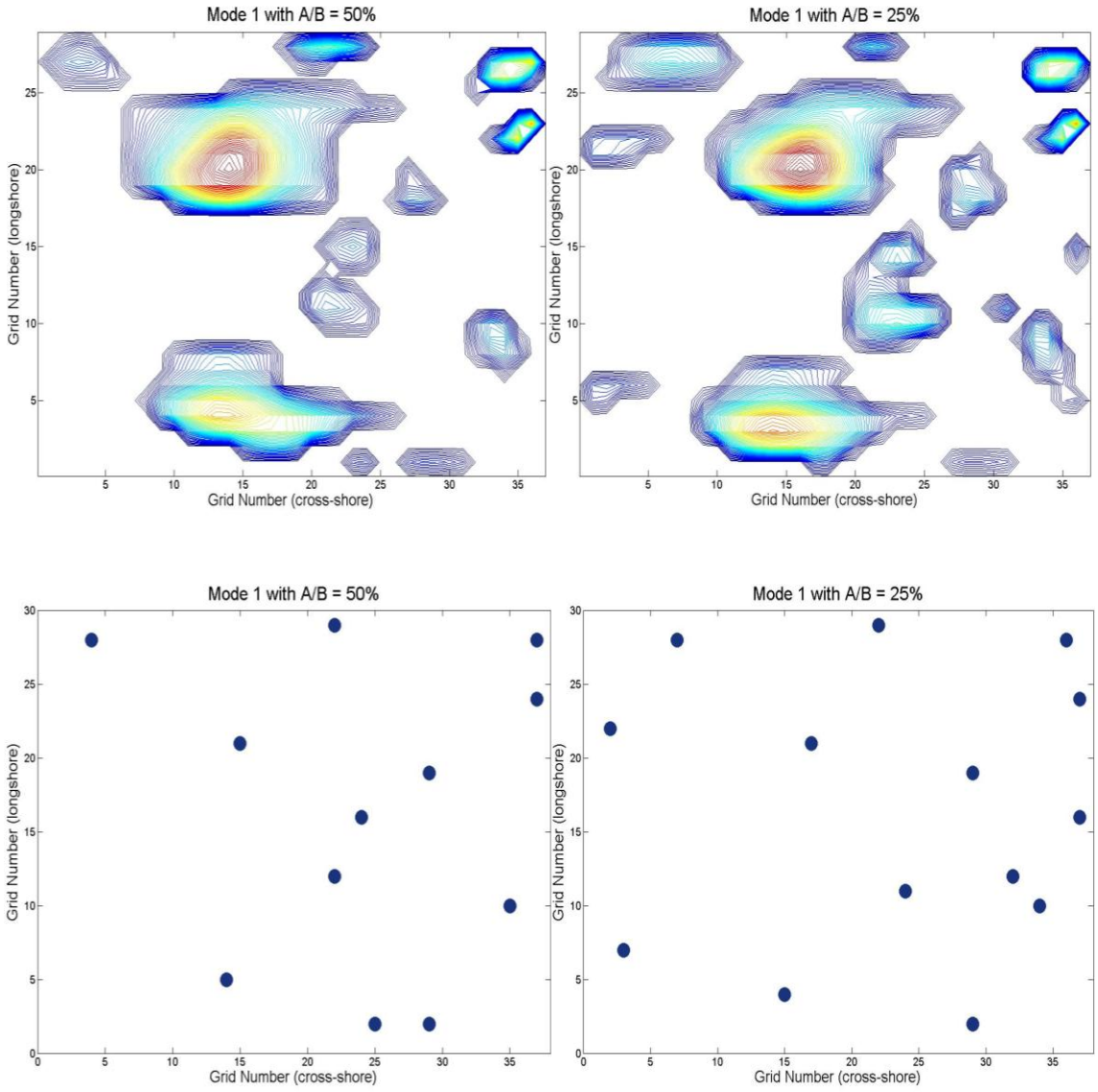

Figure 3.19 Swirl Strength estimate (top) and identification marks for eddy structures (bottom) of EOF mode 1. Left: A/B=50%. Right: A/B=25%.

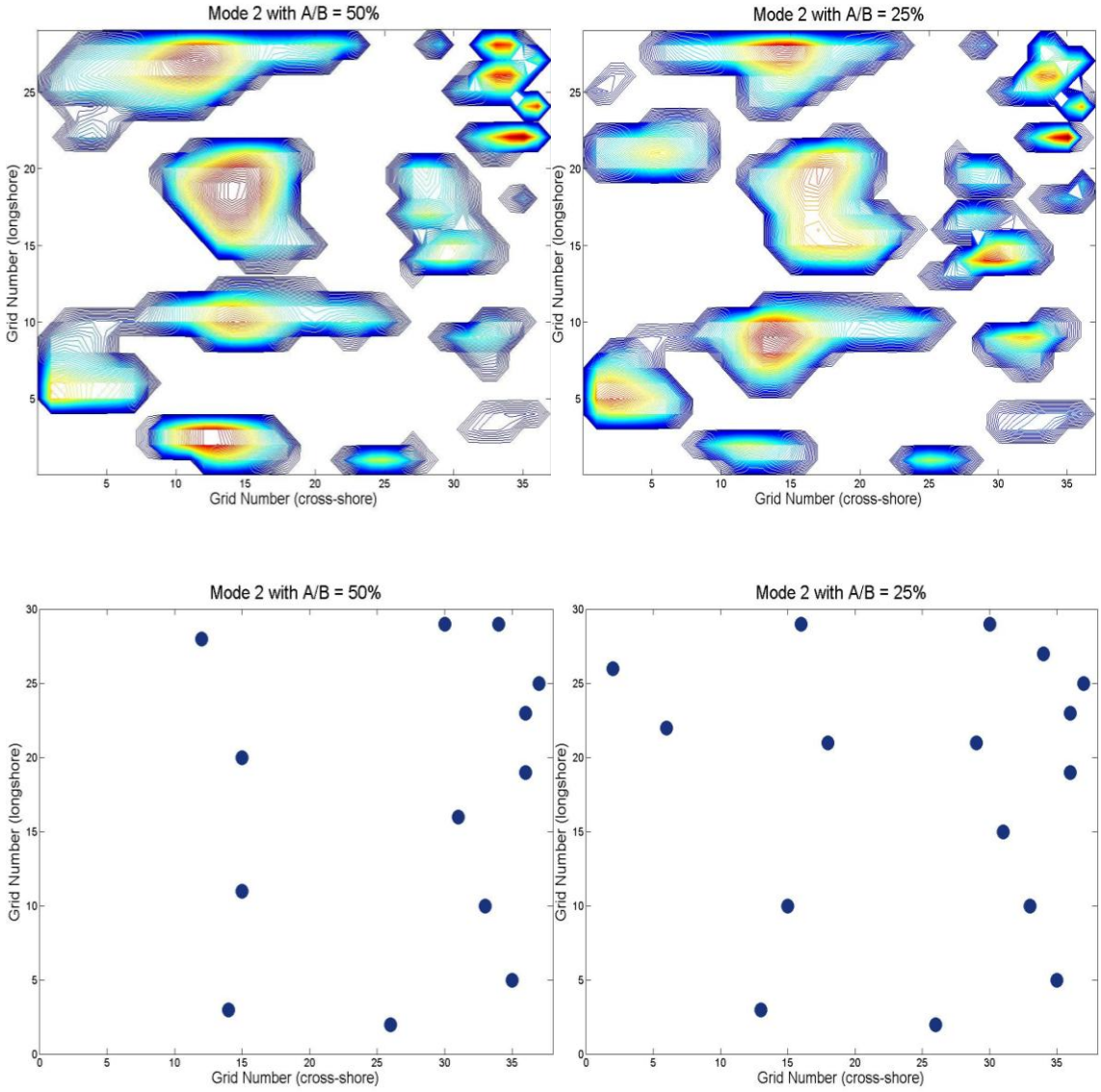

Figure 3.20 Swirl Strength estimate (top) and identification marks for eddy structures (bottom) of EOF mode 2. Left: A/B=50%. Right: A/B=25%.

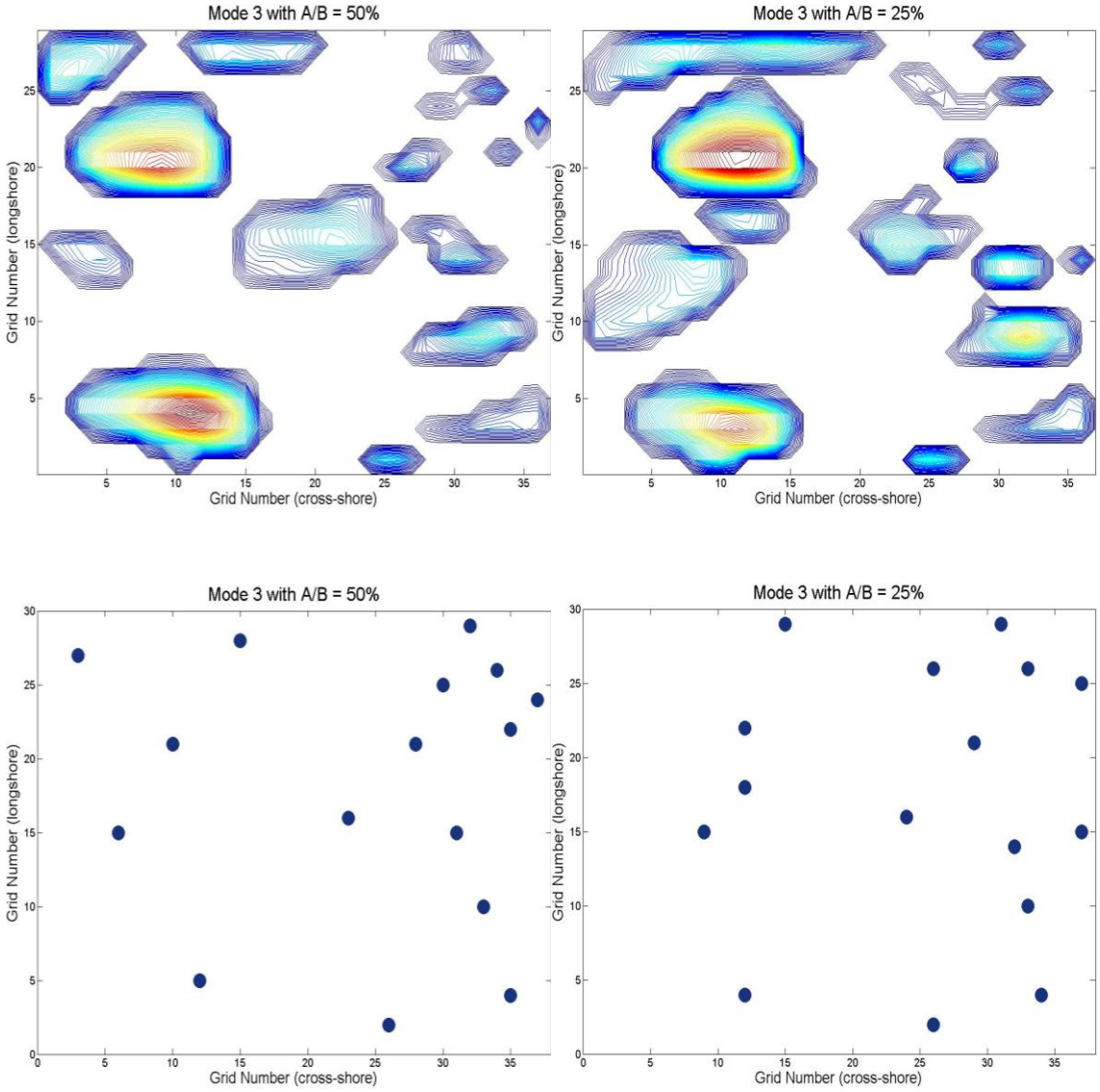

Figure 3.21 Swirl Strength estimate (top) and identification marks for eddy structures (bottom) of EOF mode 3. Left: A/B=50%. Right: A/B=25%.

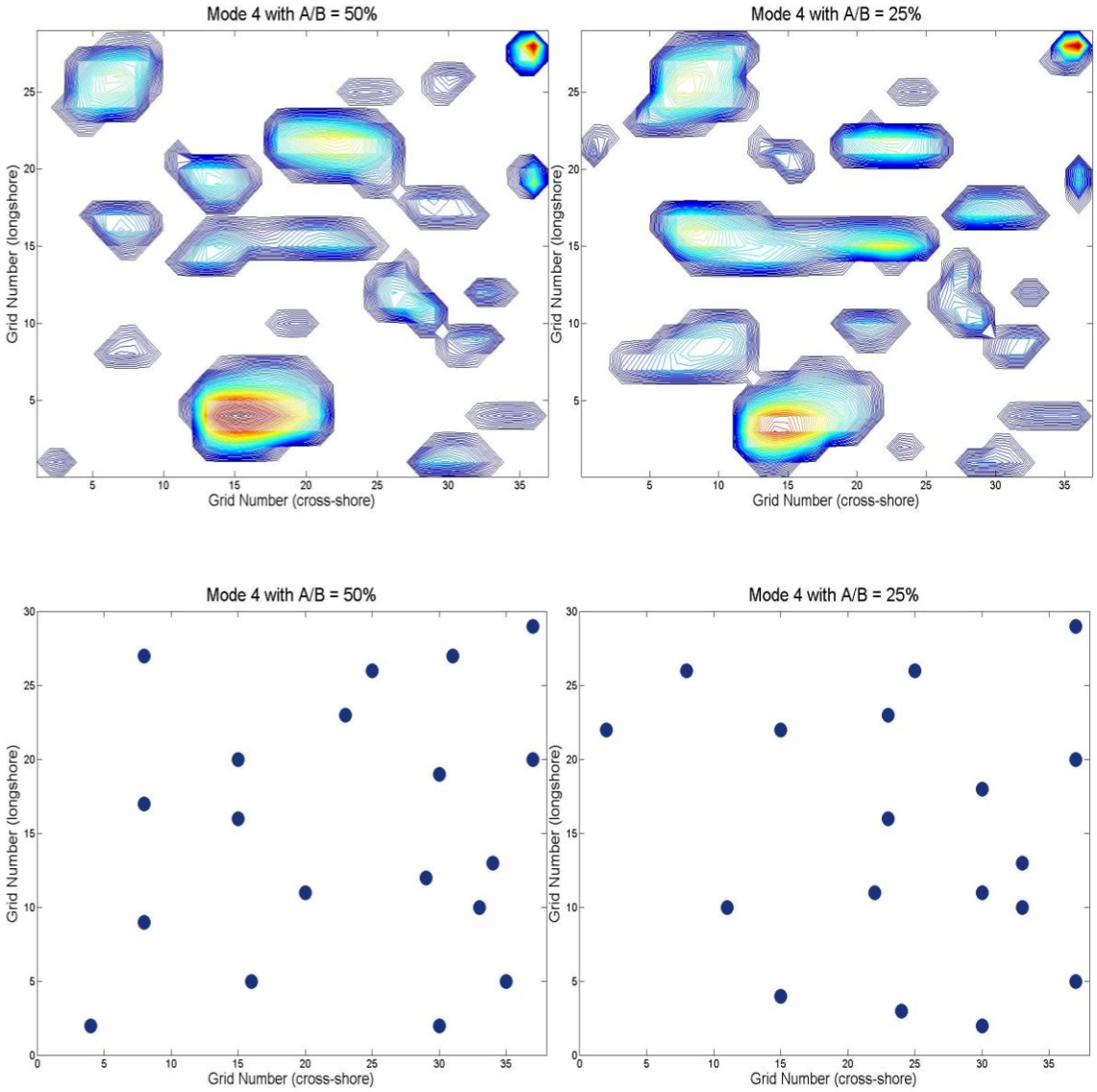

Figure 3.22 Swirl Strength estimate (top) and identification marks for eddy structures (bottom) of EOF mode 4. Left: A/B=50%. Right: A/B=25%.

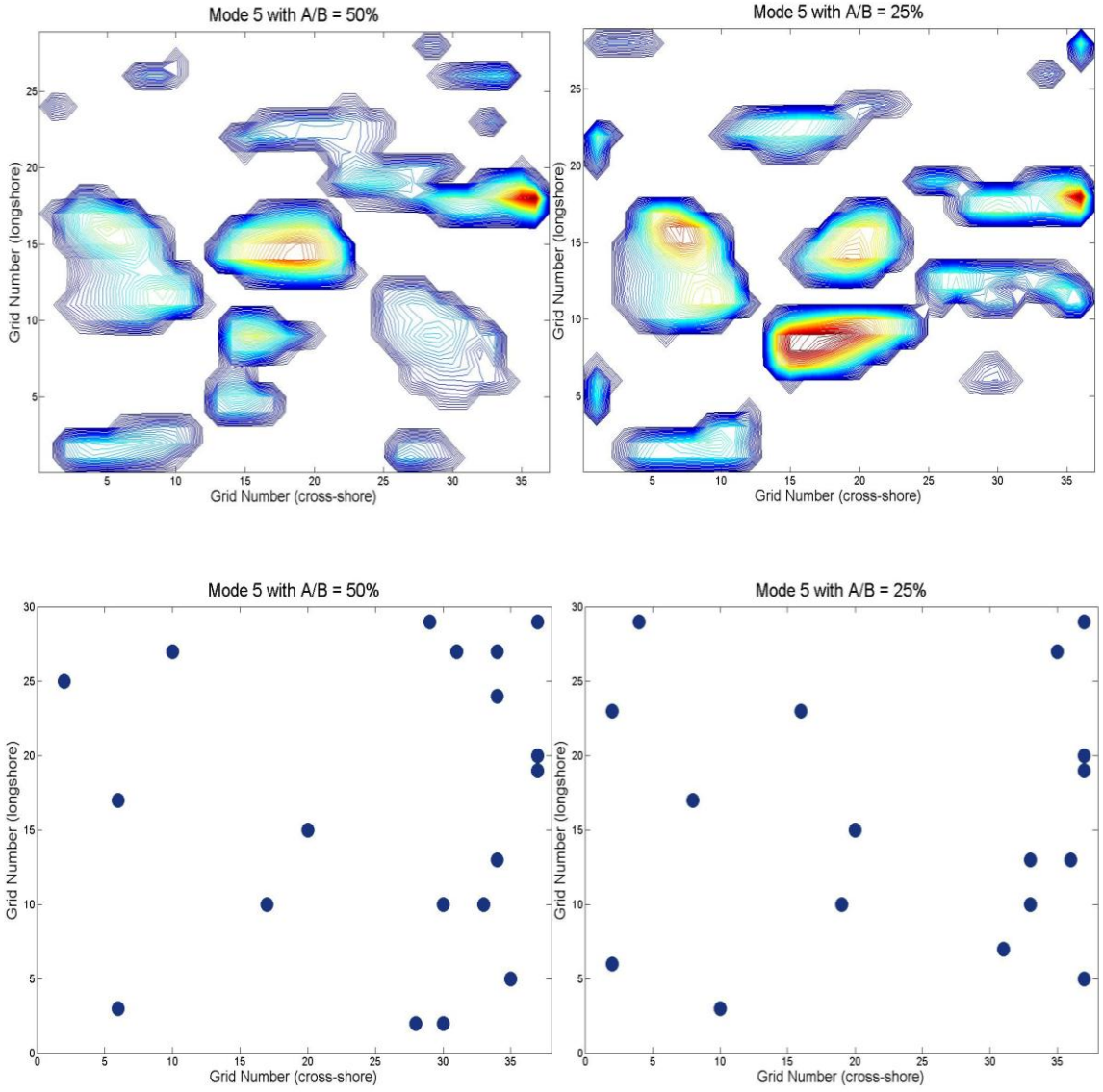

Figure 3.23 Swirl Strength estimate (top) and identification marks for eddy structures (bottom) of EOF mode 5. Left: A/B=50%. Right: A/B=25%.

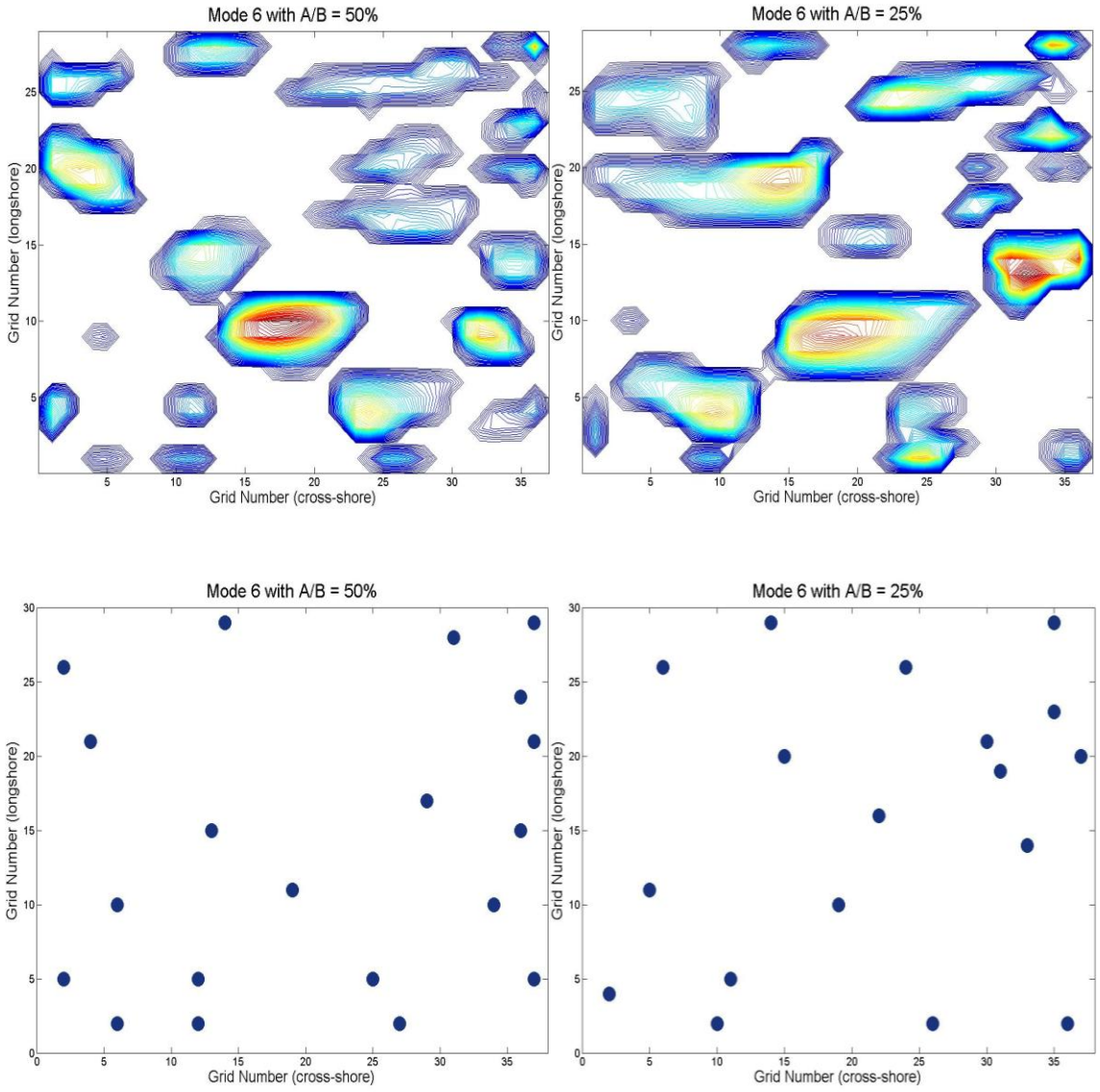

Figure 3.24 Swirl Strength estimate (top) and identification marks for eddy structures (bottom) of EOF mode 6. Left: A/B=50%. Right: A/B=25%.

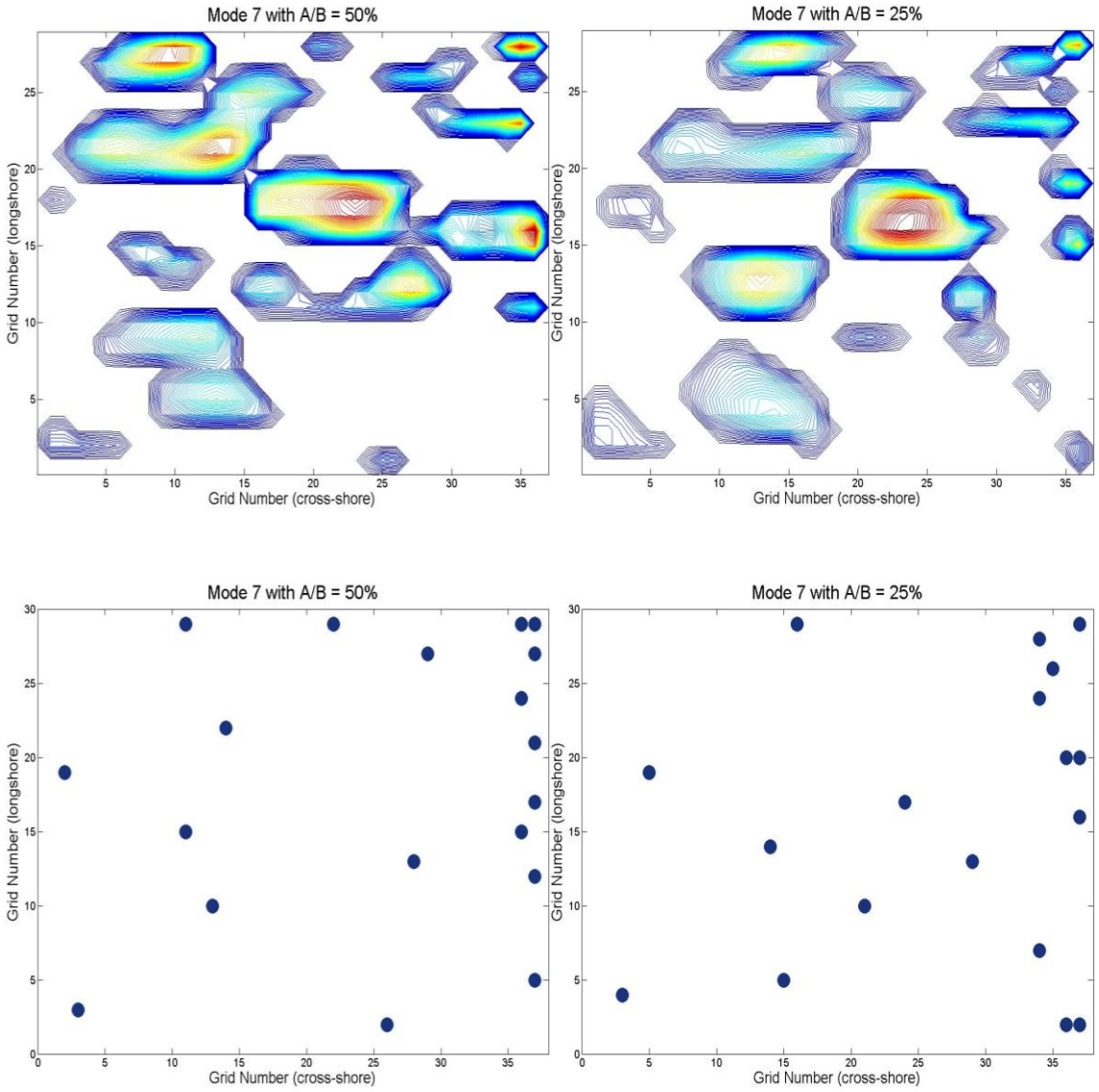

Figure 3.25 Swirl Strength estimate (top) and identification marks for eddy structures (bottom) of EOF mode 7. Left: A/B=50%. Right: A/B=25%.

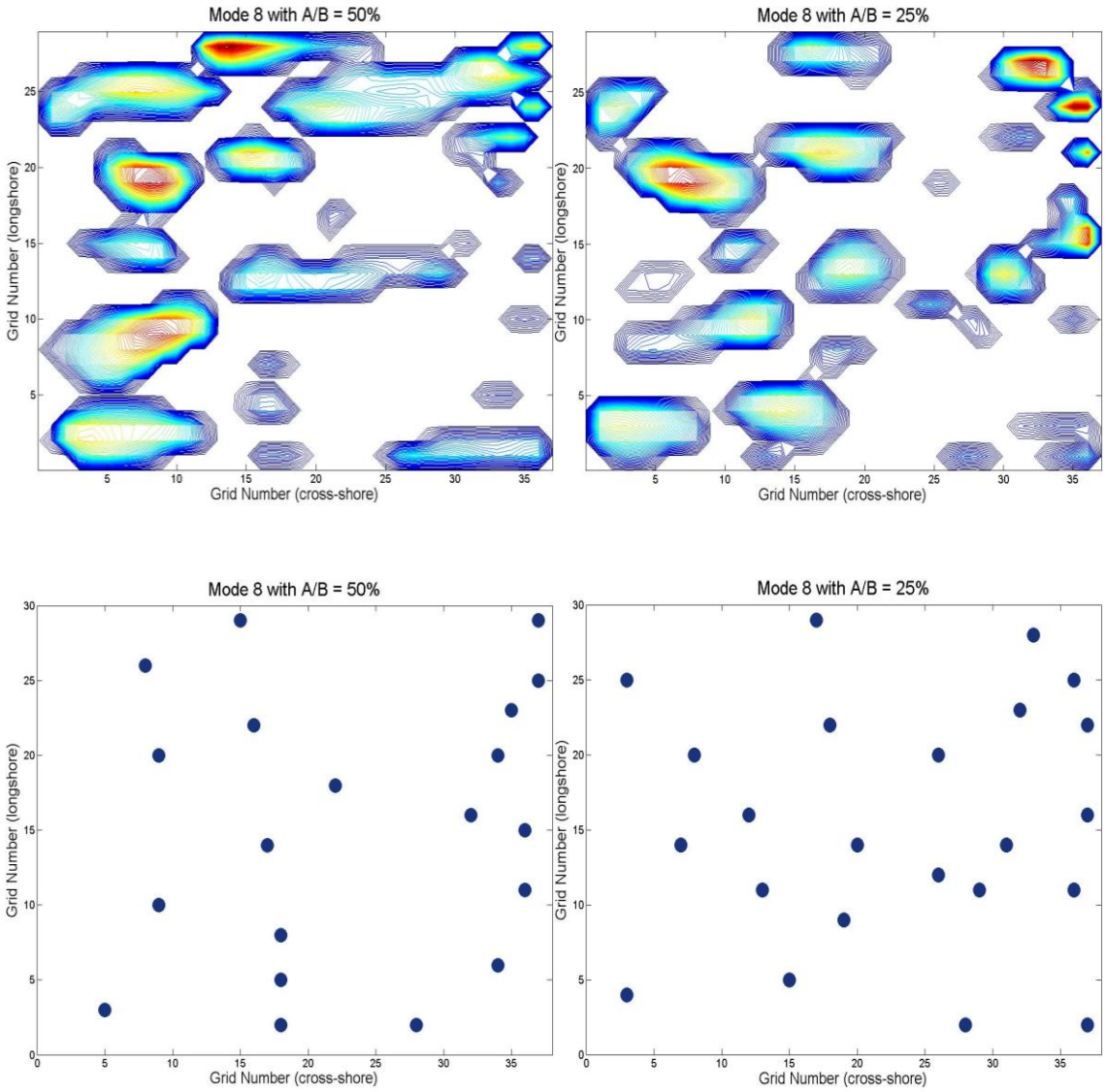

Figure 3.26 Swirl Strength estimate (top) and identification marks for eddy structures (bottom) of EOF mode 8. Left: A/B=50%. Right: A/B=25%.

3.6 Scale Analysis

In this part of study, we investigate how the spatial scales vary from EOF mode 1 to mode 8. This will allow us to identify possible representative scales in the modes and how these scales are affected by boundary errors. Longshore transects in three different locations (nearshore, middle and offshore), marked with boxes in the top panels of Figure 3.27-3.38, are selected to be the objectives of Fast Fourier Transform (FFT) algorithm. It is clear in the bottom panels that the scale of higher modes is smaller than that of lower modes. Figure 3.27-3.38 depict that the length scale of mode1 is about 300 *m* compared with 500 *m* of mode 8 for both 50% and 25% cases. While not definitive, this analysis does offer some insight into the spatial scales captured by each mode and how they are affected by the errors.

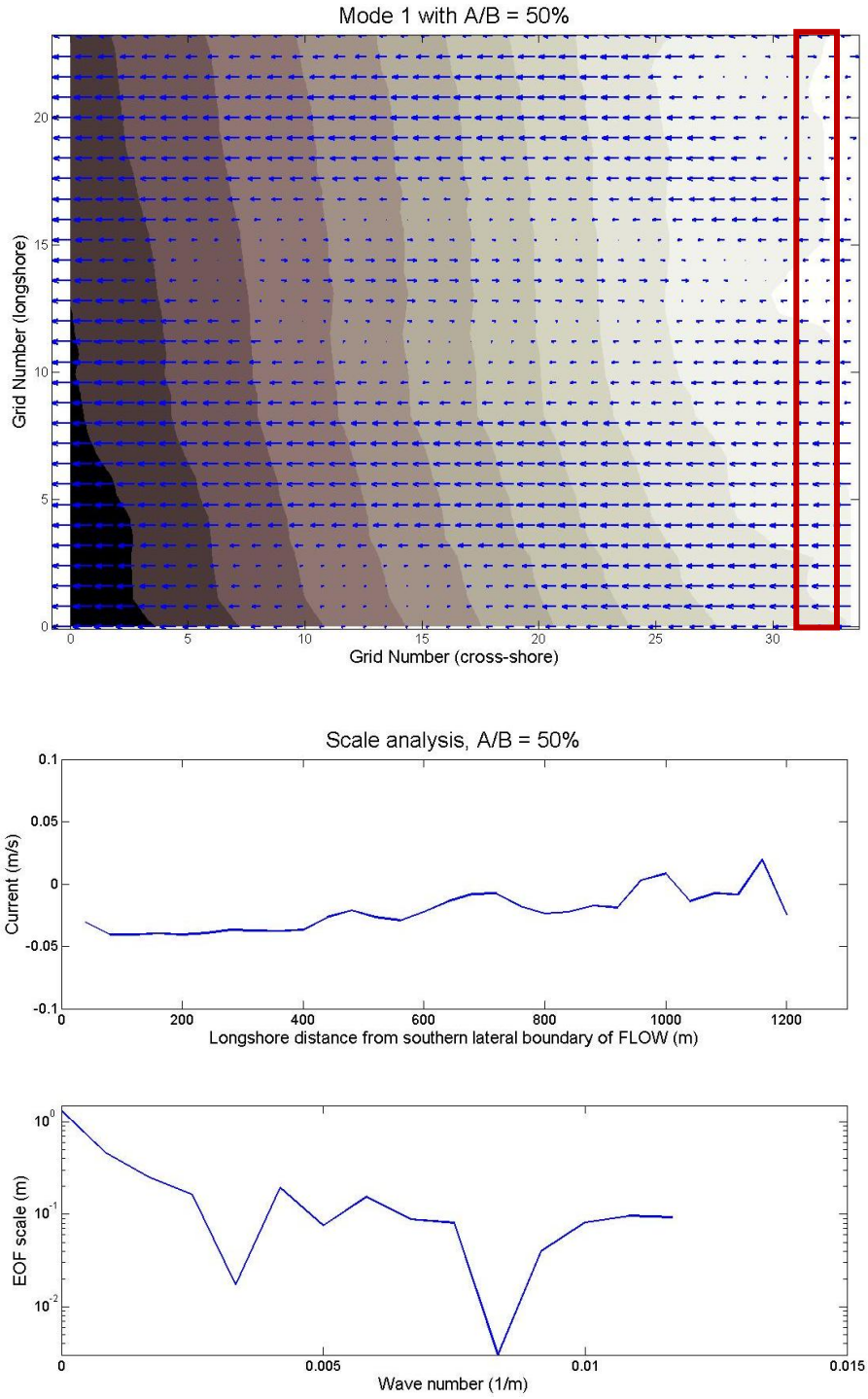

Figure 3.27 Cross-shore component of EOF mode 1 with 50% grid extension ratio (top), and scale analysis for the first series marked with box (bottom).

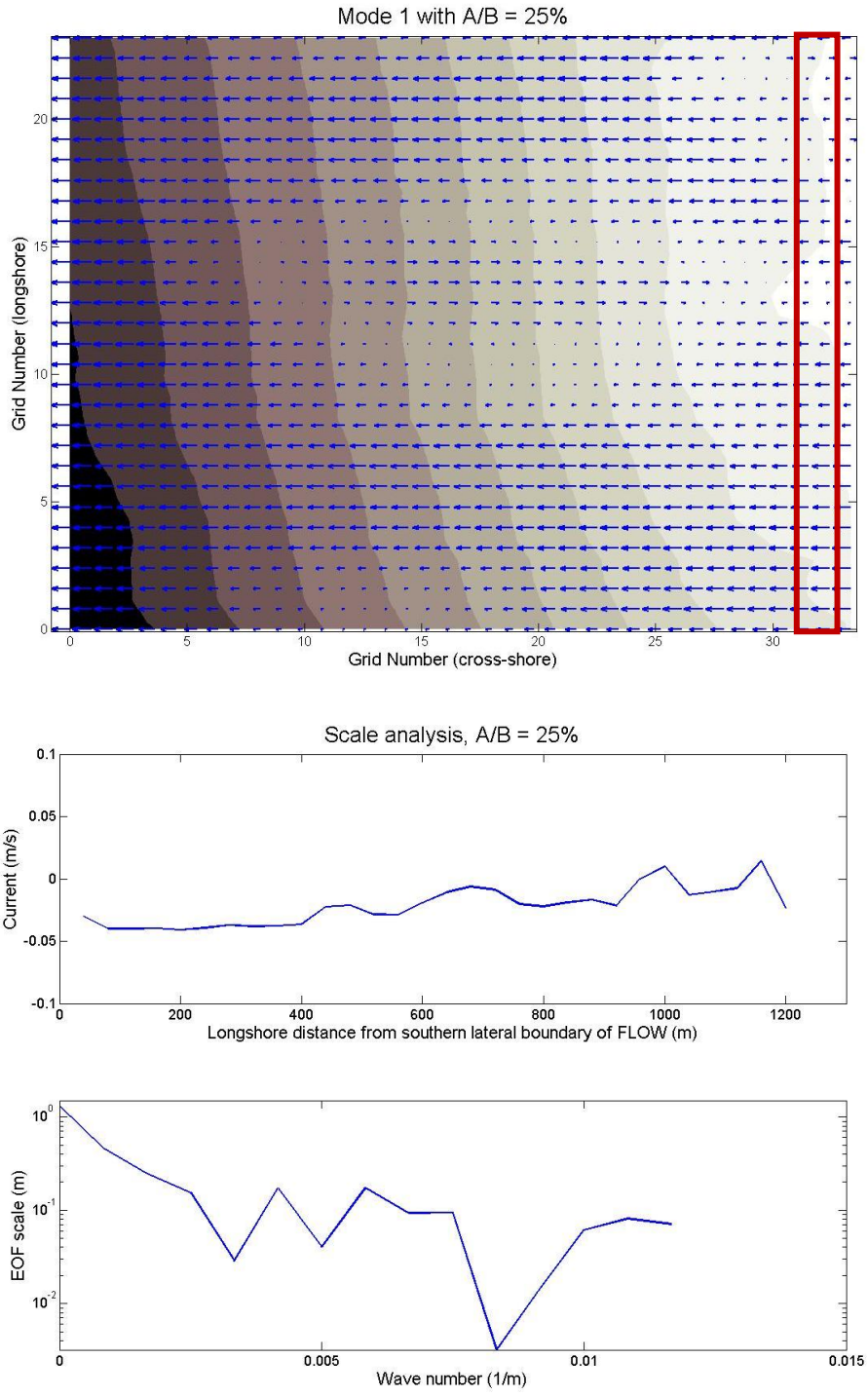

Figure 3.28 Cross-shore component of EOF mode 1 with 25% grid extension ratio (top), and scale analysis for the first series marked with box (bottom).

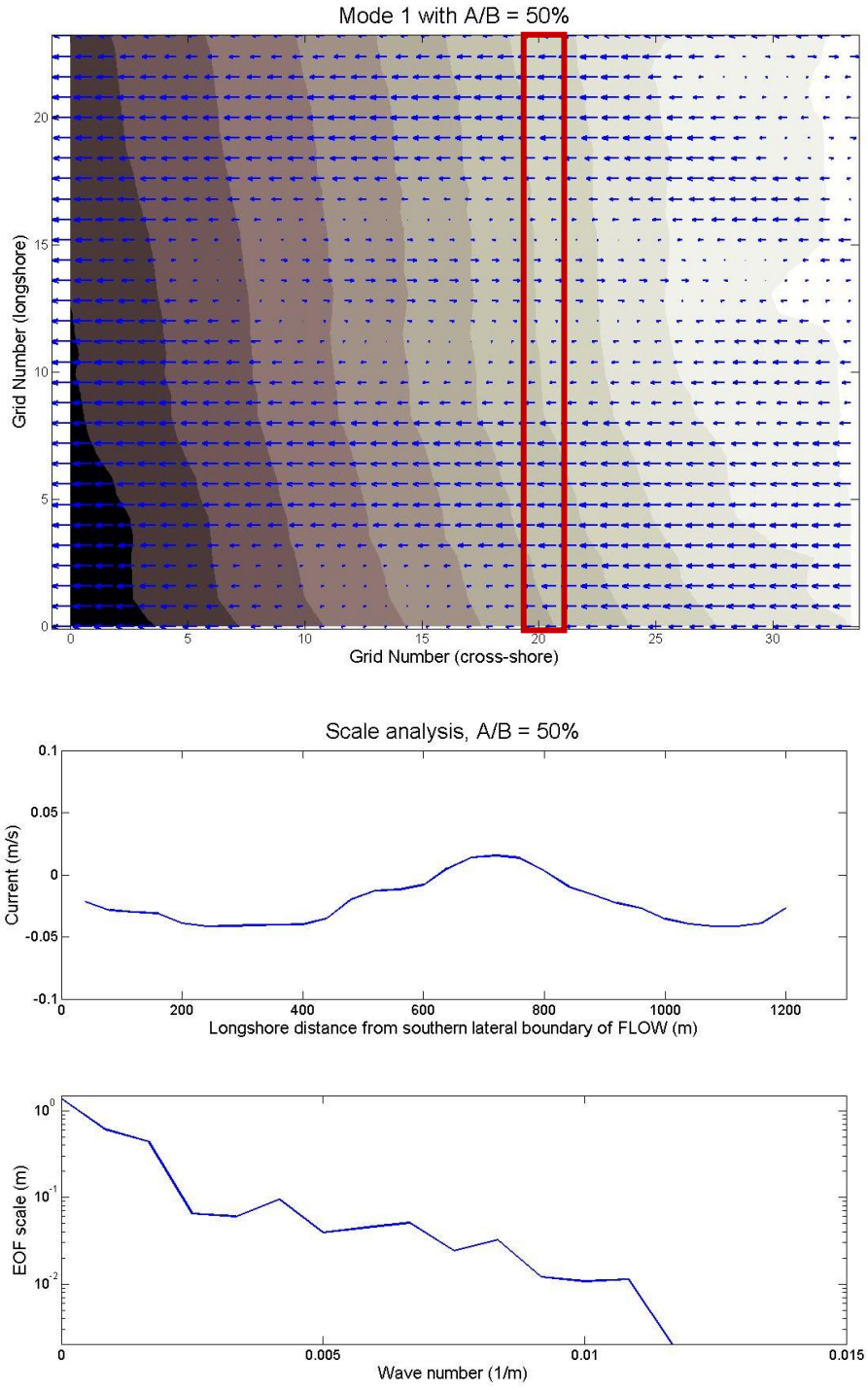

Figure 3.29 Cross-shore component of EOF mode 1 with 50% grid extension ratio (top), and scale analysis for the second series marked with box (bottom).

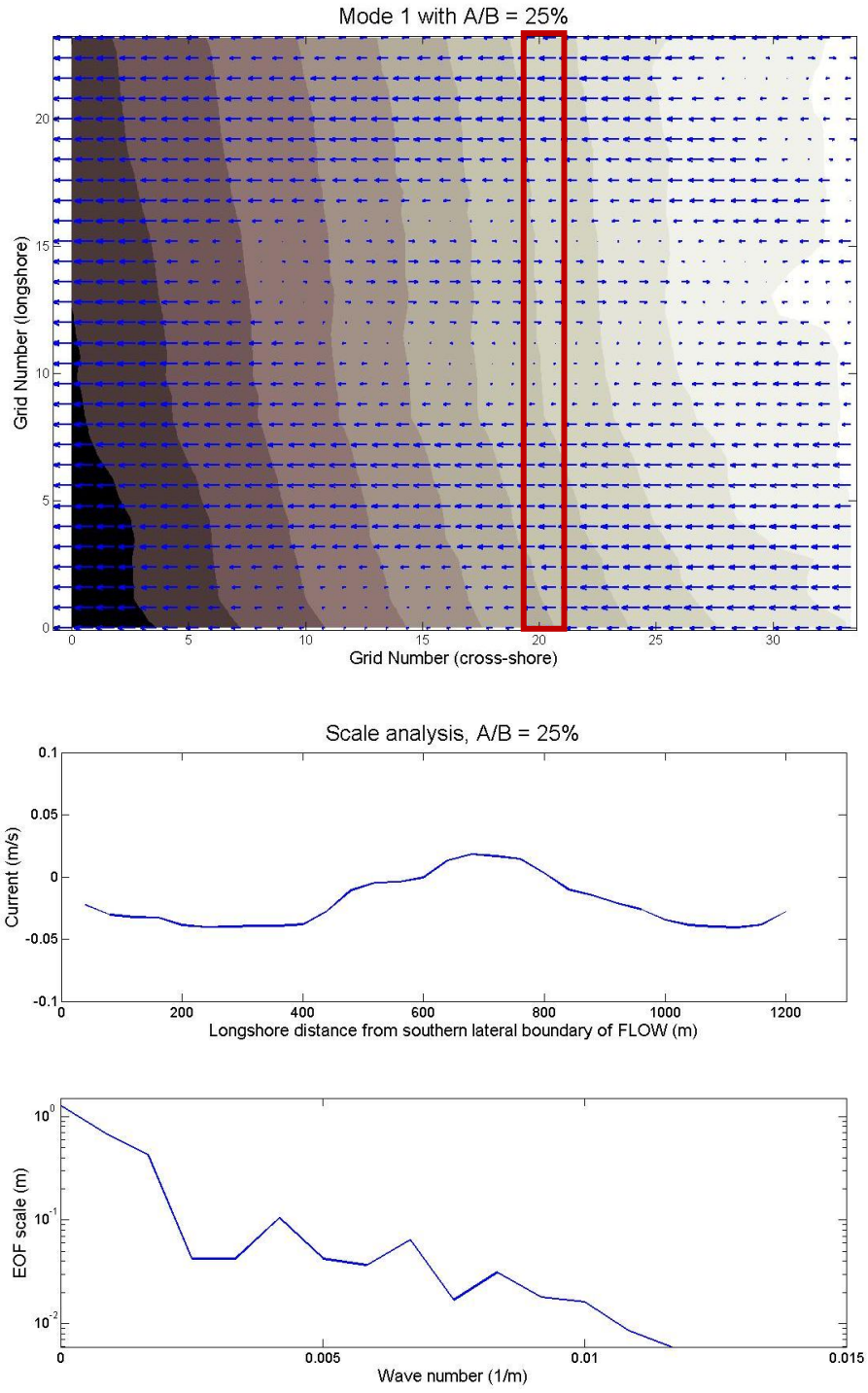

Figure 3.30 Cross-shore component of EOF mode 1 with 25% grid extension ratio (top), and scale analysis for the second series marked with box (bottom).

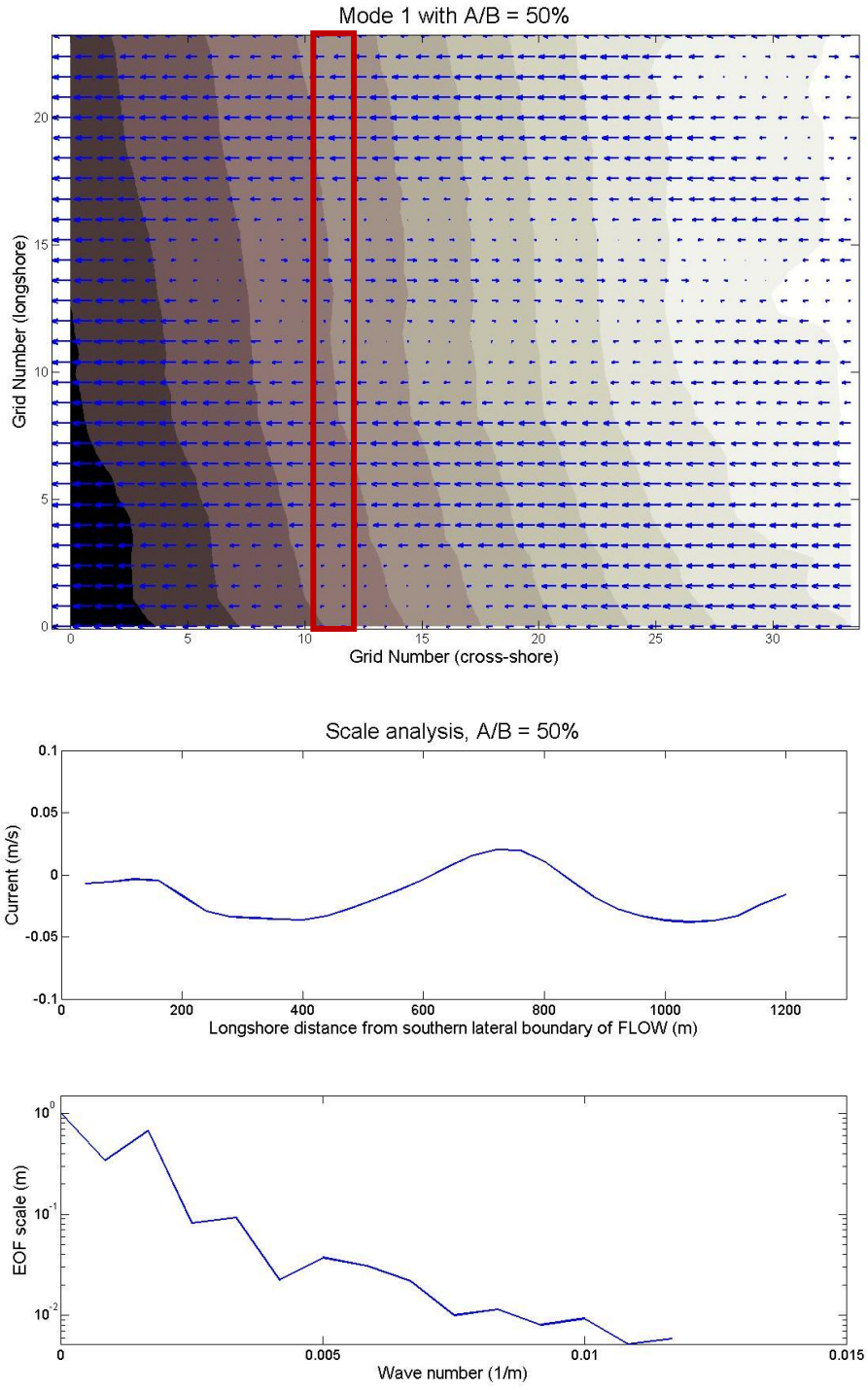

Figure 3.31 Cross-shore component of EOF mode 1 with 50% grid extension ratio (top), and scale analysis for the third series marked with box (bottom).

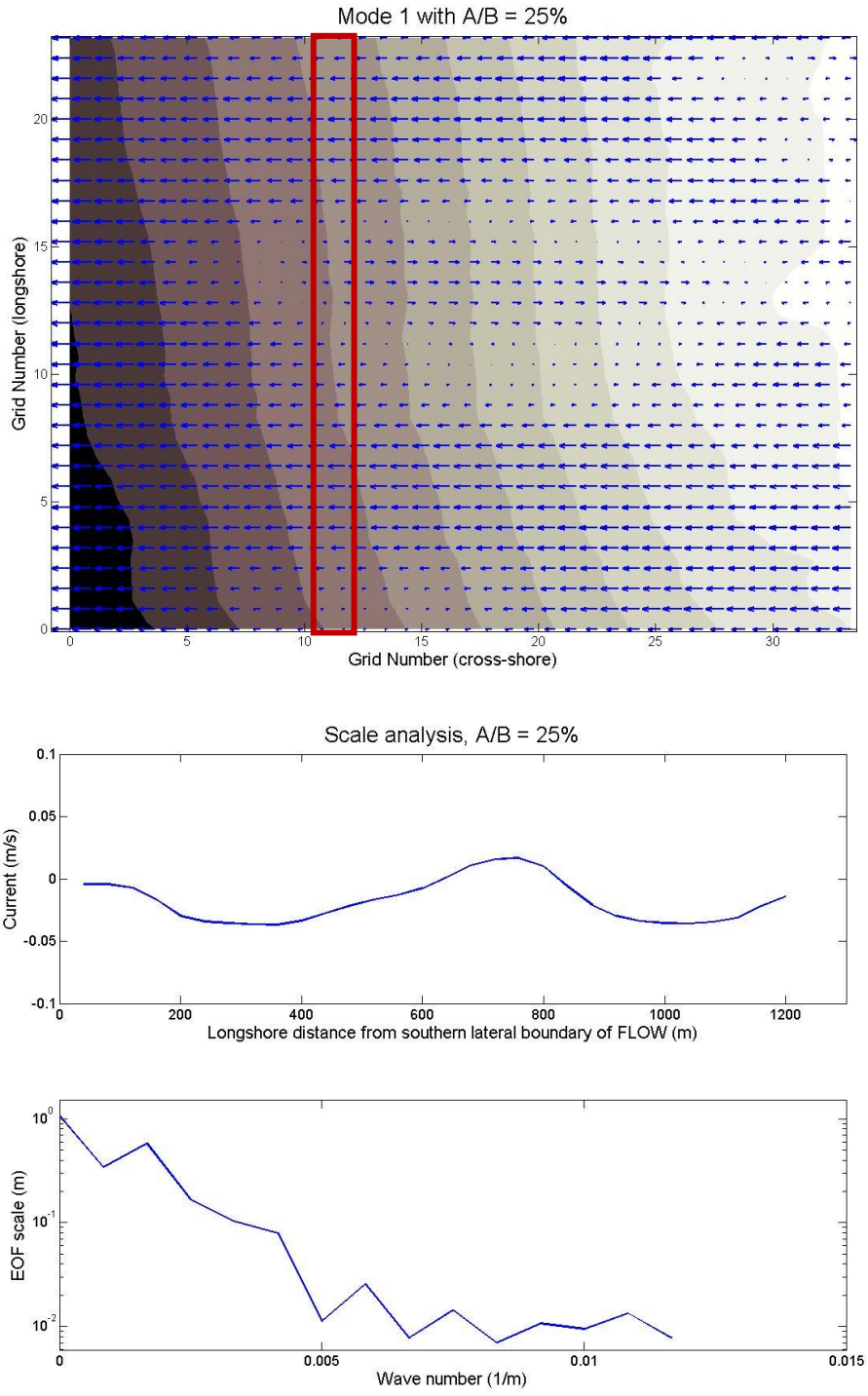

Figure 3.32 Cross-shore component of EOF mode 1 with 25% grid extension ratio (top), and scale analysis for the third series marked with box (bottom).

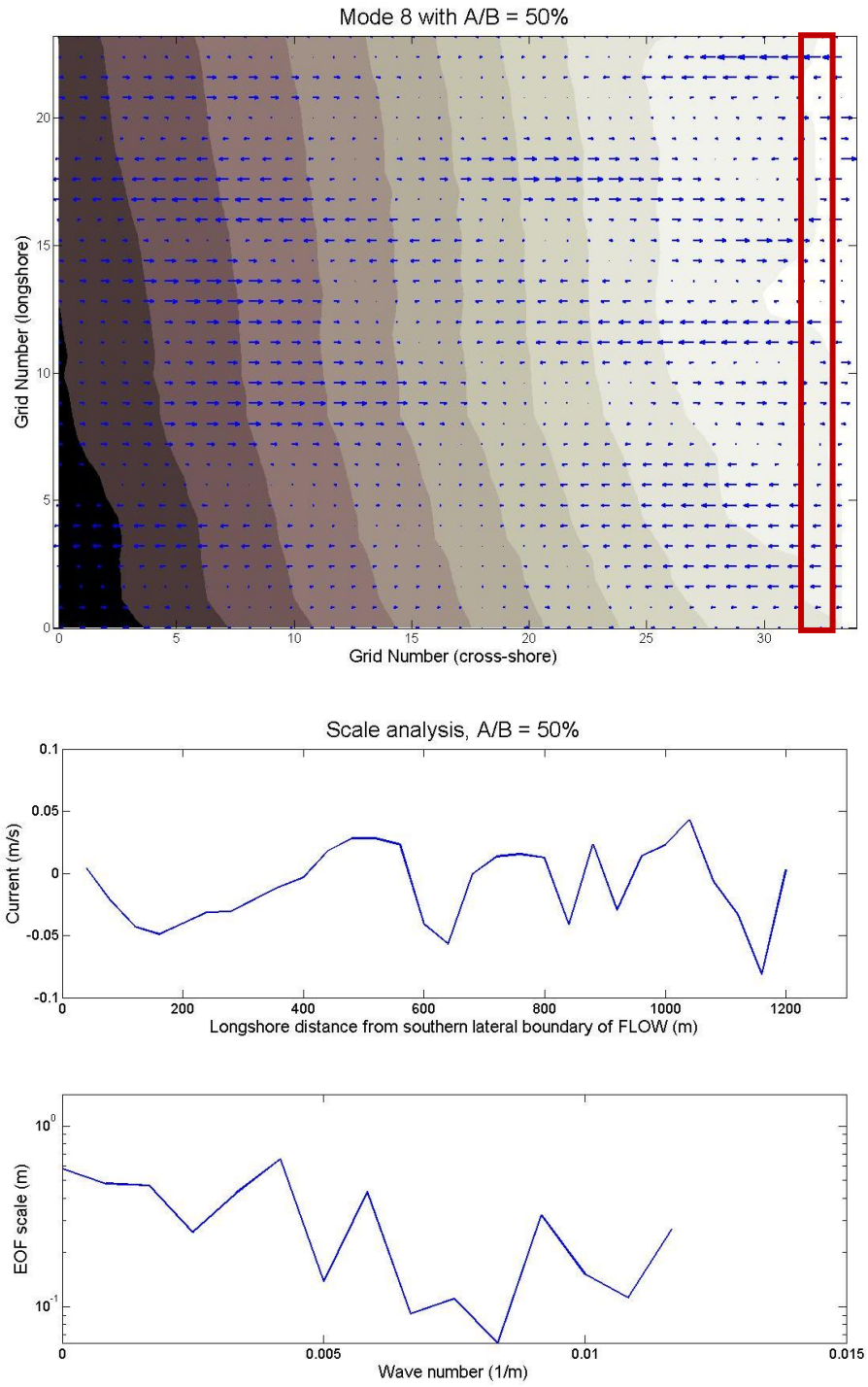

Figure 3.33 Cross-shore component of EOF mode 8 with 50% grid extension ratio (top), and scale analysis for the first series marked with box (bottom).

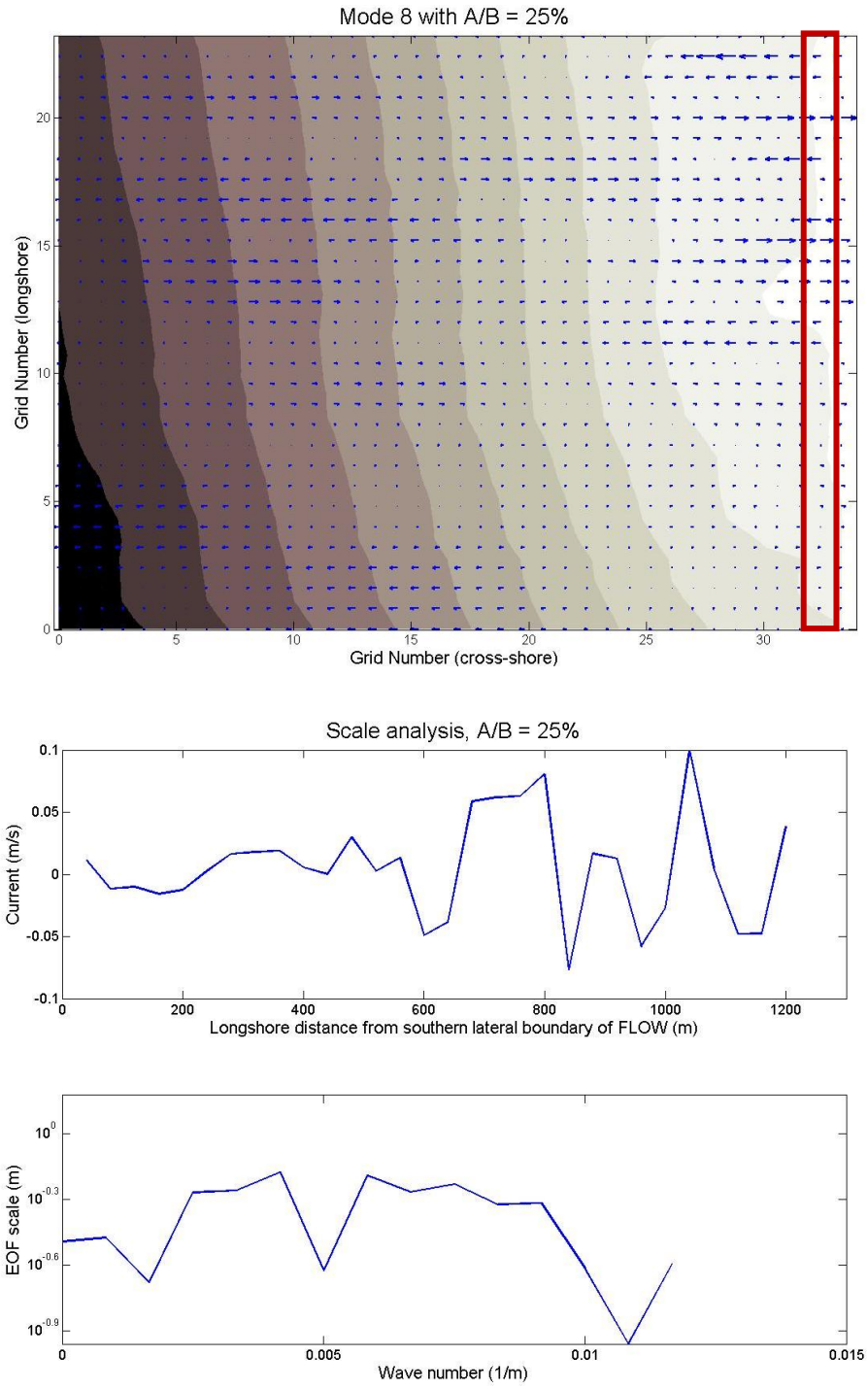

Figure 3.34 Cross-shore component of EOF mode 8 with 25% grid extension ratio (top), and scale analysis for the first series marked with box (bottom).

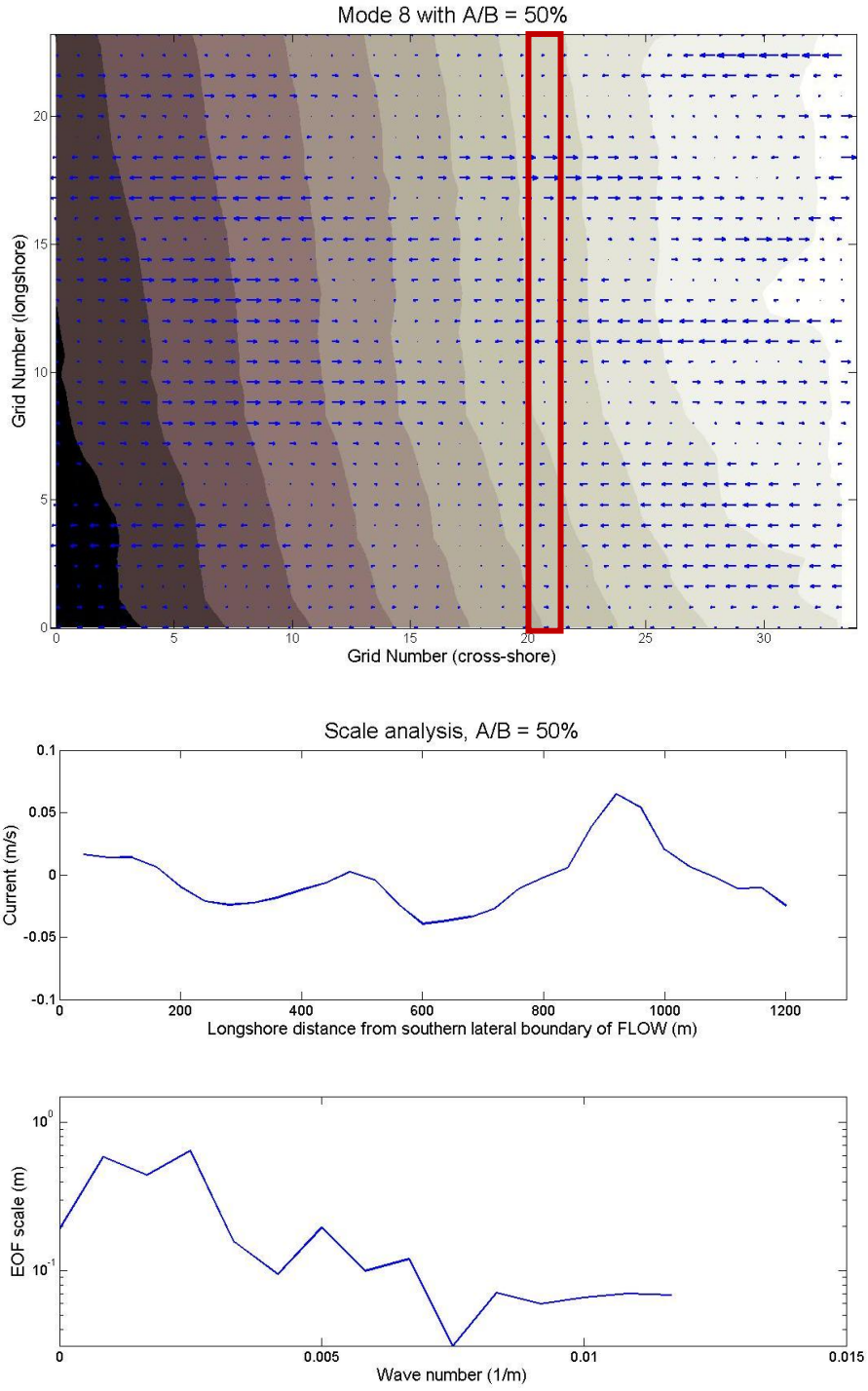

Figure 3.35 Cross-shore component of EOF mode 8 with 50% grid extension ratio (top), and scale analysis for the second series marked with box (bottom).

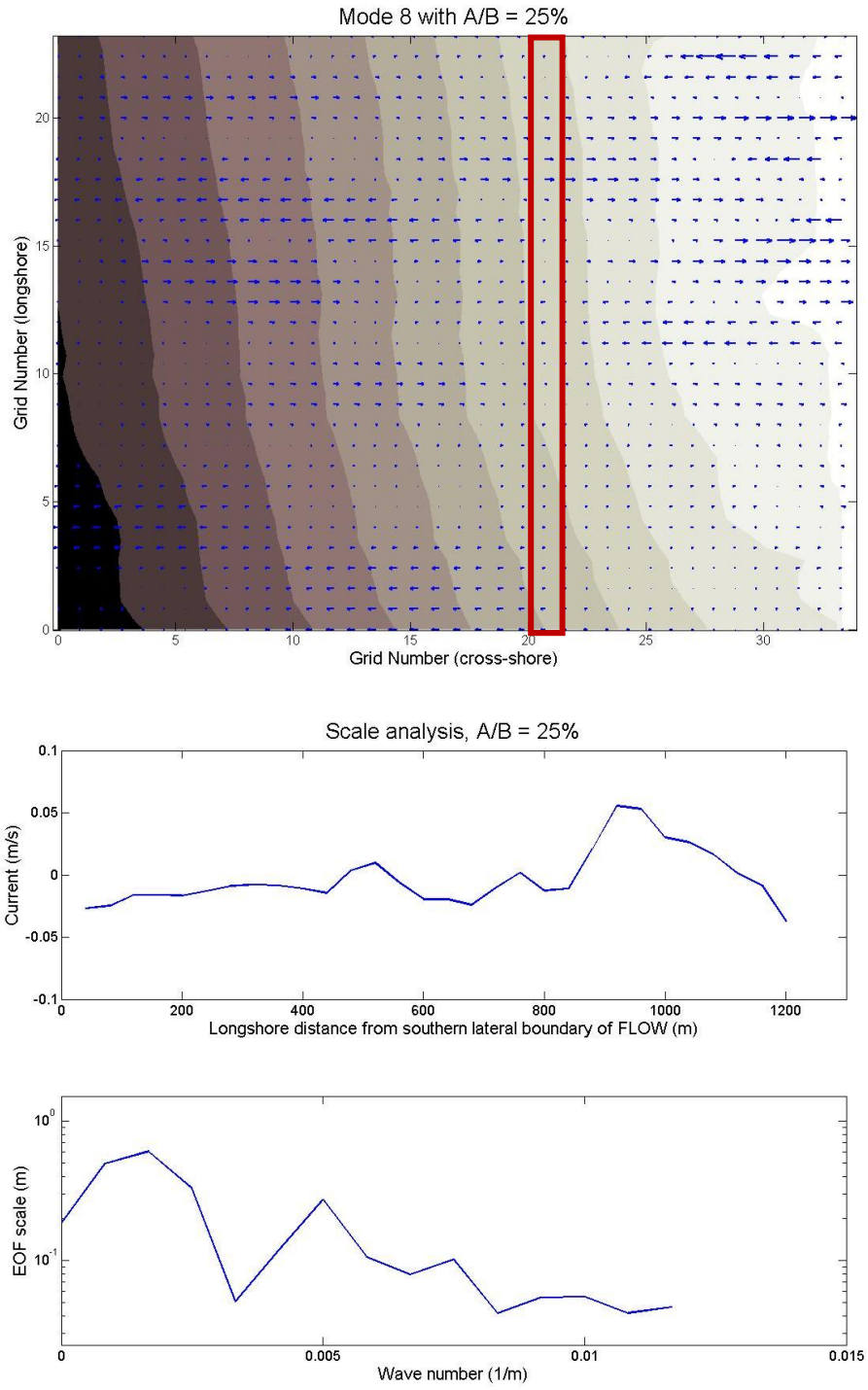

Figure 3.36 Cross-shore component of EOF mode 8 with 25% grid extension ratio (top), and scale analysis for the second series marked with box (bottom).

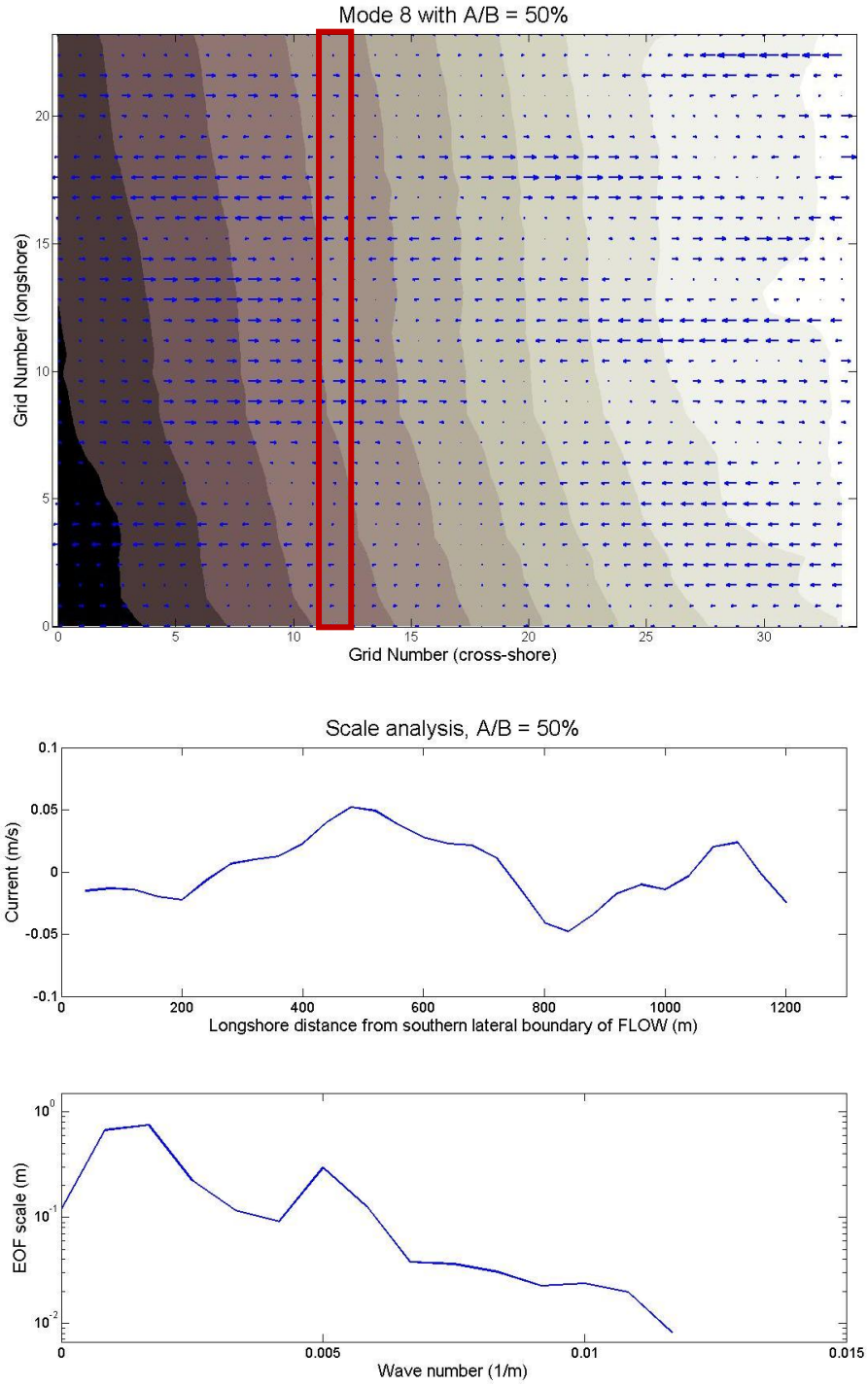

Figure 3.37 Cross-shore component of EOF mode 8 with 50% grid extension ratio (top), and scale analysis for the third series marked with box (bottom).

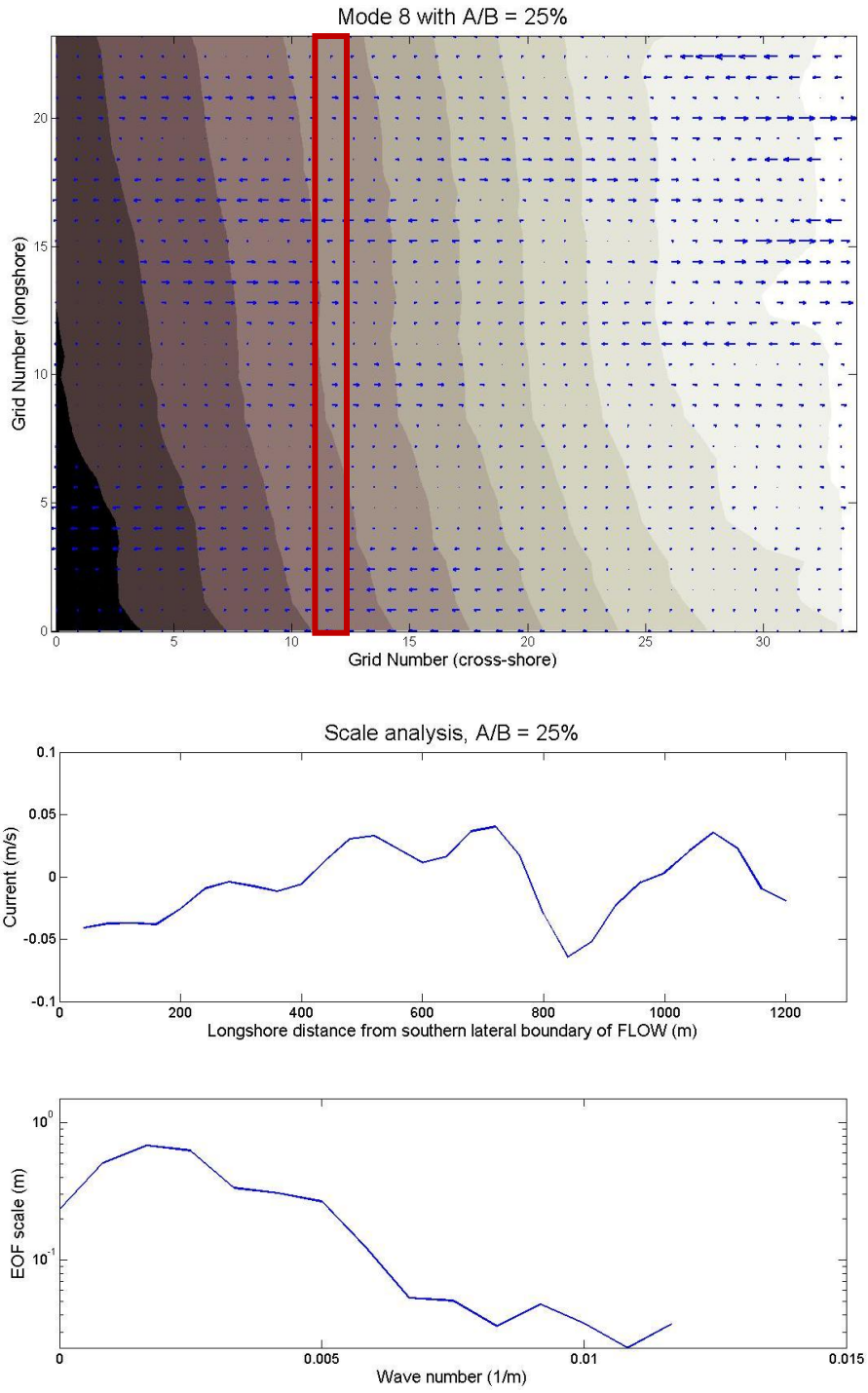

Figure 3.38 Cross-shore component of EOF mode 8 with 25% grid extension ratio (top), and scale analysis for the third series marked with box (bottom).

4. CONCLUSIONS AND FUTURE WORK

Among the recent enhancements to the utility of the Delft3D model for nearshore process simulation is the implementation of Neumann lateral boundary conditions, which allow for flow to enter and leave the lateral boundaries with no artificial circulation. This boundary condition is formulated by reducing the flow equations in the hydrodynamic model to a single dimension, which has the effect of setting conditions on the gradient of the velocities rather than on the velocities themselves. For wave-induced flow, however, one consequence is the need to have a wave-model (SWAN) grid that is significantly wider than the hydrodynamic model (FLOW) grid; this is done in order to keep irregularities in the forcing away from the boundaries of the hydrodynamic model, as well as insure longshore uniformity of conditions at the boundary. However, SWAN requires significant iterative steps, and as such is a computational chokepoint for forecast turnaround. The main focus of this investigation is to examine the effects of boundary errors, seeking a balance between computational efficiency and erroneous computation.

To start with, Duck94 data were used for evaluating Delft3D performance. All three roughness formulations, i.e. Chezy, White-Colebrook and Manning, were evaluated and all produced longshore current results. From the skill statistics, the higher the ratio A/B, the more accurate the representation of the Neumann lateral boundary condition and, consequently, the greater the accuracy when compared to data. However, more computational time is required of the model simulation at high values of A/B. The RMS error for longshore current is about 0.20 *m/s* and is about 0.13 *m* with A/B equal to 50%.

In general, Delft3D has been shown to be accurate and robust in predicting nearshore flows for point-to-point comparison. With these comparisons to data, we have established a baseline ("golden standard") to which we perform comparisons of less accurate model configurations.

Then, the Empirical Orthogonal Function (EOF) analysis is applied to address the two-dimensional behavior of the model response in the face of lateral boundary condition errors, instead of missing information on the spatial response of the model to the forcing by poor data-model comparisons (e.g., the point-to-point comparison). A limited number of the first few EOFs, those with greatest eigenvalues, can be used to describe the fundamental variability in a very large data set. We found that the lower EOF modes are affected less by imposed boundary errors than higher ones.

Both Swirl Strength method and scale analysis serve as a measure of the characteristic of eddylike structures of EOF results and their scales. After quantifying the effect of imposed error by completing inter-mode comparisons among different error cases, inadequacies in the model setup are reflected in the EOF structures.

To this end, a future study could develop methods for correcting the boundary errors to optimize model accuracy. Statistical information on the errors along the boundaries will be useful for this work, which involves the development of methods to correct these forcing errors using data taken within. A Kalman-filter-style (van Dongeren *et al.,* 2008) assimilation and correction system will be investigated for use herein to perform this boundary correction.

REFERENCES

Adrian, R.J., K.T. Christensen, and Z.-C. Liu., 2000. Analysis and interpretation of instantaneous turbulent velocity fields. Experiments in Fluids, 29, 275 – 290.

Booij, N., R.C. Ris, and L.H. Holthuijsen., 1999. A third-generation wave model for coastal regions 1. Model description and validation. J. Geophys. Res., 104(C4), 7649–7666.

Bryant, D.B., D.-G. Seol, and S. A. Socolofsky., 2009. Quantification of turbulence properties in bubble plumes using vortex identification methods. Physics of Fluids, 21, 075101.

Davis, R.E., 1976. Predictability of sea surface temperature and sea level pressure anomalies over the North Pacific Ocean. J. Phys. Oceanogr. 6, 249-266.

Dingemans, M.W., A.C. Radder and H.J. de Vriend., 1987. Computations of the driving forces of wave-induced currents. Coastal Eng. 11, 539-563

Earle. M.D., 1989. Surf forecasting software reference manual. NORDA report, N00014-84-C-0116, 261p.

Hasselmann, K., T.P. Barnett, E. Bouws, H. Carlson, D.E. Cartwright, K. Enke, J.A. Ewing, H. Gienapp, D.E. Hasselmann, P. Kruseman, A. Meerburg, P. Müller, D.J. Olbers, K. Richter, W. Sell and H. Walden., 1973. Measurements of wind-wave growth and swell decay during the Joint North Sea Wave Project (JONSWAP). Dtsch. Hydrogr. Z. Suppl., 12, A8.

Hsu, Y.L., T.R. Mettlach and M.D. Marshall., 2002. Validation test report for the Navy Standard Surf Model. NRL formal report: FR/7322-02-10008.

Hsu, Y.L., Dykes, J.D., Allard, R.A., and Kaihatu, J.M., 2006. Evaluation of Delft3D performance in nearshore flows. NRL Memorandum Report, Naval Research Laboratory, Stennis Space Center, MS.

Janssen, P.A.E.M., 1991a. Quasi-linear theory of wind-wave generation applied to wave forecasting. J. Phys. Oceanogr. 21, 1631-1642.

Kaihatu, J.M., R.A. Handler, G.O. Marmorino, J.A. Roelvink, and L.K. Shay. 1998. Empirical orthogonal function analysis of ocean surface current using complex and real – vector methods. Atmospheric and Oceanic Technology, 15, 927-941.

Lesser, G.R., J.A. Roelvink, J.A.T.M. van Kester and G.S. Stelling. 2004. Development and validation of a three dimensional morphological model. Coastal Eng. 51, 883-915.

Longuet-Higgins, M. S. 1970a. Longshore currents generated by obliquely incident sea waves, 1. J. Geophys. Res., 75: 6778–6789.

Longuet-Higgins, M. S. 1970b. Longshore currents generated by obliquely incident sea waves, 2. J. Geophys. Res., 75: 6790–6801.

Lorenz, E. 1956. Empirical orthogonal functions and statistical weather prediction. Scientific Report No.1, Statistical Forecasting Project, M.I.T., Cambridge, MA, 48 pp.

Miles, J.W. 1957. On the generation of surface waves by shear flows. J. Fluid Mech., 3, 185-204.

Morris, B.J. 2001. Nearshore wave and current dynamics. Ph.D. dissertation, Naval Postgraduate School, Monterey, CA, 89p.

Raffel, M., C.E. Willert, and J. Kompenhans. 1998. Particle image velocimetry: A practical guide. Springer, New York, NY.

Roelvink, D., and D.J. Walstra. 2004. Keeping it simple by using complex models. Advances in Hydroscience and Eng. Volume VI, pp.1-11.

van Dongeren, A.R., N.G. Plant, A. Cohen, J.A. Roelvink, M.C. Haller, and P. Catalan. 2008. Beach Wizard: Nearshore bathymetry estimation through assimilation of model computations and remote observations. Coastal Eng. 55, 1016-1027.

van Dongeren, A.R., and I.A. Svendsen. 2000. Nonlinear and 3D effects in leaky infragravity waves. Coastal Eng. vol. 41, no. 4, pp. 467-496.

Zhou J., R.J. Adrian, and S. Balachandar. 1996. Autogeneration of near-wall vertical structures in channel flow. Physics of Fluids, 8, 288 – 290.

APPENDIX A

We suppose that we have a gridded data set composed of a space-time field Φ (t, p) representing the value of the field Φ at time t and spatial position p. The value of the field at discrete time t_i and grid point p_j is noted Φ_{ij} for i = 1, … , n and j = 1, … , m. The Covariance Matrix is then defined by:

$$\Sigma = \frac{1}{n-1}\Phi^T\Phi, \tag{A.1}$$

which contains the covariance between any pair of grid points. The aim of EOF is to find the linear combination of all the variables, i.e. grid points, that explains maximum variance. That is to find a direction $\alpha = (\alpha_1, \ldots, \alpha_m)^T$, such that Φ*α has maximum variance, Now the variance of the time series Φ*α is:

$$\mathrm{var}(\Phi * \alpha) = \frac{1}{n-1}\left\|\Phi * \alpha\right\|^2 = \frac{1}{n-1}(\Phi * \alpha)^T(\Phi * \alpha) = \alpha^T \Sigma \alpha \tag{A.2}$$

Then the solution to (A.2) is a eigenvalue problem: $\Sigma\alpha = \lambda\alpha$ By definition the k'th EOF is simply the k'th eigenvector αk of matrix ∑ in decreasing order. A proof of this is given in Davis (1976).

APPENDIX B

Figure B.1-B.4 depict the spatial and temporal behavior for EOF modes 3-6 based on the NCEX case with extension ratio A/B equal to 50% and 25% respectively.

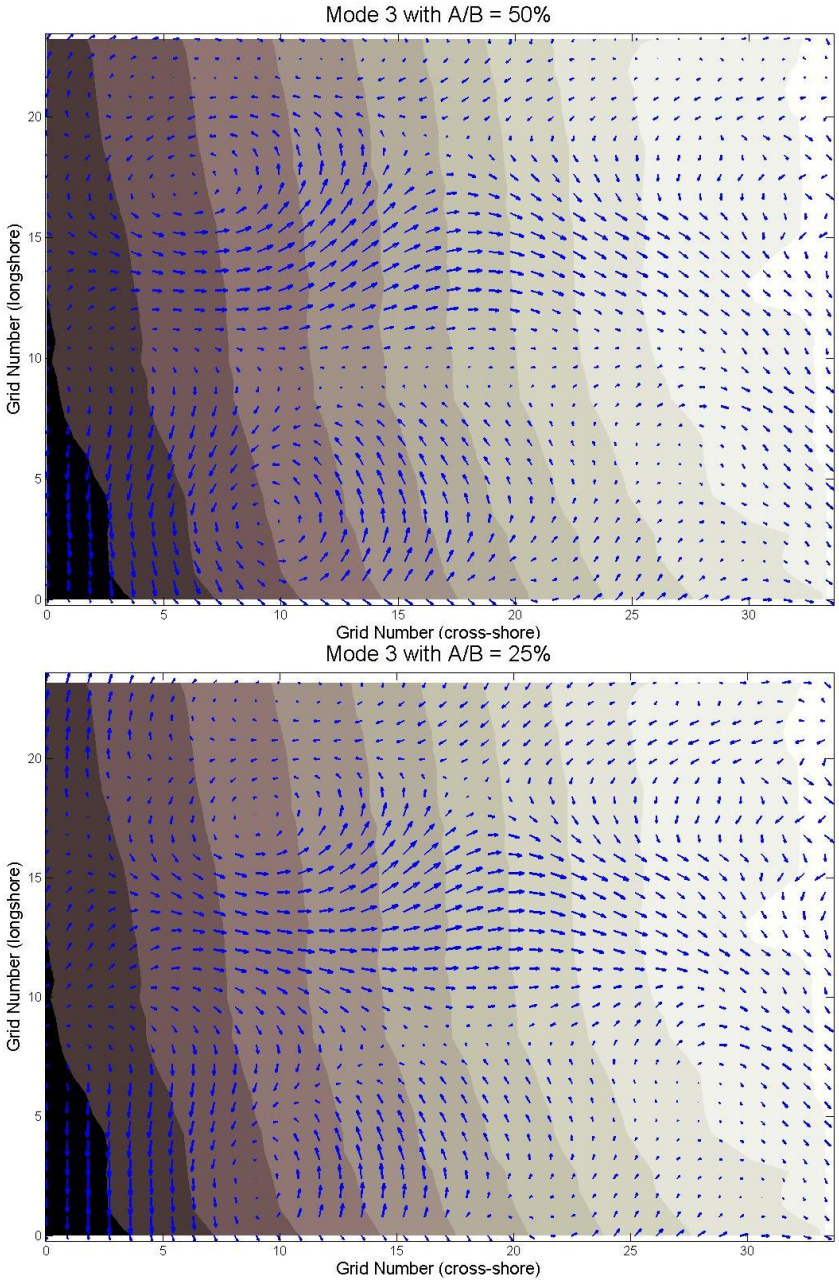

Figure B.1 EOF mode 3 based on the NCEX case with A/B=50% (top) and A/B=25% (bottom).

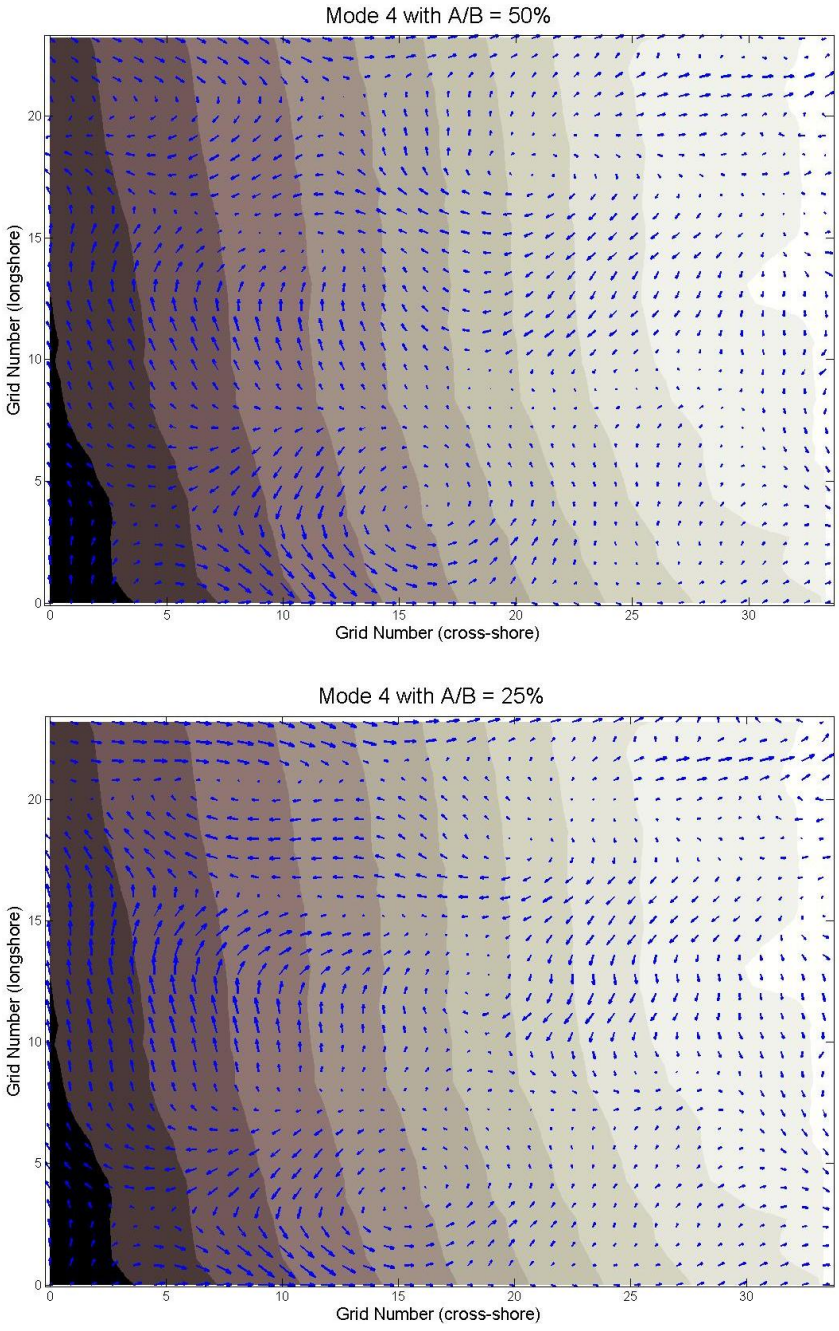

Figure B.2 EOF mode 4 based on the NCEX case with A/B=50% (top) and A/B=25% (bottom).

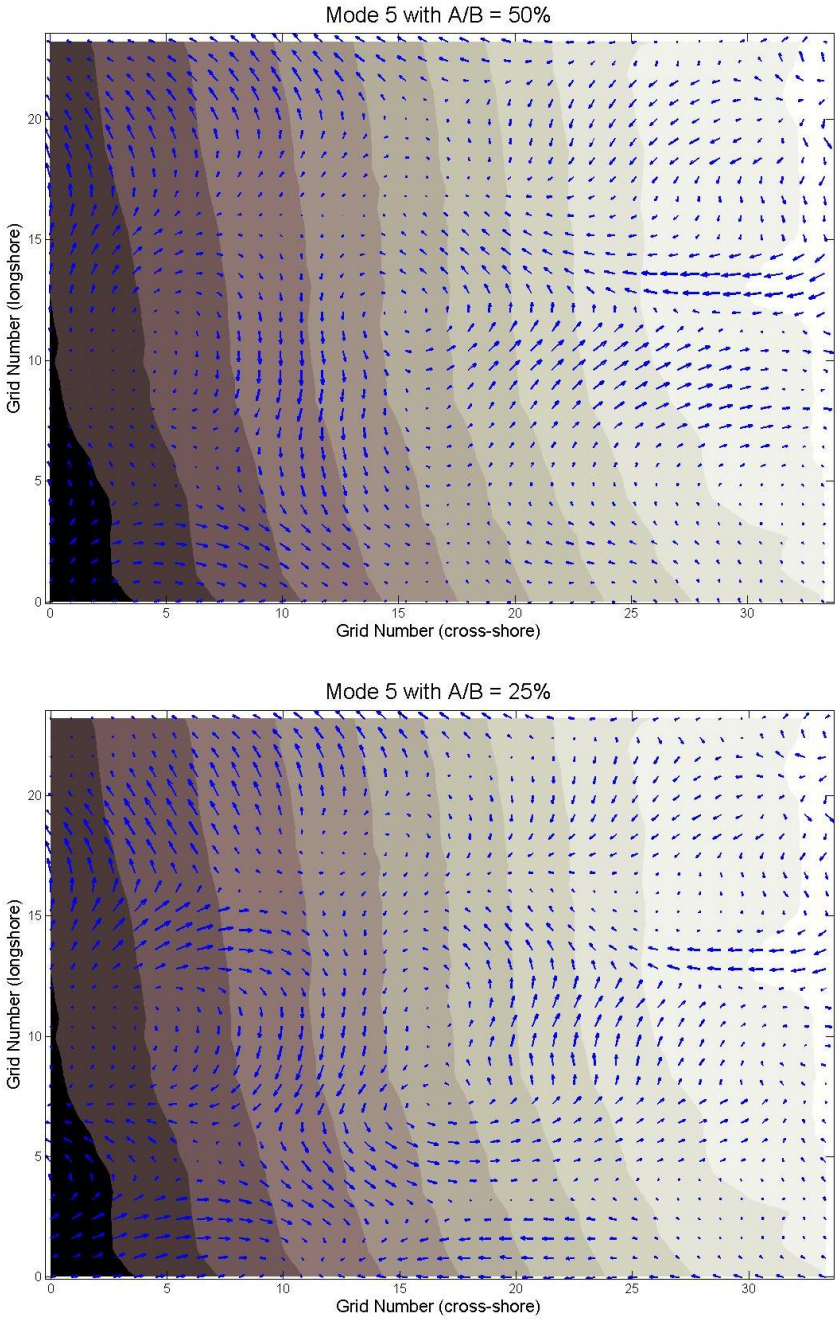

Figure B.3 EOF mode 5 based on the NCEX case with A/B=50% (top) and A/B=25% (bottom).

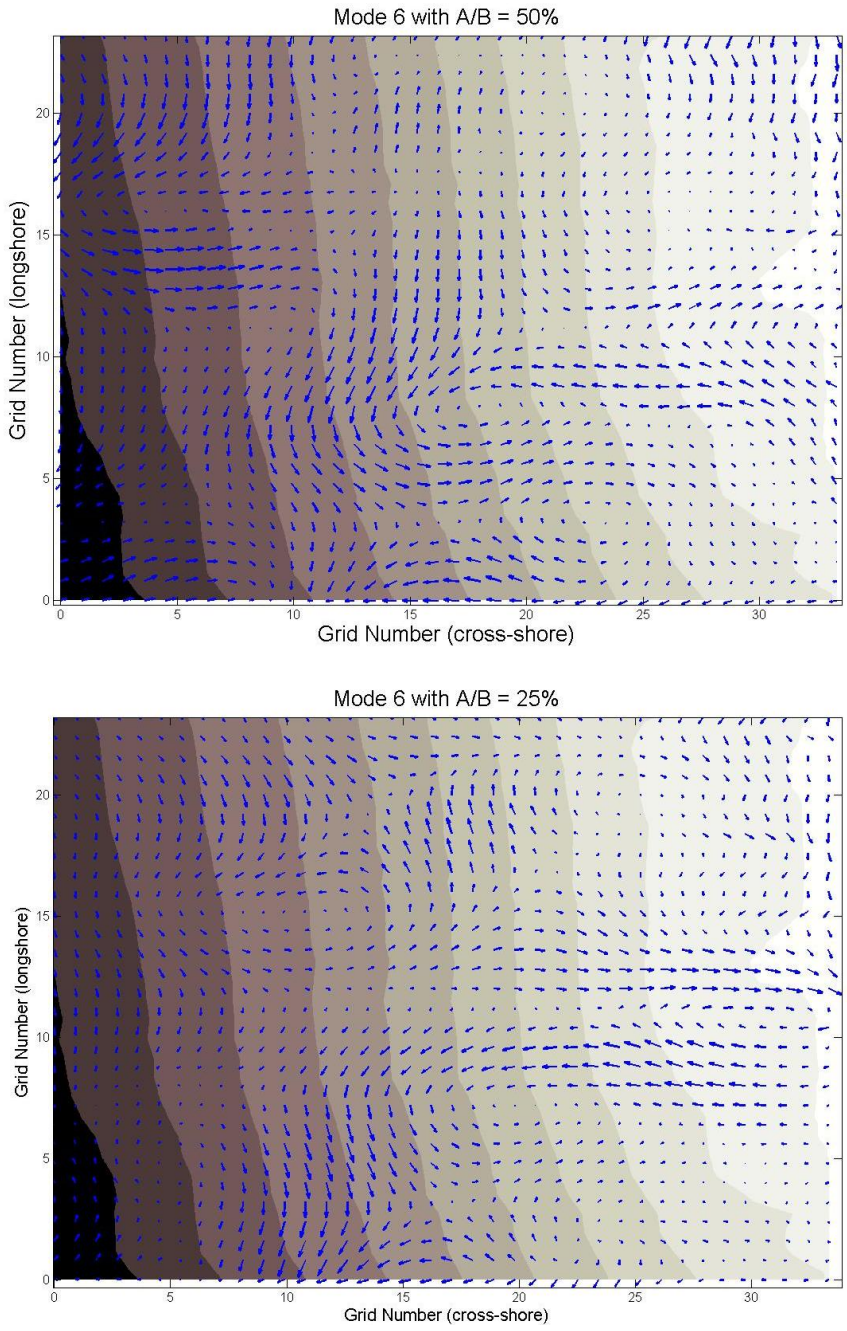

Figure B.4 EOF mode 6 based on the NCEX case with A/B=50% (top) and A/B=25% (bottom).

VITA

Name: Boyang Jiang

Address: Department of Civil Engineering
Texas A&M University
3136 TAMU
College Station, Texas 77843-3136
USA

Email Address: jby2008nj@hotmail.com

Education: B.Tech., Hydropower Engineering, Hohai University, Nanjing, China, 2008
M.S., Ocean Engineering, Texas A&M University, College Station, USA, 2010